Faculty of Mathematics and Physics
Charles University in Prague

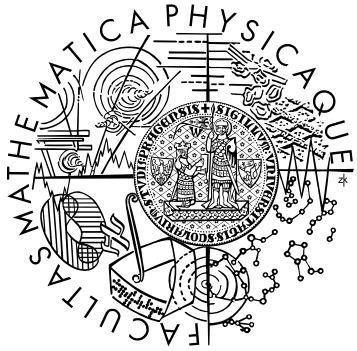

Terahertz spectroscopy of ferroelectrics and related materials

Alexej Pashkin

Ph.D. Thesis

Supervisor: Dr. Jan Petzelt

Prague 2004

Acknowledgments

I am very grateful to my supervisor Jan Petzelt for his guidance and support. He was always open for discussions and ready to share his deep understanding of dielectric phenomena.

I am very grateful to my consultant Petr Kužel who introduced me to the field of time-domain terahertz spectroscopy and physics of ultrafast phenomena. His wide knowledge, creative approach and thorough analysis of any problem made him a living example of practical physicist for me. I also appreciate very much his critical reading of the present manuscript which resulted in great improvement of the thesis.

Many thanks to my consultant Stanislav Kamba. He introduced me to the Fourier Transform Infrared spectroscopy and to the fitting technique. The most part of presented work performed on microwave ceramics has been done with his strong cooperation. I also would like to thank Milan Berta who performed fitting of IR data of $CaTiO_3$-based ceramics.

I am very grateful to my colleagues Viktor Porokhonskyy and Maxim Savinov for providing the results of dielectric spectroscopy in high- and low-frequency ranges which has been used in the present thesis. Also I would like to thank Vladimir Železny for the help with infrared measurements and to Polina Samoukhina who has measured infrared reflectivity of SBiT ceramics. A lot of help I received from other members of Department of Dielectrics. This concerns not only scientific work but also friendly and cheerful atmosphere in the department. In order not to miss some of their names, I want to thank all of them.

My visits to PI1 in Stuttgart University in order to perform measurements on BWO spectrometer were possible due to the kind invitation of Martin Dressel, the head of the institute. I would like to thank him and Boris Gorshunov who introduced me to backward wave oscillator spectroscopy as well as to the whole group of PI1 for their hospitality during my stays in Stuttgart. The financial support of Deutsche Forschungsgemeinschaft (GO 976/1-1) is acknowledged.

This work was also supported by Ministry of Education of the Czech Republic (Project No. LN00A032).

I would like to thank Hans Vogt for useful discussion and sharing of his hyper-Raman results of KLT crystals. The discussions with Vladimir Železny and Vladimir Trepakov are also appreciated a lot. I am grateful to Filip Kadlec for great improvements in our THz lab which allowed to perform fast and reliable measurements. He also helped me with preparation of this thesis using LaTeX typesetting system.

Last but not least, many thanks to Viktor Bovtun for useful discussions and also for inviting me to the PhD study in Prague.

Contents

Introduction

The present work is the result of an experimental study of different ferroelectrics and materials related to them mostly by means of the THz spectroscopy. Although this method is very useful for characterization of condensed matter system, its potential has not been fully realized in the investigation of dielectric materials. Therefore we did not restrict ourselves to the study of particular ferroelectric systems. The THz spectroscopy has been applied to a variety of samples such as single crystals, ceramics and thin films. In some cases, the THz spectroscopy was not the main experimental technique, though the obtained THz data have given a complementary information which in combination with other methods of dielectric spectroscopy allow to improve the quantitative picture of dielectric response in the broad frequency range. This kind of results are not presented in this work. Contrariwise, we present the investigations of dielectric systems in which the results of THz spectroscopy bring deeper insight on ultrafast polarization dynamics and lead to qualitatively new results.

The measurements in the THz frequency range has been performed by two techniques: time-domain THz spectroscopy and backward-wave oscillator spectroscopy. The obtained dielectric spectra have been analyzed in combination with the results of far infrared reflection spectroscopy, low-frequency and microwave dielectric measurements. In addition, second harmonic generation measurement has been carried on $K_{1-x}Li_xTaO_3$ system.

The materials investigated in this work can be divided in two large groups. The first group includes microwave ceramics which have extremely low dielectric losses in the microwave frequency range and moderate dielectric constant. The THz spectroscopy enables estimation of the intrinsic losses in the microwave range which can be compared to the actual losses in the ceramics. Hence one can make conclusions about the dependence of the quality of ceramics on composition and preparation technology. The second group of materials are doped incipient ferroelectrics with relaxor properties. These materials are characterized by high dielectric constants and appreciable losses in the THz range. The THz measurements at different temperatures provide very important information about the phonon dynamics and various polar excitations in the THz frequency range.

The manuscript is divided into three parts. The first part gives an overview of the methods of THz spectroscopy which have been used for the measurements. It presents a comparison of these methods and discusses their advantages and drawbacks. In addition, a new method of time-domain reflection spectroscopy, developed in the frame of this work, is presented. The second part presents the results obtained for various microwave ceramics systems. The third part is devoted to the analysis of THz spectra of doped incipient ferroelectrics and to the comparison of the obtained result with those published in literature.

Part 1

Methods of THz spectroscopy

The terahertz (THz) frequency region is very important in the spectroscopy of condensed matter systems. However, until recently this region was not easily accessible because of the lack of suitable sources and spectroscopic techniques. Conventional microwave techniques are limited to below roughly 100 GHz. Fourier Transform Infrared (FTIR) spectroscopy, on the other hand, can hardly reach the frequencies below 10-15 cm^{-1} (300-500 GHz) because of insufficient brightness of incoherent sources. In addition, FTIR spectroscopy measures only the intensity transmission or reflection function and hence does not allow direct determination of the real and imaginary parts of the response function without using Kramers-Kronig relations or some appropriate fitting models. From this point of view it is very useful to develop quasioptical phase sensitive techniques which can perform measurements of complex transmission or reflection functions. However the key problem for realization of such an experiment is the development of powerful broadband or tunable sources of coherent THz radiation. This is a complicated task that was solved in two different ways (we do not discuss synchrotron and free-electron laser radiation here). The first way consists in extension of the emission range of microwave vacuum devices towards millimeter wavelength region. As a result the tunable monochromatic generators - *Backward Wave Oscillators* (BWOs) were developed in the 1960s. Then the method of coherent-source submillimeter spectroscopy (or BWO spectroscopy) was developed and applied to the investigation of dielectric properties of a wide range of substances (ferroelectrics, superionic conductors, superconductors etc.) [1, 2]. The second method of generation of coherent THz radiation has become possible with appearance of commercially available ultrafast lasers. It is based on electro-optical generation and detection of electromagnetic transients using femtosecond laser pulses. These transients (THz pulses) are single-cycle bursts of electromagnetic radiation with typical duration around 1 ps. Their spectra typically cover frequency region from 100 GHz up to several THz. The spectroscopic technique utilizing coherent broadband THz pulses is called terahertz time-domain spectroscopy (TDTS). Starting from 1990s TDTS has been applied to studying a great variety of materials, including dielectrics [3], semiconductors [4], superconductors [5], organic materials [6] etc. Recently, additional new promising way of generation of tunable monochromatic THz radiation based on nonlinear frequency mixing of dual-wavelength laser beam has been realized [7]. In perspective, the whole THz source of such type can be incorporated into a single laser diode. The advantage of this method would be the low-cost and compactness comparing to the BWOs and femtosecond lasers. However, cw-THz sources are in the initial stage of development

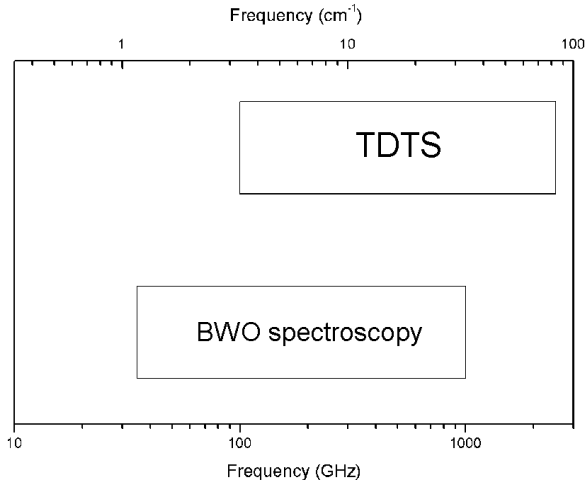

Figure 1.1: Frequency regions covered by TDTS and BWO spectroscopy.

and no application for THz spectroscopy has been reported yet.

The comparison of frequency regions covered by the above mentioned spectroscopies is shown in Figure 1.1. TDTS is able to reach higher frequencies (up to 80 cm^{-1} or more) than BWO spectroscopy and is more convenient in the sense that a single measurement allows to characterize the whole accessible frequency range while BWO spectroscopy requires about 10 separate measurements with different BWOs to fully cover the accessible frequencies. On the other hand, the main advantage of BWO spectroscopy is connected to the fact that the radiation power of BWO increases towards low frequency limit of these sources (about 1 cm^{-1}). Thus it is possible to perform reliable measurements at the lowest accessible frequencies of BWO spectroscopy. In contrast, TDTS is less suitable for the measurements below 5 cm^{-1}. Thus each of this two methods has its advantages in particular investigation.

1.1 Principles of BWO spectroscopy

1.1.1 Backward wave oscillators

Figure 1.2 shows schematically the arrangement of the BWO, which is similar to conventional electrovacuum diode and triode. When the heater (1) is switched on, the cathode (2) emits a beam of electrons (3) which, accelerated by a high anode (4) voltage, travels in vacuum toward the anode (collector). The electron beam collimated by an external magnetic field (magnet 5) flies over a comb-like fine-structure electrode (6) (slowing system) intended to transfer the kinetic energy of the electrons to the electromagnetic field. Actually, moving in the periodic potential of the slowing system, the electrons are grouped periodically in bunches and induce an electromagnetic wave (7) traveling in the opposite direction to the electrons (backward wave). This radiation comes out through an oversize waveguide (8). The velocity of the electrons, and thus the radiation frequency, are determined by the magnitude of the accelerating field.

Despite of simple construction, production of BWOs is highly sophisticated task since reaching of shorter wavelengths imposes conflicting requirements on the electrical and geometrical parameters of these devices. Within a particular device one should

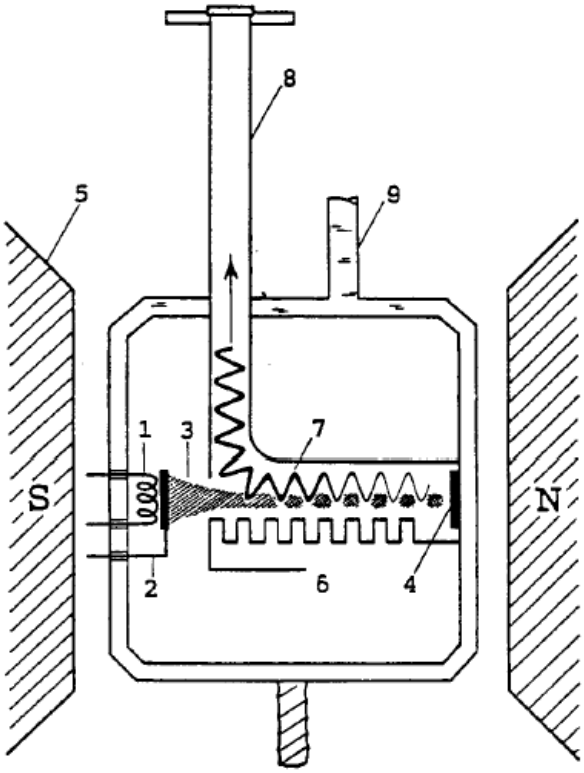

Figure 1.2: Schematic diagram of backward wave oscillator: 1 - heater, 2 - cathode, 3 - electron beam, 4 - anode, 5 - permanent magnet, 6 - slowing system, 7 - electromagnetic wave, 8 - waveguide, 9 - water cooling.

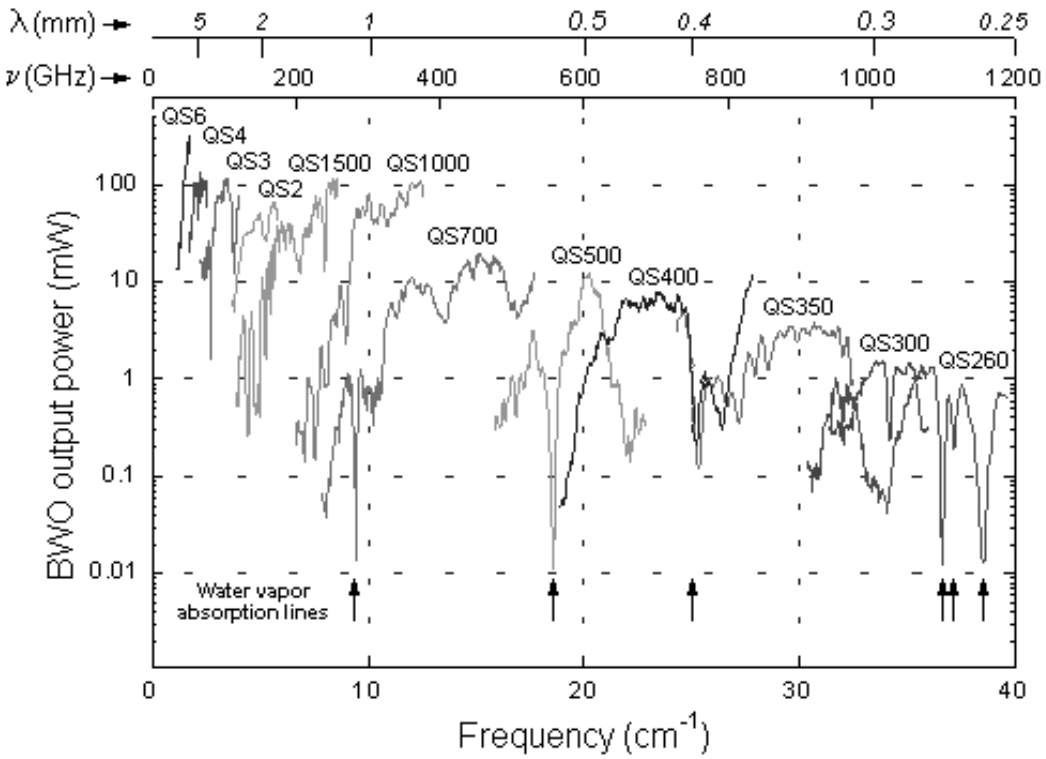

Figure 1.3: Spectra of BWO sources.

combine a large number of small gaps (millimeters and fractions of millimeter) with high voltages (up to 6 kV), high temperatures (up to 1200℃ on the cathode) and high vacuum (up to 10^{-6} Pa). The electron current density in the beam has to be increased up to 150 A/cm^2.

Figure 1.3 shows output power of BWO sources in the whole accessible frequency range (from 1 cm^{-1} to 40 cm^{-1}). The output power of BWO seems to look like a random function of frequency, though, it is highly reproducible for a particular source. The BWO output power power may change by one or two orders of magnitude between the minima and maxima of the BWO's spectral pattern. This is a disadvantage of BWO spectroscopy: the measurement error is different for different points of the spectra. However, careful estimation of the errors and repeating of the measurements several time allows obtaining reasonable data in most cases. On the other hand, the great advantage of BWO spectroscopy is its high resolution. It depends on many factors such as quality of BWO, stability of cathode voltage and heater current and so on. Typically the monochromaticity of the BWO radiation and its frequency reproducibility under high voltage tuning conditions can be maintained at the level of $\Delta f \approx 10^{-5} f$.

1.1.2 Detectors of BWO radiation

The BWO's radiation can be detected either by microwave methods (crystal detectors with point contact) or by methods of infrared spectroscopy (thermal and photoelectric detectors).

The most commonly used detector of BWO radiation is acousto-optical Golay

cell. Its sensitivity is about $\approx 10^{-10} - 10^{-11}$ W Hz$^{-1/2}$ which is several times higher than of the pyroelectric detectors. The main advantage of Golay cell is frequency-independent response in the whole sub-mm wavelength range and ability to operate at room temperature. The dynamical range is 40 dB and the saturation power is about 0.1 mW. Thus the Golay detectors most optimally correspond to the power characteristics of BWO sources with the exception of the sources at the low and high frequency edge of the available spectrum.

Microwave crystal detectors are more suitable for the millimeter wavelength range, where they have an appropriate sensitivity $\approx 10^{-11}$ W Hz$^{-1/2}$ and the response time $\approx 10^{-9}$ s. They work at room temperature, they are simple to operate and commercially available. Their main drawback is the frequency selectivity. The detector heads are usually used in a waveguide variant which implies a narrow-band spectral tunability. Therefore microwave detectors are rarely used in BWO spectrometers in the frequency range above 3 cm^{-1}.

The output power of BWOs which covers the highest accessible frequencies (30-40 cm^{-1}) is too weak to be reliably detected by the Golay cell. For the measurements with these sources more sensitive detectors like He-cooled silicon bolometers have to be used. They have high sensitivity ($10^{-11} - 10^{-13}$ W Hz$^{-1/2}$), but comparatively large response time ($\approx 10^{-2} - 10^{-3}$ s). Besides high frequency range they can be used for the transmission measurements of highly absorbing samples where the transmitted signal is weak.

1.1.3 Principal schemes of BWO spectroscopy setup

All BWO measurements mentioned in further sections were performed using the BWO-based spectrometer "Epsilon". Among the variety of known BWO setups it is distinguished by two features: a rapid, reproducible, high-precision, wide-range scanning of the frequency and a unique equipment for dielectric measurements [8].

The acquisition system of "Epsilon" consists of a detecting unit (Golay cell or He-cooled bolometer), an amplifier synchronized with a 25 Hz radiation modulator (chopper) and a sampling-storage-reset circuit. The dynamic range of electronic registration unit is 10^4. Taking into account the dynamical range of optical attenuator ($10^3 - 10^4$) it provides a value of $10^7 - 10^8$ for the whole spectrometer.

The measuring section of the spectrometer can be adapted either for transmission or reflection measurements (Figure 1.4). While the specific measuring geometry depends on the choice of the experimental method, the basic invariable principles of its construction are the following: the radiation propagates in free space; a beam with a diameter ≈ 40 mm is formed by dielectric lenses or by metallic parabolic mirrors; plane one-dimensional wire grids with a period $L \ll \lambda$ (λ is the radiation wavelength) are used as polarizers and beam splitters; the sample is placed in a channel tightly pressed against a metallic diaphragm. In both measuring geometries the radiation impinges under normal incidence onto the sample which is prepared in the form of plane-parallel plate. Depending on the method used, the measurable quantities can either be the intensity transmission coefficient T of the sample and the phase shift ϕ of the transmitted wave, or the intensity reflection coefficient R (the reflected wave phase shift ψ is not measurable, see below). The mathematical relationships connecting these measurable quantities with real and imaginary parts of the complex refractive of bulk sample (n and κ) are well known in optics [9]:

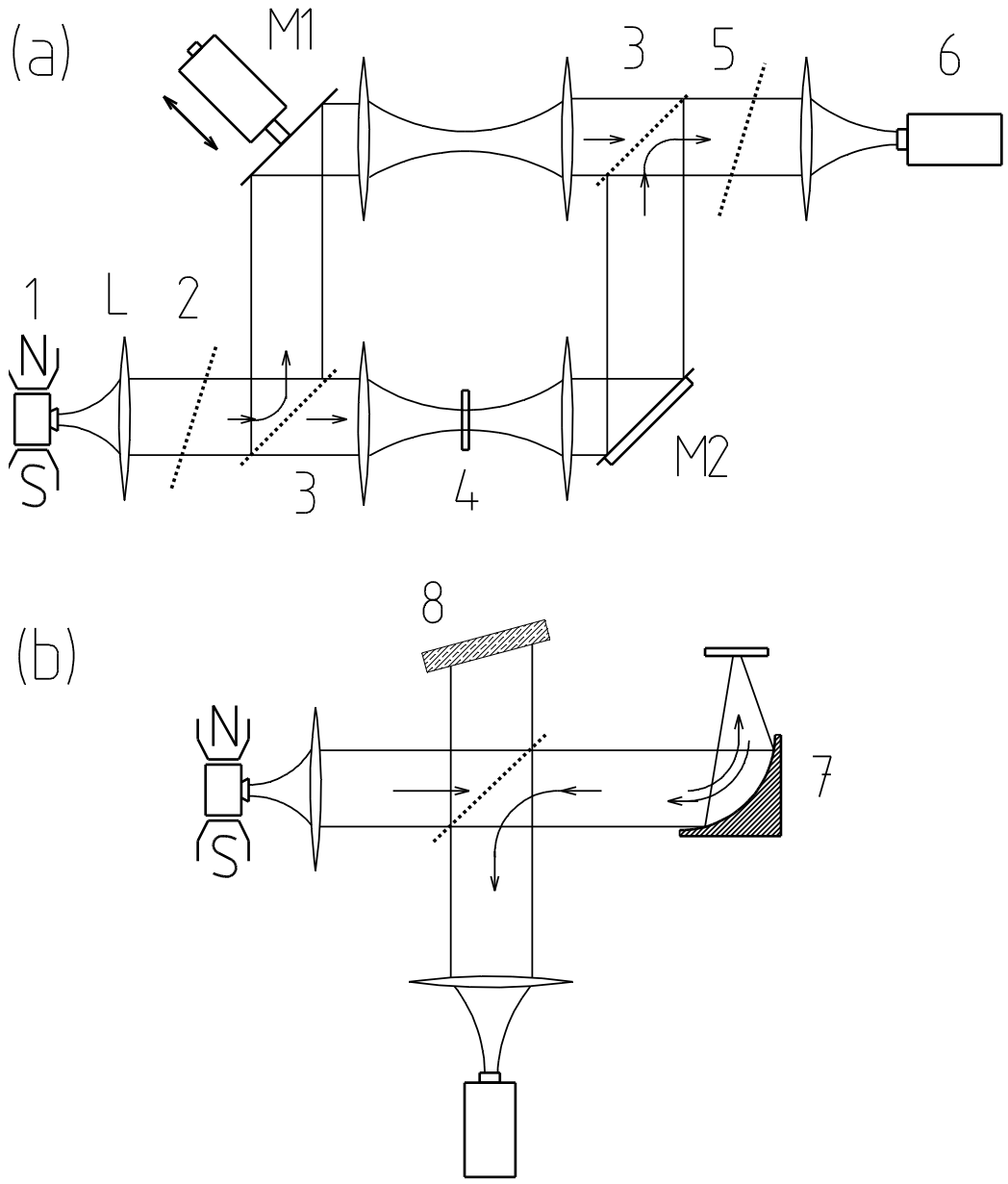

Figure 1.4: Scheme of the BWO-spectrometer "Epsilon": (a) - transmission geometry, (b) - reflection geometry. 1 - BWO, 2 - polarizer, 3 - wire-grid beam-splitters, 4 - sample, 5 - analyzer, 6 - detector, 7 - parabolic mirror, 8 - absorber, L - teflon lens, M1 and M2 - moving mirrors.

$$T = e^{-\frac{4\pi\kappa d}{\lambda}} \frac{(1-R)^2 + 4R\sin^2\psi}{\left(1 - Re^{-\frac{4\pi\kappa d}{\lambda}}\right)^2 + 4Re^{-\frac{4\pi\kappa d}{\lambda}}\sin^2\left(\frac{2\pi nd}{\lambda} + \psi\right)}, \tag{1.1}$$

$$\begin{aligned}\phi &= \frac{2\pi(n-1)d}{\lambda} - \arctan\frac{\kappa(n^2+\kappa^2-1)}{n+(n^2+\kappa^2)(n+2)} \\ &\quad + \arctan\frac{Re^{-\frac{4\pi\kappa d}{\lambda}}\sin 2\left(\frac{2\pi nd}{\lambda} + \psi\right)}{1 - Re^{-\frac{4\pi\kappa d}{\lambda}}\cos 2\left(\frac{2\pi nd}{\lambda} + \psi\right)},\end{aligned} \tag{1.2}$$

$$R = \frac{(n-1)^2 + \kappa^2}{(n+1)^2 + \kappa^2},$$

$$\psi = \arctan\left(\frac{2\kappa}{n^2+\kappa^2-1}\right), \tag{1.3}$$

where d is the sample thickness. Obviously, any pair of quantities from T, ϕ, R and ψ can be used to calculate n and k. However, different pairs of measurable quantities are not equivalent in providing the maximal accuracy of the optical constants determination. It turns out that under nearly identical conditions, the T and ϕ pair gives the best results. This method is the most preferable in dielectric measurements and is always used when the radiation power is sufficient to penetrate through the sample and to be registered by the detector.

The essential part of BWO-spectrometer in transmission geometry is Mach-Zehnder interferometer (see Figure 1.4a) containing two wire-grid beam-splitters and two mirrors (M1 and M2). The measurement in basic (T, ϕ)-configuration consists of two stages. First the power transmission dependence on frequency $T(f)$ is measured in a simple transmission geometry, the empty branch of interferometer (containing M1) is blocked during this measurement. Transmission is determined as the ratio of BWO signals recorded when the sample is inside measuring branch (sample signal) and when the sample is removed (calibration signal). In this way all the instrumental factors are canceled out and $T(f)$ is directly obtained. The second stage involves the recording of $\phi(f)$. Both branches of Mach-Zehnder interferometer are used in this process. During the frequency scan, the position of the mirror M1 is continuously adjusted by the computer feedback system in order to sustain the interferometer in balanced state (zero signal on the detector). The measured quantity in this case is the mirror displacement $\Delta(f)$. In other words, the spectrometer registers the change in the optical thickness of the sample vs. frequency. The phase spectrum is then equal to

$$\phi(f) = \frac{2\pi}{c} f[\Delta(f) - \Delta_0(f)] + 2\pi m, \tag{1.4}$$

where c is the speed of light, m is the phase order and $\Delta_0(f)$ is the calibration measurement without the sample.

Having performed the measurement in (T,ϕ)-configuration one can calculate complex refractive index of the sample material solving numerically the system of two equations (1.1 and 1.2). However, for the correct definition of the phase factor in Equation 1.2 one has to specify the phase order m. This is consequence of the fact that during a phase measurement the interferometer is kept balanced near the proximate minimum of interference. Usually the phase order can be easily estimated

knowing the sample thickness and an approximate value of refractive index. Furthermore, the frequency range of each particular BWO source is quite narrow so that the corresponding phase change is smaller than 2π even for highly dispersive materials. Thus the phase order can be set as a constant for one measurement.

Dielectric parameters of the material are related to the real and imaginary parts of the complex refractive index by simple formulas:

$$\begin{aligned} \epsilon' &= n^2 - k^2, \\ \epsilon'' &= 2nk, \end{aligned} \tag{1.5}$$

$$\begin{aligned} \sigma' &= 2\pi f \epsilon_0 \epsilon'', \\ \sigma'' &= 2\pi f \epsilon_0 \epsilon', \end{aligned} \tag{1.6}$$

where ϵ', ϵ'' and σ', σ'' are real and imaginary parts of permittivity and conductivity respectively, ϵ_0 - the permittivity of vacuum. Taking into account typical technical specifications of BWO-spectrometer and assuming that the bulk sample thickness can be reduced to a few tens of micrometers, the values of $\epsilon', \epsilon'' \approx 1000$ ($\sigma \approx 100\ \Omega^{-1}\mathrm{cm}^{-1}$) are accessible for measurements with "Epsilon" spectrometer in the transmission geometry. The average accuracy of such dielectric measurements over a wide frequency range is $\approx 5\%$ for ϵ' and $\approx 10\%$ for ϵ''. However the measurement accuracy may be lower at the lowest and highest parts of the accessible spectral range (near 1 and 40 cm^{-1}) because of the low power of high frequency BWO and because of the strong parasitic diffraction and interference effects at low frequencies.

If the sample has high dielectric loss and is opaque in the submm range, the transmission geometry cannot be used for the measurement. In this case, dielectric properties can be determined from the analysis of the reflectivity. The reflection geometry of BWO spectrometer is depicted in Figure 1.4b. In contrast to transmission setup, the reflection geometry is similar to the Michelson interferometer with one beam-splitter. The beam focused by the parabolic mirror reflects back from the sample which plays the role of end mirror in one branch of the interferometer. Second branch of the interferometer is blocked by an absorber. The radiation reflected from the sample is directed to the detector by the beam-splitter. Thus one can measure power reflectivity of the sample as a ratio of sample and calibration signals, in analogy with the first stage of transmission measurements. For the calibration measurement in reflection geometry a silver or aluminium mirror with almost 100% reflectivity is used.

In principle, the second stage of reflectivity measurements which determines the phase shift $\psi(f)$ is possible if we place a mirror in the second branch of Michelson interferometer. Then the calculation of complex refractive index using Equation 1.3 becomes possible. However, as the THz radiation is directly reflected on the sample surface, the phase shift induced by the sample is much smaller than in the transmission experiment where it is proportional to the sample thickness. In other words, it means that $\psi(f) \ll \phi(f)$. Therefore even small errors in the phase lead to appreciable errors in the determination of complex refractive index. This fact is demonstrated in Figure 1.5. The curves in the plane of the complex refractive index correspond to constant values of the reflectance amplitude and adjacent points correspond to the difference in the reflectance phase induced by a 1 µm-shift of the sample for frequency 1 THz. The shape of the curve remains unchanged for other frequencies while the

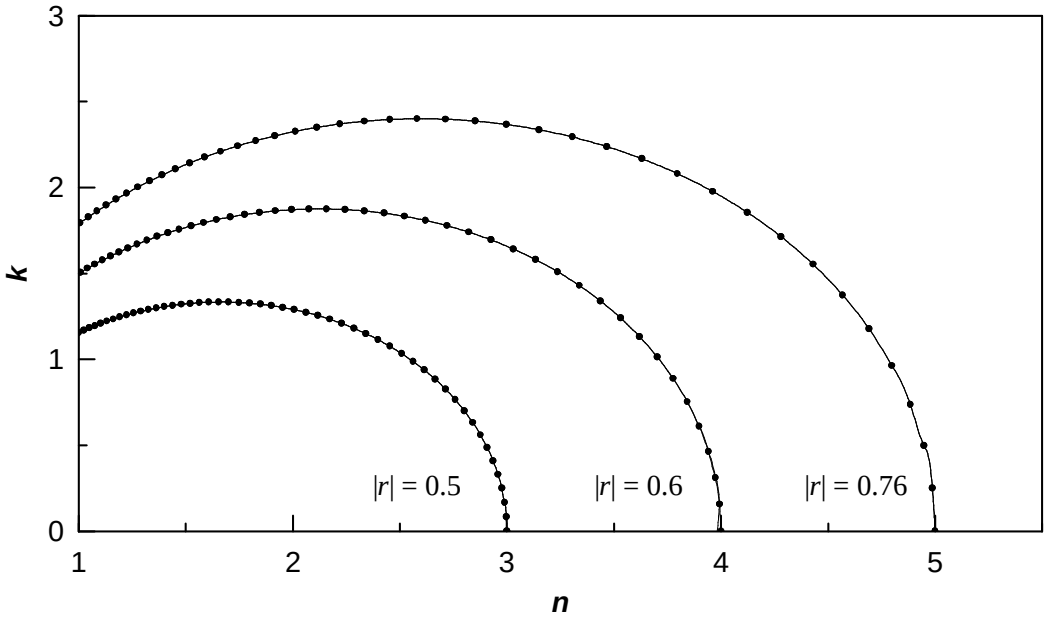

Figure 1.5: Complex refractive indices corresponding to the same reflectance amplitude. Adjacent points correspond to a phase change equivalent to 1 µm displacement of the sample. The values are calculated for normal incidence and frequency 1 THz.

spacing between points is inversely proportional to the frequency. For a low absorption index (close to the real axis) the slope of the curves is almost vertical. Therefore a small phase error leads to large errors in the calculated absorption index. On the other hand, when the refractive and absorption indices are comparable, the slope is horizontal and error in the real part of refractive index becomes dominant. Thus the requirements for the relative alignment of the sample and reference mirror are very strict in reflection geometry: spatial shift - less than 1 µm, angular misalignment - less than a few mrad. It is almost impossible to fulfil these requirements in BWO spectrometer, especially in the case when the sample is placed inside a cryostat. Therefore "Epsilon" is used only for the determination of reflection amplitude which is then used to extend the spectra obtained by means of FTIR reflection spectroscopy (see Section 1.3).

The transverse size of the samples for BWO spectroscopy (as well as for TDTS) has the limitation which depends on the measuring geometry and the frequency range. In the reflectivity measurements one has to ensure that the detected signal is reflected only from the sample and not from the front aperture. Otherwise it can lead to an error in determination of the reflectivity amplitude. It is known from the optics that the beam cannot be focused to a spot smaller than the wavelength of radiation. It implies the sample transverse size to be larger than the wavelength, usually at least by three times. In other words, if we want to measure the reflectivity spectrum around 100 GHz (wavelength - 3 mm) then the sample should have diameter larger than approximately 9 mm.

1.2 Principles of time-domain THz spectroscopy

1.2.1 Femtosecond laser systems

TDTS is approximately 20 years old. Unlike other spectroscopic techniques which were developed gradually, its birth can be traced rather precisely and was related to the progress in the femtosecond laser technology. Femtosecond laser sources which uses Ti:sapphire crystal as an active element have become widely available commercially within last decade and are easy-to-use nowadays.

The main principle of ultrashort pulse generation consists in the phase synchronization of the modes in the laser cavity. The mode frequencies of the laser are equal to $\nu_q = qc/2L$ (where q is an integer number, c speed of light and L the optical length of the laser cavity). The ultrafast lasers oscillate in multimode regime when the phases of the modes are fixed (locked) in time with respect to each other. It is illustrated in Figure 1.6 where the time profiles of the output energy flux (proportional to $|E|^2$) are shown for different operation regimes. Figure 1.6a shows the flux of a single mode, Figure 1.6b the result of interference of two modes, and Figure 1.6c and Figure 1.6d interference of twelve modes. In the case of Figure 1.6c, the phases of modes were chosen randomly and resulting intensity looks like a noise with weak signs of periodicity. In real laser systems the number of modes is much larger than twelve and the output intensity is quasiconstant in time. In the case of Figure 1.6d, all twelve mode have the same phase, and the time profile of the flux shows a periodic repetition of a strong pulses (note the different scales in Figure 1.6) resulting from the constructive interference of the twelve modes. It is easy to demonstrate that the period of obtained pulses $T = 2L/c$, i.e. equal to the pulse round-trip in the laser cavity. On the other hand, as it is seen in Figure 1.6, the pulse duration decreases with increase of the number of laser modes. More precisely, the pulse duration is equal to

$$\Delta\tau = \frac{2\pi}{m\Delta\omega}, \tag{1.7}$$

where m number of the laser modes and $\Delta\omega = c/2L$ distance between them [10]. Such pulses, obtained by assuming that the initial phases are rigorously equal, are said to be Fourier-transform-limited and the laser is said to be "mode-locked". From Equation 1.7 one can see that the generation of the shorter pulses requires a spectral broadening of the gain profile of active medium in the laser $\Delta\omega_{gain} \simeq m\Delta\omega$.

In order to force the laser to operate in mode-locked regime one has to modify the cavity in such a way that the pulsed radiation will have lower losses in cavity than quasicontinuous radiation. There are two main mode-locking methods developed so far:

- *passive mode-locking* resulting from the insertion of a saturable absorbing medium or another passive element into the cavity in order to select a single pulse;
- *active mode-locking* resulting from an external modulation at frequency $\Delta\omega$ either of the cavity losses (by inserting an acousto-optical crystal inside the cavity, for instance) or of the gain of the amplifying medium (synchronous pumping).

The Ti:sapphire femtosecond laser, in which mode-locking is especially simple to obtain, works in modified passive mode-locking regime, so called "self-locking" of the

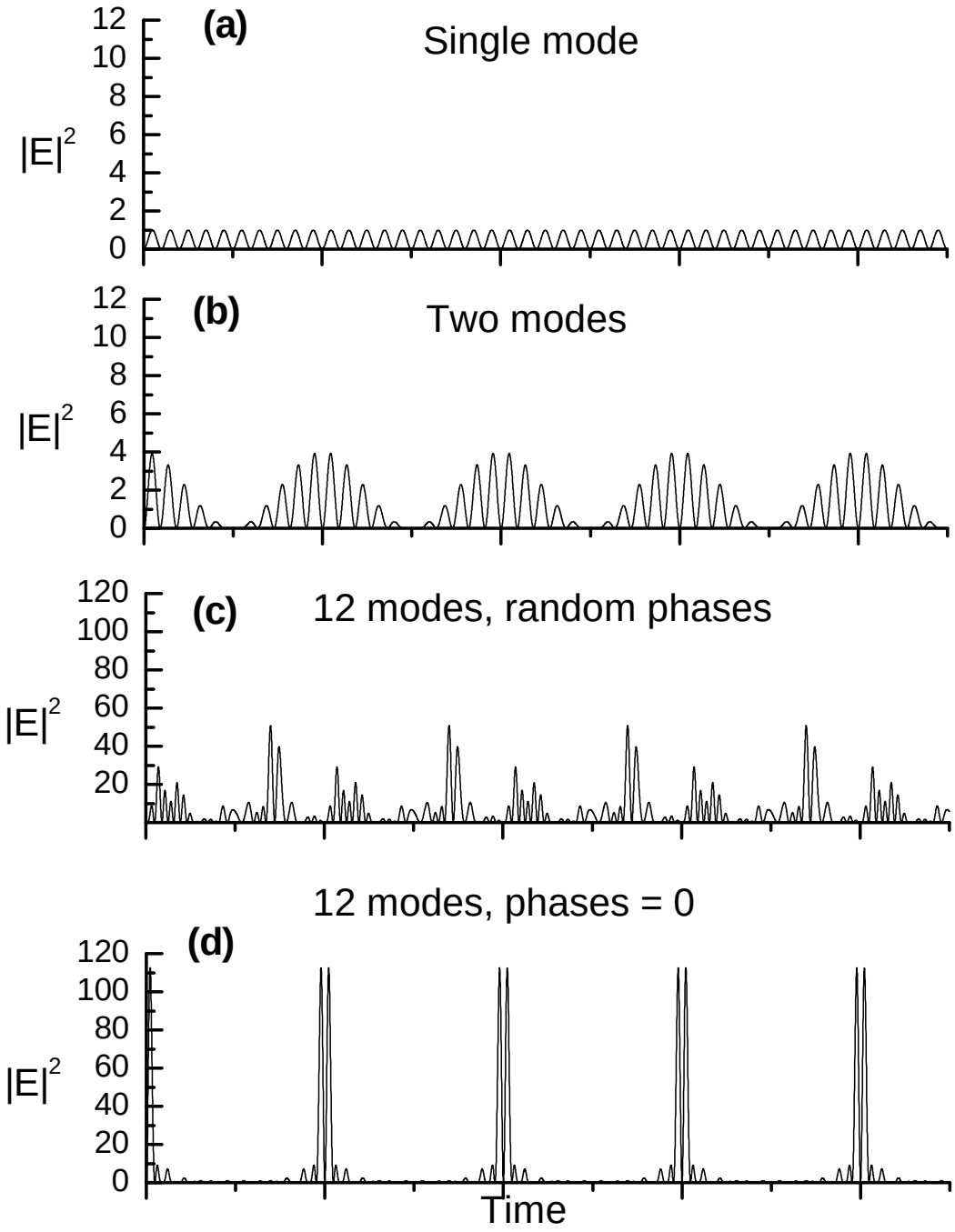

Figure 1.6: Illustration of the laser cavity modes interference resulting in pulse generation. (a) single mode, (b) two modes in phase, (c) twelve modes with random phases, (d) twelve modes with the same phase

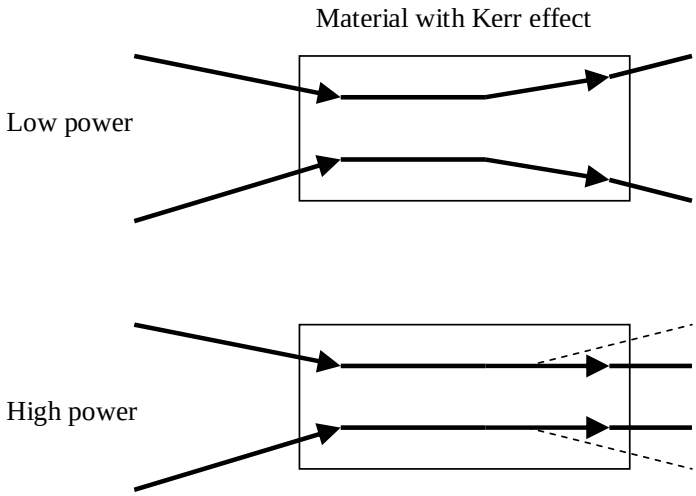

Figure 1.7: Illustration of the self-focusing by the optical Kerr effect on the beam waist of a laser beam at high and low intensity.

modes. It makes use of nonlinear properties of Ti:sapphire crystal which serves as an amplifying medium and passive nonlinear filter at the same time. The fact that the amplifying medium is nonlinear implies that its refractive index is a function of the intensity (Kerr effect): $n = n_0 + n_2 I$. The laser beam with Gaussian intensity profile therefore feels an inhomogeneous refractive index as it passes through the medium. If n_2, the nonlinear coefficient of the refractive index, is positive, the crystal behaves like a convergent lens (Kerr lens). However, such a focusing is intensity dependent. It means that the strong pulse in the laser cavity will be much more strongly focused than the weaker quasicontinuous wave (see Figure 1.7). The strong pulses, whose transverse size have been reduced, are usually less subject to losses in the cavity than the weaker intensities, which have larger cross-section, so they are enhanced. Often an adjustable slit is introduced into laser cavity to make this effect more pronounce (less focused weak radiation is cut off by the slit). Clearly, the intensity-differentiated self-focusing associated with the natural cavity losses plays a part similar to that of the saturable absorber in the passive mode-locking method.

Due to the very broad spectrum of amplification (> 50 nm at 800 nm wavelength) of Ti:sapphire and fast nonlinear response of sapphire the laser systems based on Ti:sapphire enables generation of light pulses shorter than 100 fs [10]. In our TDTS measurements femtosecond laser "Mira Seed" by COHERENT has been used for generation of ultrashort light pulses with following characteristics:

pulse length	50 - 80 fs
spectral bandwidth	15 - 40 nm
repetition rate	76 MHz
energy per pulse	8 nJ
average power	650 mW
pulse peak power	140 kW

In some cases, such as generation of THz radiation via optical rectification (see below) and other nonlinear conversions of femtosecond pulses, higher pulse energy

is required. It can be achieved using ultrafast laser amplifiers. Amplification of short pulses is similar to that of any optical radiation. A gain medium is pumped by an external source of radiation, which in most cases is a laser. Short pulses are amplified during propagation through the amplifier medium. To make amplification more efficient, multipass amplification technique is frequently used. It is based on a special cavity geometry in which amplified pulse passes through the active medium several times (typically from four to eight). In this way, total gain increases by several orders of magnitudes and pulses with energies above 1 mJ can be produced. However, a problem arises from the high fluence used in these amplifiers, which for short pulses leads to intensities above the damage threshold of the amplifying media. To avoid this problem a pulse is first stretched by a large factor (typically 1000) in order to reduce its peak power, safely amplified, and finally compressed to its initial duration [11]. Increase in the power of pulses is accompanied by decrease in the repetition rate so that the mean power does not increase dramatically. Our TDTS setup uses Quantronix "Odin" multipass femtosecond amplifier which allows to amplify femtosecond pulses generated by "Mira Seed". Amplified pulses on the output of "Odin" have following characteristics:

pulse length	50 fs
spectral bandwidth	$\approx$ 30 nm
repetition rate	1 kHz
energy per pulse	1 mJ
average power	1 W
pulse peak power	25 GW

In TDTS setup the train of ultrashort optical pulses generated by a femtosecond laser splits into two beams. The first more intense beam, so called "pump beam", serves for the generation of THz pulses, while the second much weaker "sampling" beam is used for the time resolved detection of THz pulses. There are two most commonly used ways of generation and detection of pulsed THz radiation which are described below.

1.2.2 Generation of THz pulses

Historically the first sources of coherent THz transients were based on photoconductive switches irradiated by femtosecond laser pulses [12]. The free carriers induced by the femtosecond optical pulse are accelerated in an applied electric field and emit electromagnetic radiation. Finally, the photoexcited free carriers are trapped or recombine and the current density returns to its steady value. Far from the emitter the on-axis field is given by time derivative of the current density. The exact shape of the produced electromagnetic transient depends on the characteristics of both the semiconductor material and the switch construction itself. In the case of pure monocrystalline semiconductor materials, the carrier lifetime is typically much longer than the timescale of interest, so that upon excitation the current will flow continuously in the device until the capacitance on voltage supply is discharged. Then, after the carriers recombine, the bias voltage slowly recovers its initial value; the device is ready for the next laser shot. Using this technique, subpicosecond transients have been achieved. Yet, even better performances are obtained when the current flows for the reduced

amount of time comparable with the duration of THz pulses. Several semiconducting materials have been established to have the reduced sub-picosecond carrier lifetime: radiation-damaged silicon-on-sapphire (RD-SOS) [13], low-temperature-grown GaAs (LT-GaAs) [14] and other.

There are two common schemes of photoconductive switches for THz field generation. A point source developed by Fattinger and Grischkowsky [15] consists of two aluminium electrodes separated by a few micrometers sputtered on radiation-damaged silicon. The size of emitting antenna in this case is much smaller than the generated wavelength and the device has radiation characteristics similar to that of the elementary dipole. Therefore a spherical sapphire or silicon lens has to be applied to the the emitter substrate in order to collimate emitted radiation. Another THz generation scheme was demonstrated by Hu *et al.* [16] and has a typical spacing between the electrodes of 1 cm, i.e. much larger than the wavelength of generated THz radiation. As a result, the divergence of THz beam is greatly reduced. Thus the spherical lens is not necessary in the scheme. Moreover, an important advantage of this emitter is the possibility to scale up the energy of femtosecond pump pulses, because the active area of the emitter is much larger than that of the point source. In this way, generation of THz pulses of nearly 1 µJ energy has been demonstrated [17].

Besides photoconductive switching, the nonlinear optical properties of dielectric crystals can be utilized to achieve generation of THz pulses. The effect used for this purpose is called optical rectification and takes place in noncentrosymmetric crystals. The polarization induced in a material can be written as the Taylor expansion of the electric field of the incident femtosecond optical pulse

$$P(t) = \chi_1 E(t) + \chi_2 E^2(t). \tag{1.8}$$

The electric field of short laser pulse can be expressed as

$$E(t) = A(t) \cos \omega_0 t, \tag{1.9}$$

where $A(t)$ is the pulse envelope and ω_0 is the carrier frequency. According to Equation 1.8, the induced polarization is not equal for two opposite directions of the applied electric field, if $\chi_2 \neq 0$. Then the nonlinear polarization, $P_2(t)$, can be decomposed into two terms, according to the following expression

$$P_2(t) = \chi_2 E(t)^2 = \frac{\chi_2 A^2(t)}{2} + \frac{\chi_2 A^2(t)}{2} \cos 2\omega_0 t. \tag{1.10}$$

The second term is associated with a carrier frequency $2\omega_0$ and describes the well-known process of second-harmonic generation. The first term is directly proportional to the pump pulse intensity and does not contain any carrier frequency. Thus it represents transient pulse of electric field with spectrum around THz frequency region. The effect of optical rectification has close analogy with widely-used rectification effect in electronic devices.

Optical rectification in $LiNbO_3$ observed by Yang *et al.* [18] was the first process used for the generation of microwave pulses from the picosecond laser pulses. Further development of this method allowed generation of freely propagating radiation [19] and thus its implementation to various THz experiments has become easier. An important advantage of optical rectification technique consists in a very fast polarization response

related directly to the ionic or electronic nonlinear polarizability of dielectric crystal which allows to extend the spectrum of generated THz pulses [20].

A number of materials has been used to obtain the THz radiation via optical rectification effect. Several examples can be mentioned: ZnTe crystals produce THz radiation under phase-matching conditions in the frequency range from 100 GHz up to 3 THz [21]; resonant optical rectification in GaAs [22], InP and CdTe [23] when the photon energy of the excitation beam exceeds the band gap; organic crystals with high electronic polarizability and correspondingly huge optical nonlinearity such as DAST (dimethyl amino 4-*N*-methylstilbazolium tosylate) [24] and derivatives of MNA (2-methyl-4-nitroaniline) [25].

Since the intensity of optically rectified THz signal is proportional to the square of the pump pulse intensity, the optical rectification becomes more efficient as the power of pump optical pulses increases. The efficiency of optical rectification is limited only by the process of two-photon absorption which is not negligible at high pump intensities. On the other hand, the light absorption process in the photoconductive switches saturates at lower pump intensities and the pump pulse penetrates deeper inside the semiconductor. The free carriers generated far from the surface screen the THz radiation produced near the surface. Thus the overall efficiency of THz generation does not increase proportionally to the pump intensity. Therefore photoconductive emitters are more suitable for non-amplified femtosecond laser systems, while the optical rectification is very efficient with powerful amplified ultrashort laser pulses.

1.2.3 Detection of THz pulses

In contrast to common methods of optical spectroscopy which determine the time average of the radiation intensity, TDTS measures a time profile of THz pulse electric or magnetic field. It allows extracting amplitude and phase information from a single measurement. Thus, in this respect, TDTS has similar capabilities as BWO spectroscopy. The idea of time-resolved detection consists in the gated detection of radiation. The sampling optical pulse switches on detection of THz field only during the short time compared to the duration of pulse. By varying delay between sampling and pump (or THz) pulses we can scan full time profile of the THz pulse as it is illustrated in Figure 1.8.

In analogy with the generation of THz radiation, the gated detection of freely propagating THz pulses is performed usually by photoconductive antennas [26] or electro-optic sampling [27]. In the former case, the sampling pulse generates free carriers in the gap of photoconductive dipole antenna. During the photocarrier lifetime there is a current which is proportional to the amplitude of the received THz field applied across the gap. This current is converted to a voltage by a current amplifier connected to the feed lines of the antenna [26]. Upper frequency detection limit of this structure is determined by the photoconductivity response. The photocurrent response can be written as a convolution of the transient photoconductivity $\sigma(t)$ and the THz electric field $E(t)$ across the photoconductor:

$$J(t) = \int \sigma(t - t')E(t')dt', \tag{1.11}$$

where $J(t)$ is the photocurrent transient. $E(t)$ becomes approximately proportional to $J(t)$ when the photoconductivity response time is much shorter than the THz wave-

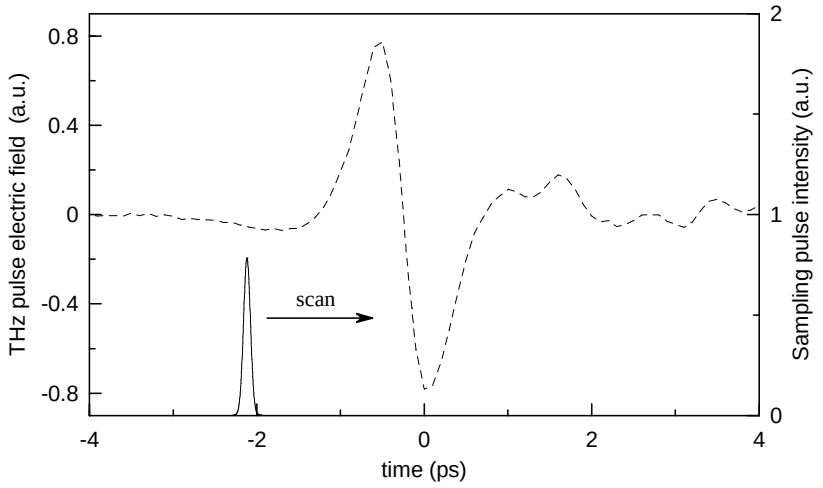

Figure 1.8: Illustration of gated detection. THz pulse (dash line), optical sampling pulse intensity (solid line).

form. Therefore only the semiconductor materials with extremely short lifetimes such as LT-GaAs (lifetime $\simeq$ 300 fs) [14] or RD-SOS and can be used in photoconductive detectors. Moreover, the electric field across the photoconductor can differ from that of the free propagating THz pulse due to the frequency-response of the antenna structure. In the approximation of point dipole, the detection efficiency is proportional to ω. Thus the low-frequency detection limit of photoconductive antennas is determined by their frequency response while the high-frequency limit depends on the photoconductivity response.

Electro-optic sampling is based on linear electro-optic effect (Pockels effect). The electric field E_{THz} of the THz pulse induces an instantaneous birefringence in an electro-optic crystal

$$\Delta n \propto E_{THz}, \tag{1.12}$$

which influences the polarization state of an optical sampling pulse which propagates collinearly with the THz pulse (Figure 1.8). In a crystal with thickness L, the phase shift between the ordinary and extraordinary part of the sampling beam is

$$\Delta\varphi = \frac{\omega}{c}\Delta n L. \tag{1.13}$$

As a result, linearly polarized sampling pulse changes into a slightly elliptically polarized pulse. After this, beam passes through a $\lambda/4$–plate which changes its polarization to almost circular. The deviation from polarization circularity then can be detected by a pair of balanced photodiodes which measure intensities of vertical and horizontal components of the sampling beam. The difference between these intensities equals

$$\Delta I = I_0 \sin\Delta\varphi, \tag{1.14}$$

where I_0 is the intensity of sampling beam. For sufficiently small values of $\Delta\varphi$ (for E_{THz} = 10 kV/cm $\Delta\varphi \approx 0.2$ rad) the measured signal is directly proportional to E_{THz}. Advantage of the described detection scheme is its insensitivity to the weak

parasite light signals because both photodiodes measure rather intense sampling signals. The difference signal is modulated by the modulation frequency of THz radiation (see Section 1.2.4) and can be reliably detected using lock-in amplifier. When the femtosecond amplified laser system is used and the repetition rate of the femtosecond pulses is of kHz order, additional improvement of the detection can be achieved using time-selective amplification by box-car amplifier. Signal-to-noise ratio (SNR) of detected THz waveform electric field higher than 10000:1 can be achieved in this case with this kind of electro-optic detection. Other electro-optic detection arrangements are not so efficient. For example, it was demonstrated that in crossed polarizers geometry the signal can be maximized by choosing appropriate (small) phase compensation so that the resulting SNR is about 200:1 only [28].

The materials which are used in optical rectification emitters of THz radiation also used for electro-optic sensors, because in both cases large nonlinear response is needed for high performance. Therefore the most popular materials for free space electro-optic sampling are ZnTe [29,30,31] which is commonly used in the range from 0.1 THz to 3 THz, GaP [32] and DAST [33].

Time-delay scans of the sampling pulse allow to determine the THz waveform using electro-optic detection. However, similarly as in the case of photoconductive detection, the measured waveform $E_{meas}(t)$ will differ from the real THz electric field $E_{THz}(t)$. In the case of ideal electro-optic crystal without any dispersion $E_{meas}(t)$ is a convolution of $E_{THz}(t)$ and the intensity profile of the sampling pulse. In the real cases, the situation is more complicated due to the group velocity dispersion (GVD) in the sensor. In a crystal with polar phonon modes appreciable difference exists between group velocity of optical and THz pulse which produces time-walkoff which increases as these pulses pass through the crystal. For example, in (011)-oriented ZnTe $n_g = 3.22$ at $\lambda = 800$ nm and $n_g \simeq 3.2$ at 1 THz [21] and the walkoff is 67 fs/mm. It means that 1 mm thick ZnTe sensor will produce walkoff which will average sensor response on 67 fs time interval. This fact together with GVD leads to the limitation of electro-optic sensor thickness and the signal value which is proportional to L (see Equation 1.13).

1.2.4 Principal schemes of TDTS setup

Transmission setup

The scheme of time-domain THz transmission spectroscopy (TDTTS) setup used in our measurements is shown in Figure 1.9. The horizontally polarized beam of femtosecond pulses generated by the laser system is divided by a beam-splitter into pump and sampling beams with intensities 96% and 4% of the initial beam. The pump beam is modulated by a mechanical chopper and excites emitter which generates THz radiation. This radiation is focused by an ellipsoidal mirror on the measured sample fixed to a diaphragm. Having passed through the sample, the THz beam is focused on the electro-optic sensor (1 mm thick (011)-oriented ZnTe) by another ellipsoidal mirror. Meanwhile, the sampling beam passes through an optical delay line and $\lambda/2$-plate which changes its polarization to vertical. Then it is directed to the sensor by a pellicle beam-splitter (several μm thick mylar, denoted by dash line in Figure 1.9) which is fully transparent for THz radiation but reflects some part of the optical sampling beam. Having passed through the sensor, the sampling beam splits into

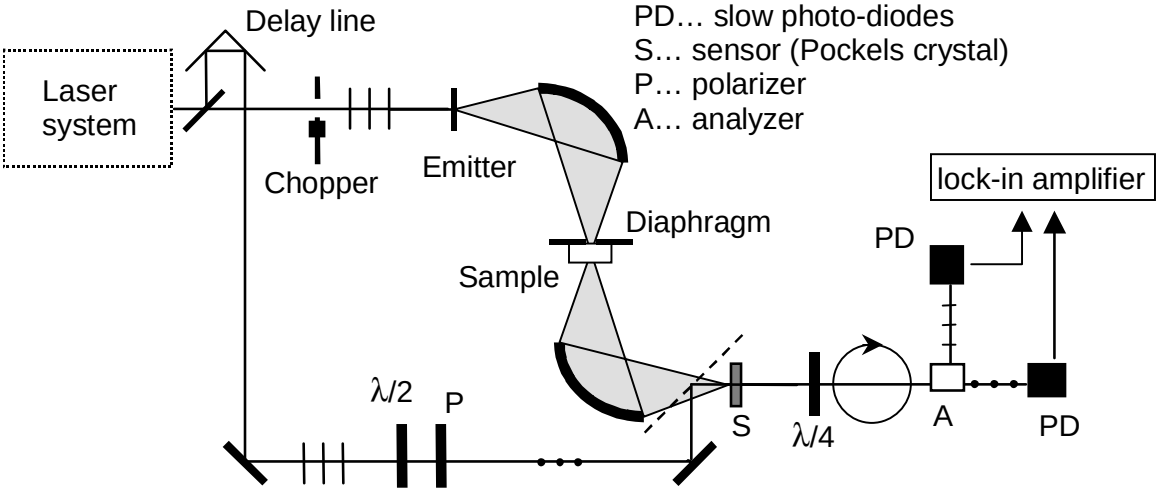

Figure 1.9: Scheme of TDTTS setup.

vertical and horizontal components by the analyzer which is the Wollaston prism in our case. The difference between intensities of these components measured by ordinary silicon photodiodes is detected by a boxcar amplifier synchronized with the repetition frequency of femtosecond pulses and then by a lock-in amplifier synchronized with the chopper frequency. The position of optical delay line is controlled by the computer. Changing the delay by small steps one is able to scan time profile of the THz waveform. The scanning limits are determined by the mechanical limits of the optical delay line.

The typical parameters of our TDTTS setup based on an amplified femtosecond laser system are listed below

pump beam power	410 mW
peak E_{THz}	5.7 kV/cm
chopper frequency	37 Hz
energy per pulse	1 mJ
SNR of E_{THz}	$\simeq 10^4$
THz frequency range	0.1 – 2.5 THz

The setup is additionally equipped with liquid He-cooled continuous flow cryostat (Oxford Optistat^{CF}) with 30 µm-thick mylar windows. It enables measurements below room temperature down to 10 K.

The described setup allows measuring the time profile of the electric field of the THz pulses. The spectroscopic method consists in the measurement of a reference waveform $E^r(t)$ with an empty diaphragm and a signal waveform $E^s(t)$ with the sample attached to the diaphragm and filling the whole aperture. Figure 1.10 shows typical example of THz signal obtained for 0.98 mm thick lithium germanate $Li_2Ge_7O_{15}$ (LGO) crystal. The "noisy" signal after the main pulses corresponds mainly to the beats of the rotational absorption lines of the water vapor [34]. The signal waveform shows two echoes accompanying the main pulse: they correspond to the reflections inside the sample. As it is pointed out in Section 1.2.3, these measured waveforms are related to the freely propagated THz signals via convolution transformation with some instrumental function $\mathcal{D}(t-t')$ which describes the sensor response and spatiotemporal

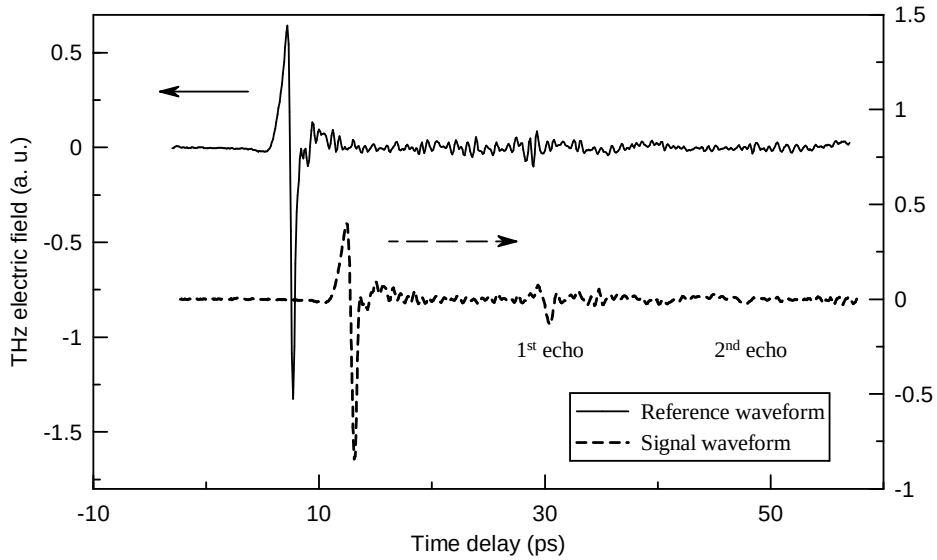

Figure 1.10: Reference (solid line) and signal (dashed line) THz waveforms obtained for the measurement of 0.98 mm thick LGO crystal along its ferroelectric axis.

transformations of THz pulses [35]

$$E_{meas}(t) = \int \mathcal{D}(t-t')E_{THz}(t')dt' \tag{1.15}$$

The Fourier components of the two signals are obtained through the fast Fourier transform and they define the complex transmission function of the sample:

$$t(\omega) = \frac{E^s_{THz}(\omega)\mathcal{D}(\omega)}{E^r_{THz}(\omega)\mathcal{D}(\omega)} = \frac{E^s_{THz}(\omega)}{E^r_{THz}(\omega)} \tag{1.16}$$

Here we consider the case of equilibrium spectroscopy (the sample properties are time-independent) and therefore can apply convolution theorem which allows to represent expression 1.15 as a simple product in frequency domain. Thus the instrumental function cancels out in the frequency dependence of the complex transmission. The Equation 1.16 demonstrates that the time-resolution does not play crucial role in standard TDTS. However, it is very important in the study of time-dependent properties, for example, in emission spectroscopy [14] and optical pump – THz probe experiments [36].

In the case of a homogeneous sample the complex refraction index $N = n + i\kappa$ is related to the complex transmission through

$$t(\omega) = \frac{4N\exp[i\omega(N-1)d/c]}{(N+1)^2}\sum_{j=0}^{m}\left[\left(\frac{N-1}{N+1}\right)\exp(i\omega Nd/c)\right]^{2j}, \tag{1.17}$$

where m is the number of reflections (echoes) inside the sample. These reflections are experimentally resolved (at least for thick samples) and form separate pulses in the measured signal so that the value of the coefficient m can be easily determined (for the case presented in Figure 1.10, $m = 2$). When the sample is optically thin, the geometrical series should be summed up to the infinity.

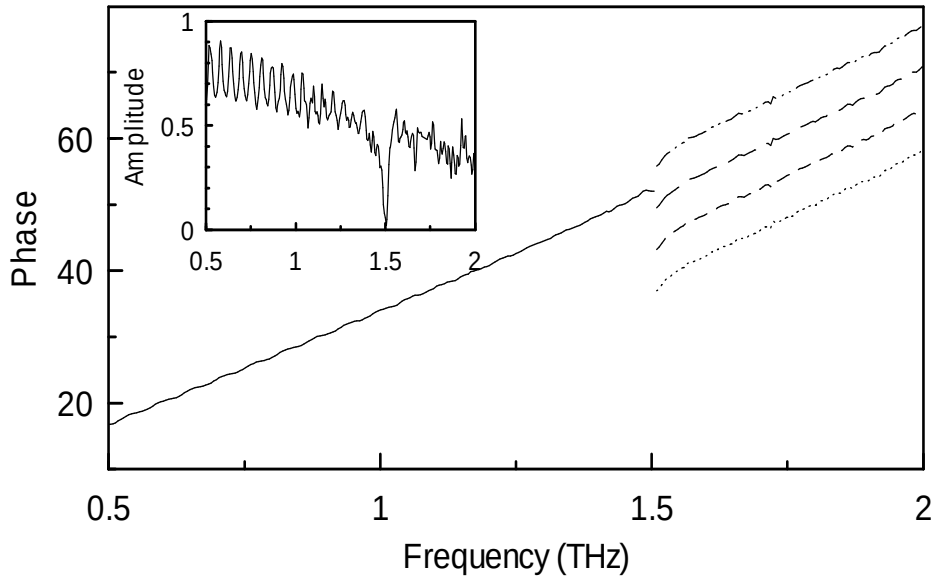

Figure 1.11: Amplitude and phase of complex transmission function of LGO sample. Different possible phase branches are shown above the resonance frequency.

Equation 1.17 constitutes two real equations for two real parameters n and κ: e.g., for $m = 0$ the expressions for the modulus t and the phase φ of the transmission function take the form

$$|t| = \frac{2\sqrt{n^2+\kappa^2}}{(n+1)^2+\kappa^2}\exp(-\omega\kappa d/c) \tag{1.18}$$

$$\varphi + 2\pi l = \frac{\omega(n-1)d}{c} - \arctan\left(\kappa\frac{n^2+\kappa^2-1}{n(n+1)^2+\kappa^2(n+2)}\right) \tag{1.19}$$

The first right-hand side term of Equation 1.19 accounts for the decrease of the phase velocity during the propagation in the sample; the second one, which constitutes usually only a small correction, describes the phase change on the interfaces. The phase is defined by the Fourier transform of the experimental data and ranges from 0 to 2π; the term $2\pi l$ is added to obtain the right order of the phase displacement. The integer parameter l can be determined for the frequency which corresponds to the maximum of transmitted spectrum by estimation of refractive index from the measured time delay between the signal and the reference pulses [$\Delta t = (n-1)d/c$]. The equations can then be solved numerically for n and κ. The same approach is in principle valid for $m \neq 0$: one obtains slightly more complicated expressions analogous to 1.18, 1.19 which can be solved numerically.

The situation becomes more complicated when the THz spectrum of the sample contains a very sharp dielectric resonance. The difficulty then comes from the fact that, due to the low spectral resolution or due to the weakness of the signal, it is not immediately clear how many orders of the phase are swept near the resonant frequency (i.e. what is the strength of the related dielectric anomaly). As TDTTS allows to access independently both the real and the imaginary part of the dielectric function, which, in turn, should satisfy the Kramers-Kronig (KK) relations [37], it is

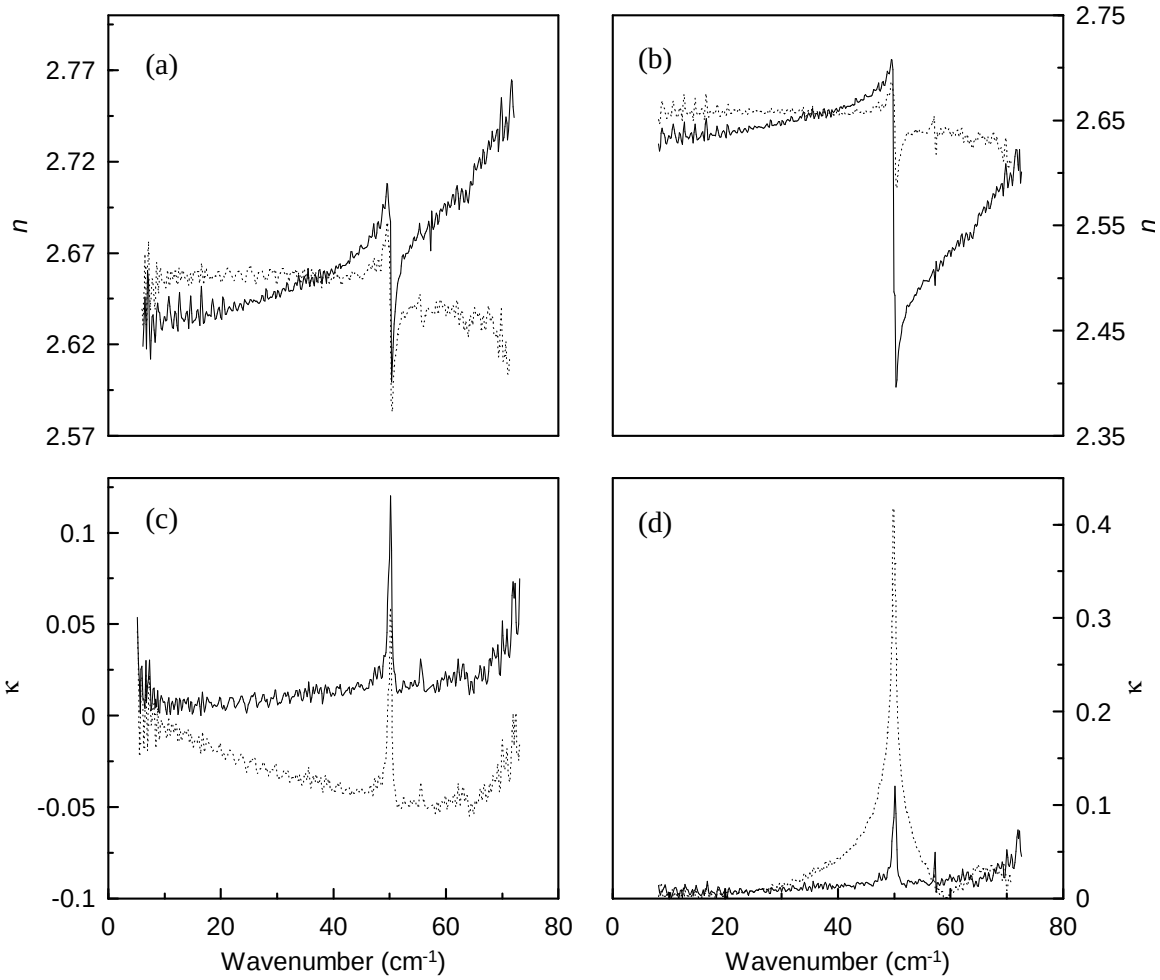

Figure 1.12: Refractive (a),(c) and absorption (b),(d) indices of LGO calculated for two adjacent phase branches (solid lines) compared with the results of KK analysis (dotted lines)

then possible to use these relations to leave the remaining ambiguity. To illustrate this procedure we use the data obtained for the LGO crystal, which presents a sharp low-frequency phonon at about 1.5 THz for the electric field polarized along polar c-axis [38]. The transmission function of a LGO sample is shown in Figure 1.11. The interference fringes of the amplitude are due to the sample internal reflections (see Figure 1.10). The values of the phase displacement for the frequencies below the phonon resonance are determined from the measured time delay between the reference and signal pulses; the correct phase branch at high frequencies needs to be determined through the KK analysis. Couples of possible n and κ coming from different branches can be determined through Equation 1.17. However, only the true n and κ should satisfy the KK relations. The results of numerical solution of Equation 1.17 and their KK analysis for LGO are shown in Figure 1.12 (only the results related to the two dashed curves in Figure 1.11 were represented here). The solid lines in Figure 1.12 present the refractive (absorption) index calculated using Equation 1.17 and the dotted lines are obtained through application of KK relation to the absorption (refractive) index calculated from the same equation.

Comparison between the strength of the dielectric resonance in original data and the data obtained through KK analysis immediately shows that n and κ in Figures 1.12a and 1.12c are correct whereas the data depicted in Figures 1.12b and 1.12d correspond to the wrong phase branch. Appreciable disagreement between original and KK spectra even in the case of the correct phase branch come from the fact that KK relations, which require knowledge of dielectric spectra from 0 to ∞, were applied to the limited frequency region of TDTS. However, the strength of the resonance (peak value of absorption and the step value in refractive index) is not much affected by this rough modification of KK relations [39].

Transmission spectroscopy of the films on transparent substrates is similar to that of bulk samples. One has to perform an additional measurement of a bare substrate. Then the complex transmission function can be obtained using the THz waveform transmitted through the bare substrate as a reference. The complex refractive index of the film can be calculated by numerically solving the equation for complex transmission of a two-layer system. Usually $N_f d_f/c \ll 1$ for thin film (where N_f refractive index and d_f thickness of the film). Within this approximation one can obtain explicit analytic expression for the complex refractive index of thin film [40]

$$N_f^2 = \frac{ic(1+N_s)}{\omega d_f}\left[\frac{1}{t(\omega)}\frac{\exp[i\omega(N_s-1)(d_s-d_s')/c]}{1+i\omega d_f/c}-1\right]-N_s \qquad (1.20)$$

where N_s is the refractive index of the substrate, d_s and d_s' thicknesses of sample and bare substrates, respectively. Since the thickness of the substrate is much larger than that of the thin film, the phase shift due to the propagation of THz radiation through the film is usually small comparing to the substrate phase shift. Therefore the value of calculated refractive index (especially its real part) is strongly affected by unavoidable errors in the determination of the substrate thickness and refractive index [40]. Nonetheless, TDTTS of thin films often can be rather successfully applied to ferroelectric thin films [41].

Reflection setup

Time-domain THz reflection spectroscopy (TDTRS), in analogy with TDTTS, requires also a reference measurement which can be obtained e.g. using a reflection on a mirror with known characteristics. The main difficulty in realization of TDTRS consists in a correct determination of the reflectance phase which is strongly affected by errors in the relative position of the sample and reference mirror as it was demonstrated in Section 1.1.3. To avoid the problem of the phase uncertainty in TDTRS, several different approaches were used. One of them consists in substitution of the reference signal by a signal reflected from the sample under specific conditions. Howells and Schlie [42] have investigated in this way the low-temperature dielectric function of undoped InSb taking as a reference the waveform obtained at 360 K. They used the fact that the reflectance of InSb at high temperature is comparable to that of a silver mirror due to the narrow band gap of the material. Thrane *et al.* [43] have measured the refractive index of liquid water in a silicon cell using the signal reflected from the air-silicon interface as the reference and the signal from silicon-water interface as the sample waveform. Such methods make use of the sample properties and can be applied only in particular cases. Other methods similar to ellipsometry extract the complex dielectric function from the s- and p-polarized THz signals reflected from the

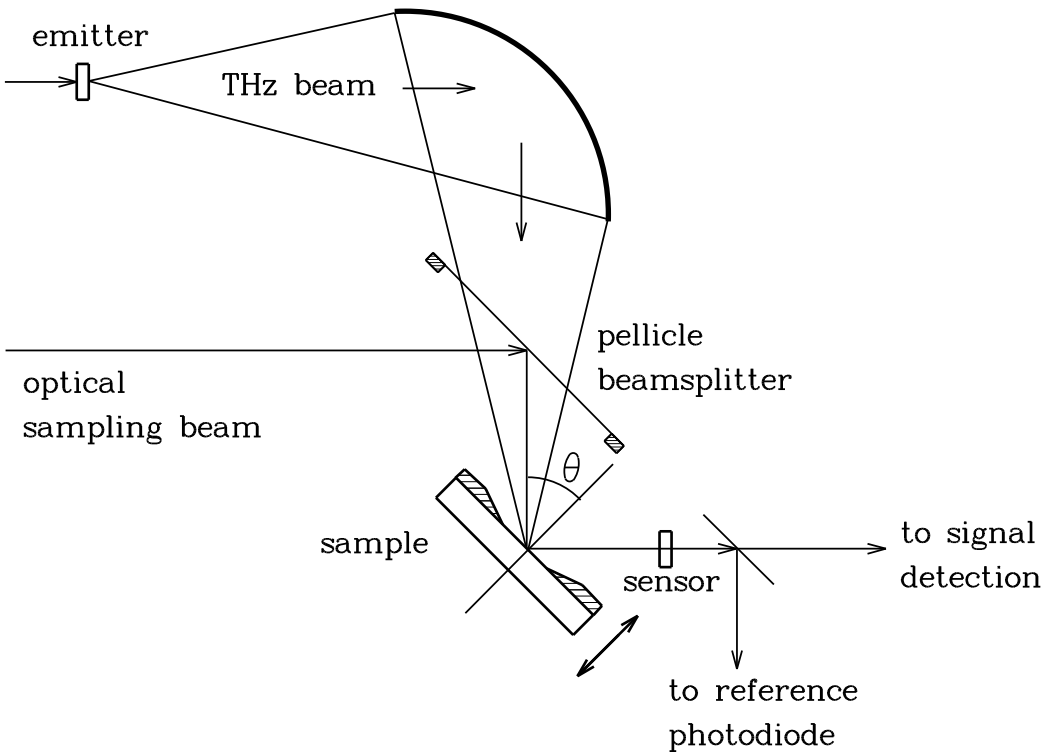

Figure 1.13: The scheme of TDTRS experimental setup.

sample at high angles of incidence [44, 45]. This approach provides very satisfactory results in some cases. On the other hand, it requires good quality THz polarizers and, for highly reflective samples, it is necessary to measure under angles of incidence close to 90°, which restricts the measurements only to homogeneous samples of large dimensions. In the case of TDTRS with a reference mirror, the uncontrollable time shift of reference pulse can be *a posteriori* adjusted to fit some model of the dielectric response [46] or to minimize the difference between the measured and calculated interference pattern in a silicon slab attached to the sample surface [47]. The last method does not use any assumption about dielectric behavior of the sample, but it is rather difficult to realize a good optical contact between the sample and the slab. Recently Hashimshony et al. [48] have succeeded in performing TDTRS measurement of epitaxial semiconductor layers using a special sample holder which allowed to replace the reference mirror by the sample with an accuracy of 1 µm. However, this is not an easy task, and in some cases even this precision is not sufficient for correct determination of the dielectric function.

We have developed a new approach to the TDTRS able to provide in many cases an easy and accurate measurement of the phase of complex reflectance [49]. It has been tested using different types of samples which were chosen to illustrate the potential applications of the method.

Figure 1.13 shows schematically the relevant part of TDTRS experimental setup. The key idea lies in overlapping of the optical sampling and THz beams between the mirror and the sample in contrast to usual arrangements where the overlap occurs between the sample and the sensor. In this geometry both beams propagate collinearly and reflect from the sample surface: the angle of incidence (and reflection) is denoted

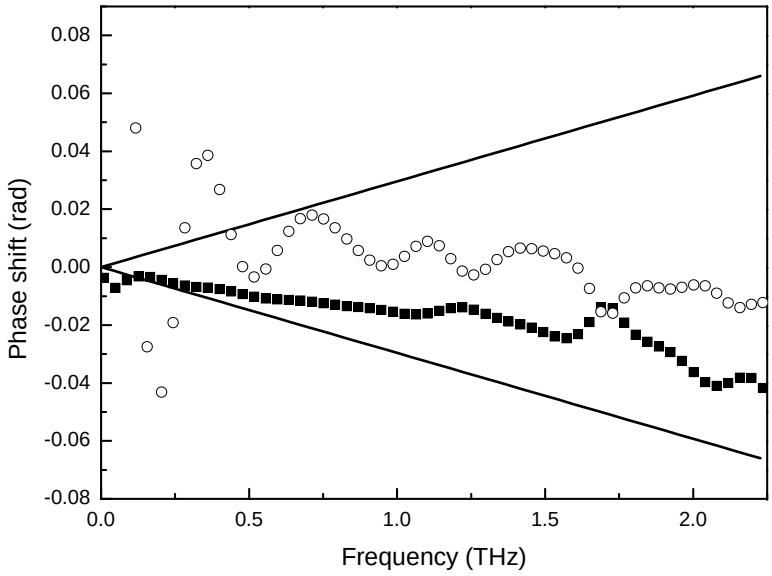

Figure 1.14: Measured phase difference introduced by 10 µm (full squares) and 1 mm (open circles) shifts of the reference mirror. The area between the full lines corresponds to an error in sample position smaller than 1 µm; angle of incidence $\theta = 45°$; p polarization.

θ. To maximize the clear aperture for the THz beam, θ should be kept small, however, in practice, θ needs to be larger than about 10°. Figure 1.13 shows the geometry with $\theta = 45°$ which is of particular interest as it is suitable for measurements in a standard cryostat with perpendicular windows. The reflected signal is detected using the electro-optic effect by a ZnTe [011] sensor which is placed directly after the sample. Measured THz waveforms are normalized by the value of the reference photodiode which is proportional to the intensity of the sampling beam. Thus the difference in optical reflectance of the reference mirror and of the sample is taken into account. The major feature of the setup is that a displacement of the sample changes the length of the optical path by precisely the same amount for both (THz and optical) beams, and produces no phase change in the measured THz waveform. To illustrate this, we have performed measurements of the THz signal for different positions of a gold mirror shifting it as shown by the arrow in Figure 1.13. It has been found that even a 1 mm shift from the initial position in both directions does not change the THz waveform. Figure 1.14 shows the phase differences between THz pulses measured with the mirror shifted by 10 µm and 1 mm. The area between the lines corresponds to the mirror shift less than ± 1 µm. It can be seen in Figure 1.14 that the phase error does not depend on the mirror shift. The limiting factor for the phase reproducibility is then the temporal stability of the whole setup rather than the precise positioning of the sample. Similarly, the described setup is not sensitive to the errors in relative angular alignment of the sample and reference mirror. The absence of a focusing mirror after the sample allows to avoid a large number of problems due to e.g. possible lower optical quality of a surface or deviation of the mirror shape from the ideal one. Indeed, focusing of the THz beam onto the sensor is not necessary as the standard THz experiments offer a very good signal-to-noise ratio nowadays.

The suitable samples for the measurements have to fulfill the following require-

ments: (*i*) optically flat surface allowing a non-diffusive (specular) reflection of the sampling beam and (*ii*) absence of secondary reflections of the sampling beam from the rear side of the sample. According to our experience, the majority of crystalline and ceramics samples can be polished with a sufficient precision to fulfill the former condition. The latter condition is critical for optically transparent samples where the echo of the sampling beam from the back side of the sample adds a systematic error to the voltage on the reference photodiode and is responsible for several replicas of the THz pulse in the measured waveform. In particular, this situation occurs in thin films on optically transparent substrates or in dielectric single crystals. In these cases, roughening or blackening of the back surface of the sample can substantially reduce the echo intensity to such extent that it can be neglected. Usually the measurements performed using p-polarized THz pulses are preferable, because this polarization is expected to be less sensitive to the errors due to mispositioning of the sample and reference mirror [49].

As an example of TDTRS we present here measurement of ferroelectric $SrBi_2Ta_2O_9$ (SBT) ceramics which is a promising material for applications in ferroelectric memories [50]. A study of IR reflectivity revealed rather strong polar phonon mode near below 30 cm^{-1} at room temperature [51]. However, this frequency region is hardly accessible to FTIR spectroscopy (signal from the source is weak) and the measured power reflectivity allows to obtain the complex permittivity only by fitting with a model dielectric function. Therefore a direct measurement of the complex permittivity can be useful for the correction and improvement of FTIR data.

We have studied the reflectivity of SBT ceramic using three different arrangements: (*i*) 12.5° incidence, p polarization, (*ii*) 45° incidence, p polarization, and (*iii*) 45° incidence, s polarization. The measured complex reflectivity and calculated permittivity of SBT ceramics together with a fit of FTIR reflectivity are presented in Figure 1.15. It has to be pointed out that the peak in the relative phase which occurs near 40 cm^{-1} for SBT corresponds to the frequency of a longitudinal phonon mode, while the imaginary part of the permittivity (dielectric loss) peaks at the position of the transverse resonance near below 30 cm^{-1}. One can see that TDTRS is able to reproduce correctly the mode structure at higher frequencies and brings a valuable information down to at least 10 cm^{-1}. The complex permittivities measured in different arrangements are in agreement with each other: it demonstrates the reliability of the presented technique.

Another field of application of TDTRS is the measurement of thin films on substrates. TDTTS sometimes does not offer a sufficient sensitivity to provide a precise information about the optical constants of the thin film. This is due to a large difference between the thicknesses of the film and of the substrate: the phase change of the THz signal induced by the thin film is in most cases much smaller than the phase change owing to the substrate [40]. Thus the evaluation of the transmittance related to the thin film exhibits a large error. In this case, TDTRS can bring a valuable information about such structures because the radiation reflected on the air – thin film – substrate interfaces is no more affected by the substrate thickness.

A 5.5 µm thick SBT film on a (0001) sapphire substrate has been characterized in reflection as well as in transmission geometry. For the transmission measurements, the THz pulse transmitted through bare sapphire substrate was used as the reference and the complex permittivity was numerically calculated in a standard way. The

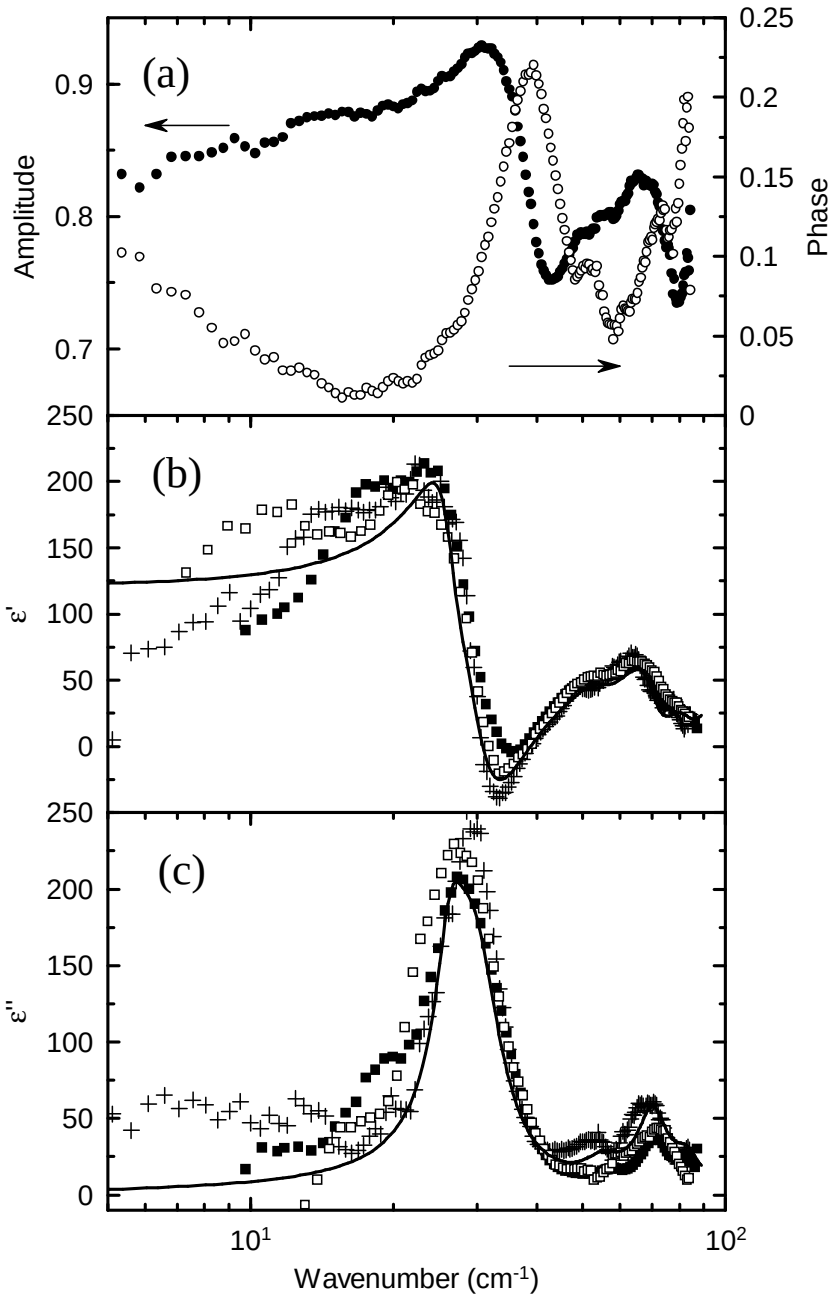

Figure 1.15: Complex reflectivity and dielectric permittivity of SBT ceramics from TDTRS measurements. (a) Complex reflectivity for $\theta = 12.5°$, p polarization; (•) amplitude, (○) phase. (b) dielectric constant, (c) dielectric loss; (+) $\theta = 12.5°$, p polarization, (■) $\theta = 45°$, p polarization, (□) $\theta = 45°$, s polarization; lines: fit of classical FTIR reflectivity data based on a sum of damped harmonic oscillators.

reflection measurement was performed using the p-polarized THz pulses with 45° incidence on the sample with blackened back surface to avoid the above-mentioned multiple reflection of the optical sampling beam inside the sapphire substrate. The complex reflectance was calculated taking into account only the THz pulse reflected from the front surface of the sample. Fabry-Pérot interferences inside the substrate were cut off (time windowing). Additional correction was made to take into account multiple reflections of the sampling beam inside the film. Usually the thickness of thin films is smaller than 1 µm and the delay of the sampling beam echoes is negligible compared to the duration of the sampling pulse (typically 50–100 fs). In our case (film thickness $d = 5.5\,\mu\text{m}$) a special care has to be taken in order to deconvolute the influence of the Fabry-Pérot reflections of the sampling beam inside the film. The time delay of the sampling pulse needed for its propagation back and forth through the film is equal

$$\Delta t = \frac{2n^2 d}{c\sqrt{n^2 - \sin^2\theta}}, \tag{1.21}$$

where n is optical refractive index of the thin film and d is its thickness. We deduced the optical refractive index of SBT from ϵ_∞ obtained by means of FTIR measurements on the SBT ceramics: $n = 2.45$; the corresponding time delay is $\Delta t = 94$ fs. Thus the sampling pulse is divided into a sequence of pulses with decreasing amplitude and separated in time. The detected THz waveform can be written in the form

$$y(t) = \frac{y_0(t) + a y_0(t + \Delta t) + \ldots}{1 + a + \ldots}, \tag{1.22}$$

where $y_0(t)$ is the deconvoluted waveform (*i.e.* free of artifacts due to the multiple reflections of the sampling beam), $a = 0.025$ is the ratio of intensities of the first two sampling pulses calculated using the Fresnel equations. The denominator of Equation 1.22 accounts for the normalization of the signal by the voltage in reference photodiode. In view of small value of a, all the higher order terms in (1.22) can be neglected. Transforming (1.22) into the frequency domain and dividing it by the spectrum of reference pulse we obtain for the complex reflectance

$$r_0(\omega) = r(\omega)\frac{1 + a}{1 + a e^{-i\omega\Delta t}}\,, \tag{1.23}$$

where $r(\omega)$ is the measured reflectance and $r_0(\omega)$ is the corrected one which should be used for the evaluation of the dielectric properties. Such a correction mainly leads to changes in the imaginary part of permittivity. In the case of SBT film it increases the value of the dielectric loss peak by about 7 %. The complex permittivity was calculated by numerically solving the system of two equations derived by Berreman [52] which relates the complex reflectance of a thin film on substrate at arbitrary angles of incidence to the dielectric constants of the thin film and substrate. The resulting complex permittivity of both transmission and reflection measurements and a fit of the transmission data by two damped harmonic oscillators are shown in Figure 1.16. The fit yields the following parameters of the soft-mode: $\nu_0 = 28\ \text{cm}^{-1}$, $\gamma_0 = 26\ \text{cm}^{-1}$ and $\Delta\epsilon_0 = 54$. For comparison we show also the complex permittivity calculated from the amplitudes of reflectance and transmittance (disregarding the respective phases). Comparison between transmission and reflection THz spectroscopies in the case of thin films leads us to three important points:

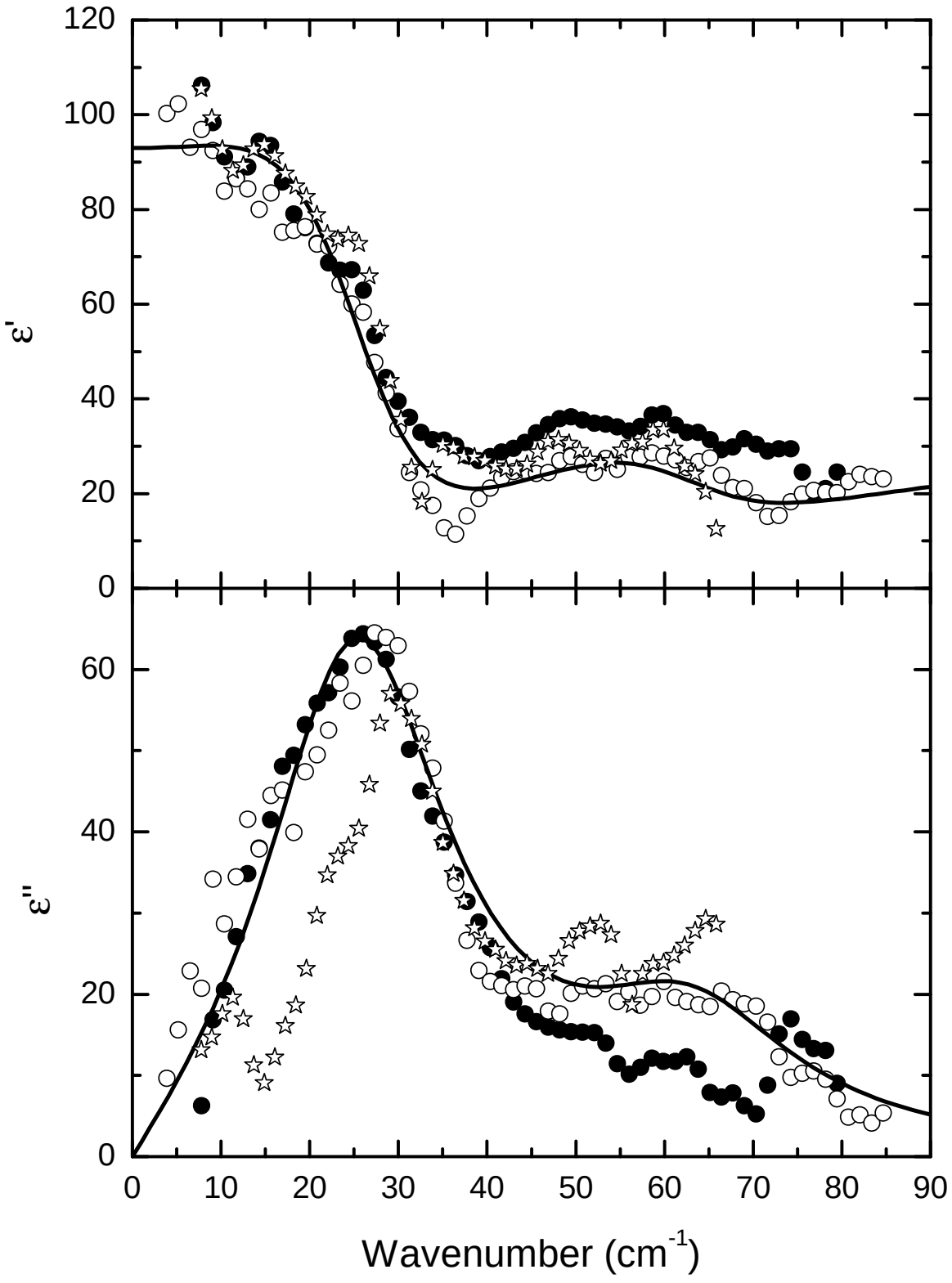

Figure 1.16: Real and imaginary part of permittivity of thin SBT film calculated from the measurement of complex transmittance (open circles), complex reflectance (full circles, p polarization, $\theta = 45°$) and amplitudes of reflectance and transmittance (open stars). Full lines correspond to the fit of the transmission data.

(*i*) The transmission data can be influenced by a large error in the static value of permittivity and in the strength of modes due to the uncertainty in the substrate thickness [40]. In contrast, the substrate thickness does not play any role in the reflection experiment. Hence, one can use e.g. the static value of the dielectric constant — or any other particular value — as determined by the reflection experiment for a small correction (within 1 or 2 microns) of the substrate thickness: trial substrate thicknesses can be used during the transmission data evaluation in order to match the resulting permittivity with that obtained from the reflectance. Such an approach has been used to evaluate the transmission data shown in Figure 1.16.

(*ii*) The evaluation of complex permittivity using reflectance and transmittance amplitudes is indeed possible; moreover it does not require the value of the substrate thickness for transparent substrates. However, our experience shows that the results obtained by this method are not as accurate as the results of phase sensitive methods: note the appreciable error in the imaginary part of the permittivity in Figure 1.16.

(*iii*) The data obtained from the transmission measurement using the above described procedure fulfill slightly better the Kramers-Kronig relations than those obtained from the reflectance only. In this respect, if the substrate thickness is very precisely known, the transmission experiment seems to provide slightly more accurate data for this film. The transmission and reflection experiments are thus complementary in this sense and their combination allows an unambiguous determination of the dielectric strength of the detected polar modes.

1.3 Fourier Transform Infrared Spectroscopy

FTIR spectrometer is an instrument which acquires broadband from near to far IR spectra. Unlike a dispersive instrument, i.e. grating or prism monochromator, a FTIR spectrometer collects all wavelengths simultaneously (so called Fellgett advantage). In fact FTIR spectroscopy is a method of obtaining infrared spectra by first collecting an interferogram of a sample signal using an interferometer, and then performing a Fourier Transform (FT) on the interferogram to obtain the spectrum [1]. The advantages of FTIR spectrometer over a dispersive instrument are

- broad spectral range 10-10000 cm^{-1}
- high spectral resolution of 0.1 to 0.05 cm^{-1} which is mostly sufficient for solid-state spectroscopy, is easily accessible
- fast spectra acquisition rate
- high signal-to-noise ratio

Due to these features FTIR spectroscopy has become the main tool for IR spectroscopy of solids. There are different commercially available FTIR spectrometers but all of them work according to the same principles.

An FTIR spectrometer is typically based on a Michelson interferometer; its principal scheme is shown in Figure 1.17. The mercury arc lamp or the SiC rod (globar) are usually used as the sources of IR radiation since the thermal sources have a rather weak spectral intensity in the far IR. The interferometer consists of a beam splitter, a fixed mirror, and a mirror that translates back and forth, very precisely. The

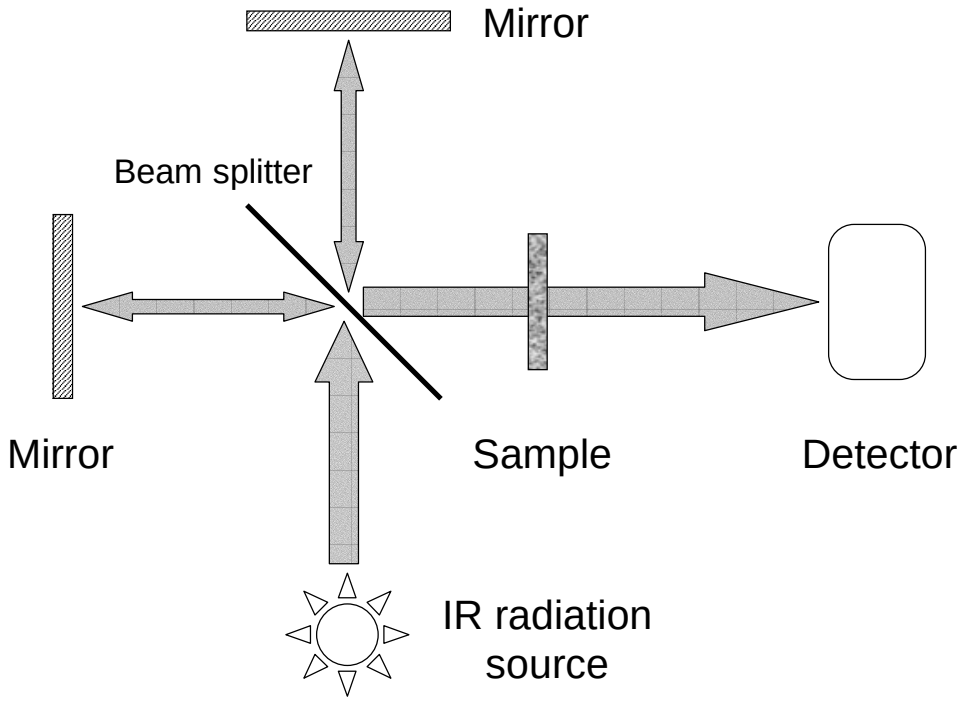

Figure 1.17: Scheme of FTIR spectrometer.

beam splitter is made of a special material that transmits approximately half of the radiation striking it and reflects the other half. The different beam splitters such as coated mylar and metal grids are used for the different parts of IR spectrum. Radiation from the source strikes the beam splitter and separates into two beams. One beam is transmitted through the beam splitter to the fixed mirror and the second is reflected off the beam splitter to the moving mirror. The fixed and moving mirrors reflect the radiation back to the beam splitter. Again, half of this reflected radiation is transmitted and half is reflected at the beam splitter, resulting in one beam passing to the detector and the second back to the source. The detector measures the power of incident IR radiation passed through the sample. DTGS pyroelectric detectors and helium-cooled silicon bolometers are usually used for the detection of IR signal in FTIR spectrometers. The measurement consists in recording of signal on detector dependence on the position of movable mirror. The resulting function is called interferogram. It is usually significantly more complex looking than a single sinusoid, which would be expected if only a single wavelength of light was present. The centerburst, the big spike in the center of interferogram on Figure 1.18a is a telltale signature of a broadband source. Its origin lies in the fact that all wavelengths are in-phase at the zero optical path difference. Therefore, their contributions are all at maximum and a very strong signal is produced by the systems detector. As the optical path difference grows, different wavelengths produce peak readings at different positions and, for a broadband signal, they never again reach their peaks at the same time. Thus away from centerburst, the interferogram becomes a complex looking oscillatory signal with decreasing amplitude.

Once an interferogram is collected, it needs to be translated into a spectrum. The process of conversion is through the Fast Fourier Transform algorithm. The discovery of this method in 1965, followed by an explosive growth of computational power at affordable prices, has been the driving force behind the market penetration

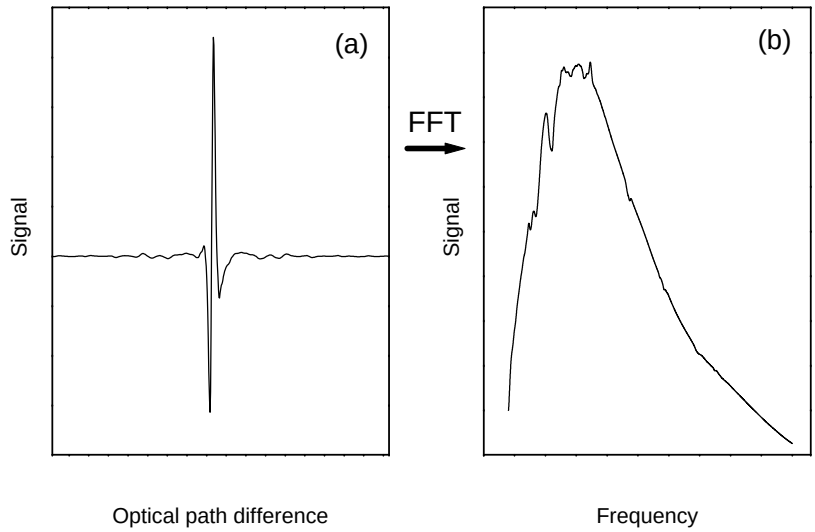

Figure 1.18: Interferogram and spectrum in FTIR spectroscopy.

of FTIR instruments. The power spectrum obtained by the Fourier transform of the corresponding interferogram is shown in Figure 1.18b. The high frequency limit of the spectrum is determined by the interferogram resolution and the power spectrum of the source. At the same time, the frequency resolution depends on the scan length of interferogram. The resolution limit is simply an inverse of the achievable optical path difference. Therefore, a 2 cm scan capable instrument, for instance, can reach 0.5 cm^{-1} resolution. Transmission or reflection functions then can be obtained in the way similar to TDTS and BWO spectroscopy as the ratio of sample and reference spectra. However in FTIR experimental arrangement depicted in Figure 1.17 the sample is placed outside of the interferometer branches and does not produce phase change in the interferogram. Thus presented FTIR spectrometer setup provides only *power* transmission or reflection spectra in contrast to TDTS and BWO spectroscopy.

Phase-sensitive FTIR spectroscopy is possible when the sample is placed in the interferometer branch with the fixed mirror. It is able then to determine complex refractive index as in TDTS. A comparison of these two methods shows that TDTS has better signal-to-noise ratio than FTIR spectroscopy at frequency below 3 THz, while the opposite is true at over 5 THz [53]. However phase-sensitive arrangement of FTIR spectrometer causes numerous difficulties in measurement and is not used in commercially available spectrometers.

In order to extract the information about complex refractive index or permittivity of the sample from measured power spectrum one has to use additional assumptions. There are two different ways in doing this. First, one has to assume that the measured spectrum is broad enough to satisfy Kramers-Kronig relations for permittivity [37]:

$$\epsilon'(\omega) - 1 = \frac{2}{\pi} P \int_0^\infty \frac{\omega' \epsilon''(\omega')}{\omega'^2 - \omega^2} d\omega' \tag{1.24}$$

$$\epsilon''(\omega) = -\frac{2\omega}{\pi} P \int_0^\infty \frac{\epsilon'(\omega') - 1}{\omega'^2 - \omega^2} d\omega' \tag{1.25}$$

where P designates the principal value of the integral. Then the phase of reflectivity (normal incidence) can be calculated using the amplitude:

$$\phi(\omega) = -\frac{2\omega}{\pi} P \int_0^\infty \frac{\ln r(\omega')}{\omega'^2 - \omega^2} d\omega'. \tag{1.26}$$

The complex refractive index can be calculated using Equation 1.3.

The second way consists in modeling of dielectric response using some number of independent parameters. The power reflection function can be simulated then using expression

$$R(\omega) = \left| \frac{\sqrt{\epsilon^*(\omega)} - 1}{\sqrt{\epsilon^*(\omega)} + 1} \right|^2 \tag{1.27}$$

In the case of dielectric materials the dielectric contribution of polar phonon modes can be described by the sum of n classical damped harmonic oscillators

$$\epsilon^*(\omega) = \epsilon'(\omega) - i\epsilon''(\omega) = \sum_{j=1}^{n} \frac{\Delta\epsilon_j \omega_{TO_j}^2}{\omega_{TO_j}^2 - \omega^2 + i\omega\gamma_{TO_j}} + \epsilon_\infty \tag{1.28}$$

or more generally by a factorized form [54]

$$\epsilon^*(\omega) = \epsilon_\infty \prod_{j=1}^{n} \frac{\omega_{LO_j}^2 - \omega^2 + i\omega\gamma_{LO_j}}{\omega_{TO_j}^2 - \omega^2 + i\omega\gamma_{TO_j}}, \tag{1.29}$$

where ω_{TO_j} and ω_{LO_j} are the transverse and longitudinal frequencies of jth polar phonon mode, respectively, γ_{TO_j} and γ_{LO_j} their respective damping constants, $\Delta\epsilon_j$ is the jth mode contribution to the static permittivity and ϵ_∞ the optical permittivity due to the electronic polarization processes. The values of these parameters are varied during the fitting procedure to obtain the best correspondence between the measured and modeled reflection or transmission functions.

The four-parameter oscillator Equation 1.29) follows from the general properties of dielectric function in a polarizable lattice (pole at transverse and zero at longitudinal eigenfrequencies of polar phonons) and is able to describe the permittivity of the substance in most cases. However one has to pay attention during the fitting because an arbitrary combination of parameter values in Equation 1.29 can sometimes result in unphysical values of complex permittivity (for example, negative losses). There are necessary conditions which should be fulfilled by the parameters of the factorized oscillator model. In the simple case of single oscillator ($n = 1$) we have

$$\begin{aligned} \omega_{LO} &> \omega_{TO} \\ \gamma_{LO} &\geq \gamma_{TO} \\ \frac{\omega_{LO}^2}{\omega_{TO}^2} &\geq \frac{\gamma_{LO}}{\gamma_{TO}} \end{aligned} \tag{1.30}$$

Classical oscillator model described by Equation 1.28 uses only three parameters for each fitted mode and is more stable from this point of view. Moreover there are no restrictions for the values of parameters and the modeled dielectric losses are always positive. However classical model is not general and in some cases (namely,

asymmetrical dielectric resonances) it fails to describe dielectric function correctly. The four-parameter factorized oscillator model has to be applied in this situation.

Additional advantage of the fitting over the Kramers-Kronig analysis is that after fitting one automatically obtains the parameters of polar phonon mode which can be directly compared with the data obtained by other spectroscopic method (for example Raman spectroscopy). Moreover the fitting can be performed taking into account directly measured complex permittivity in THz and/or GHz range improving the fit quality in far IR region.

All far-infrared reflectivity measurements presented in the thesis were performed using a Fourier transform spectrometer Bruker 113v with He-cooled bolometer or DTGS detectors. Spectral range was 30-5000 cm^{-1}, typical resolution about 0.5 cm^{-1}. Low temperature measurements in far infrared range were carried out in helium cryostat Oxford Optistat^{CF} with polyethylene windows. Silver mirrors sputtered on glass substrates were used for reference (background) measurements.

Part 2

THz spectroscopy of microwave ceramics

Microwave (MW) low-loss ceramics are nowadays widely used as MW dielectric resonators in MW integrated circuits. The basic requirements for MW resonators are small size, high quality factor and good temperature stability. Ceramic technology allows to prepare relatively cheap materials with defined properties for industrial applications. The aim of this technology is to produce materials with relatively high and temperature independent permittivity and with losses as low as possible to fulfill the requirements of MW integrated circuits. It appears that, despite of high permittivity, ferroelectrics are not good candidates for MW resonators because of high losses and strong temperature variation of permittivity. Therefore researchers are looking for materials "related" to ferroelectrics in the sense of a high ionic polarizability of their lattice. At the same time, anharmonic effects in the lattice should not be very strong to prevent from the temperature instability and transition into ferroelectric phase. Permittivity of such materials is about $\epsilon' = 20 \div 100$ and does not strongly depend on temperature. Thus the minimization of losses ϵ'' or increase of quality factor $Q = \epsilon'/\epsilon''$ in the whole MW range ($1 \div 100$ GHz) is a very challenging task.

Dielectric losses in MW materials consists of *intrinsic losses* which are fundamental losses of ideal crystalline material and *extrinsic losses* caused by lattice defects. Intrinsic losses are related to the polarization mechanisms in the perfect lattice and do not depend on material preparation method. On the other hand, extrinsic losses can be in principle removed by proper material processing. Various types of defects can cause extrinsic losses: point defects (isotopes, dopant atoms, vacancies, defect pairs, positional disorder in complex system), linear defects (dislocations), planar defects (grain boundaries) and other bulk defects (pores, inclusions, second phases). Separation of intrinsic and extrinsic MW losses using standard MW measurements is very difficult. The most promising approach to this problem is the study of higher frequency dielectric response including the whole THz and IR range [55] and its temperature dependence down to low temperatures.

2.1 Theory of intrinsic losses

The intrinsic MW losses are fully determined by the lattice absorption of the ideal (but necessarily anharmonic) crystal lattice. The simplest model which describes the

strong lattice absorption due to polar phonon modes within the broad IR and far-IR range is that of the additive damped harmonic oscillators. Neglecting the anisotropy, the corresponding dielectric function (complex permittivity) can be written as

$$\epsilon^*(\omega) = \epsilon_\infty + \sum_{j=1}^{n} \frac{S_j}{\Omega_j^2 - \omega^2 + i\omega\gamma_j} \tag{2.1}$$

where ϵ_∞ is the optical permittivity defined by the electronic polarization mechanisms, $S_j = e_j^2/(\epsilon_0 v m_j)$ is oscillator strength (e_j effective charge, v unit cell volume, m_j reduced mass), $\Omega_j = (f_j/m_j)^{1/2}$ is the eigenfrequency (f_j force constant) and and γ_j is damping of the jth polar phonon mode. Summation goes over all n polar modes allowed by the lattice symmetry. In fact, Equation 2.1 is three-parameter oscillator model described by Equation 1.28 where oscillator strength $S_j = \Delta\epsilon_j\Omega_j^2$ is introduced. It is preferred from the point of view of physical analysis, because S_j is related to ionic charges in the lattice and it is an internal factor characterizing a particular material.

The simplest idea of estimation of the intrinsic MW losses consists in extrapolation of Equation 2.1 down to MW range, i.e. 2-3 orders of magnitude below phonon eigenfrequencies ($\omega \ll \Omega_j$). Then for real permittivity and losses we obtain

$$\epsilon'(\omega) \simeq \epsilon(0) = \epsilon_\infty + \sum_{j=1}^{n} \frac{S_j}{\Omega_j^2} \tag{2.2}$$

$$\epsilon''(\omega) \simeq \omega \sum_{j=1}^{n} \frac{S_j\gamma_j}{\Omega_j^4} \tag{2.3}$$

Simple interrelation between $\epsilon(0)$ and ϵ'' can be obtained if we reduce our discussion to the strongest polar mode and drop the summation in Equation 2.3:

$$\epsilon''/\omega = [\epsilon(0) - \epsilon_\infty]^2\gamma/S \tag{2.4}$$

We see that the losses are proportional to the frequency and to the damping and that they are roughly quadratically increasing with the static permittivity. However, in the frame of the described phenomenological model, one cannot say how the permittivity change affects γ and S values and to what extent the Equation 2.1 is valid in the low-frequency submillimeter and MW range if frequency independence of γ and S is assumed. Experiments performed on the ordered cubic complex perovskite system $Ba(B'_{1/2}B''_{1/2})O_3$ (B′ = Y^{3+}, In^{3+}, Nd^{3+}, Gd^{3+}, Mg^{2+}, Cd^{2+} and B″= Ta^{5+}, Nb^{5+}, W^{6+}) [56] have shown that the losses increase with permittivity much faster than quadratically. This fact demonstrates that the simplified approach of classical damped oscillators is not always sufficient for explanation of MW losses.

The most complete microscopic theory of low-frequency losses in dielectrics was worked out and reviewed by Gurevich and Tagantsev [57]. It considers all possible loss mechanisms in terms of photon absorption in dielectric crystal due to the multi-quantum processes. Figure 2.1 schematically shows the main absorption processes considered by the theory. The strongest process (number 1 in Figure 2.1) is related to resonance absorption of photon with creation of phonon with the same energy and wave vector. It is responsible for the absorption in the vicinity of polar optical phonon eigenfrequencies at the Brillouin zone center $\Omega_{TOj}(0)$. In the limit of MW

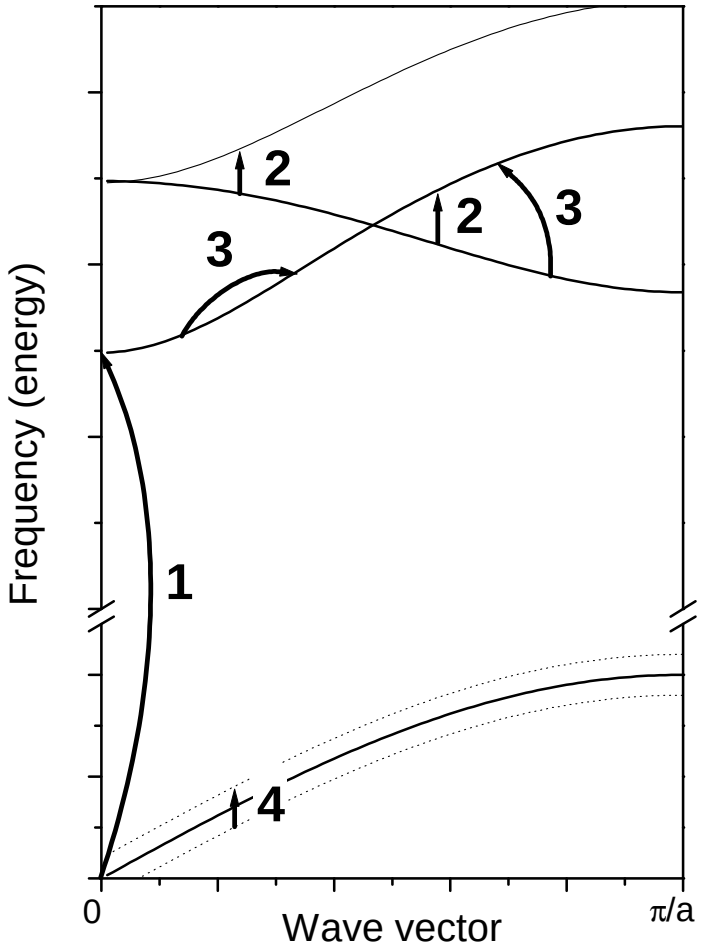

Figure 2.1: Possible photon absorption mechanisms in dielectric crystal: (1) - resonance single-phonon loss; (2) - three-quantum loss; (3) - four-quantum loss; (4) - quasi-Debye loss

frequencies $\omega \ll \Omega_{TOj}$ the characteristic energy of the phonons primarily responsible for the loss is much larger than the energy of the field quanta with which they are interacting. This large difference makes it difficult to satisfy the conservation laws in processes involving the absorption of photons. There are three other main lattice loss mechanisms contributing in MW absorption (see Figure 2.1): three-quantum loss, four-quantum loss and quasi-Debye loss.

The three-quantum mechanism corresponds to photon absorption processes involving two phonons, satisfying energy and quasi-momentum (wave vector) conservation laws of the form

$$\Omega_j(\mathbf{k}) \pm \Omega_{j_1}(\mathbf{k_1}) = \omega, \qquad \mathbf{k} \pm \mathbf{k_1} = 0 \tag{2.5}$$

Minus sign here stands for two-phonon difference absorption process denoted as number 2 in Figure 2.1. It occurs near the lines of degeneracy of the phonon branches in the Brillouin zone. Optical phonon from the thermally populated branch absorbs photon creating phonon with higher energy and the same wave vector on the adjacent phonon branch. Plus sign in Equation 2.5 corresponds to the summation process when the quantum of electromagnetic field generates two phonons with opposite wave vectors. In MW frequency region this process can take place only for low-energy part of acoustic branches where phonon density of states is small. Therefore summation process does not play appreciable role in MW losses.

For the dominant two-phonon difference mechanism, it was shown that two frequency regimes should be distinguished, a higher-frequency one $\Omega_i \gg \omega \gg \gamma_T$ and a lower-frequency one $\omega \leq \gamma_T$, where γ_T is the averaged damping of thermally populated phonons. If the former inequality can be satisfied, it was shown that in the case considered $\epsilon''(\omega) \propto \omega^2 T$ whereas in the MW range one expects $\epsilon''(\omega) \propto \omega T^2$ (neglecting weak logarithmic correction in T) [57, 58].

Four-quantum loss mechanism is represented by processes involving three phonons with conservation laws

$$\Omega_j(\mathbf{k}) \pm \Omega_{j_1}(\mathbf{k_1}) \pm \Omega_{j_2}(\mathbf{k_2}) = \omega, \qquad \mathbf{k} \pm \mathbf{k_1} \pm \mathbf{k_2} = \mathbf{b} \tag{2.6}$$

where $\mathbf{b}$ is a reciprocal lattice vector. Despite of the small probability of such process comparing to three-quantum loss its contribution is comparable to the latter one due to the weak restrictions of transitions between phonon branches imposed by the conservation laws (2.6). The wave vector of additional phonon participating in four-quantum process makes possible not only vertical transitions between the branches but also transitions within a particular branch (see process number 3 in Figure 2.1). Thus, unlike the case of three-quantum loss, four-quantum loss involves contributions coming from not only from the vicinity of degeneracy lines but from the whole Brillouin zone.

Another mechanism of intrinsic losses which is characteristic for non-centrosymmetric (piezoelectric) crystals was pointed out by Coombs and Cowley [59]. Formally it occurs due to the perturbation of the phonon distribution function induced by an applied ac field. This can be qualitatively interpreted as transitions within a single phonon branch because of its finite width γ_T. This contribution should dominate in the broad range around γ_T above the Debye temperature. It is called quasi-Debye

losses because of its frequency dependence which is equivalent to a simple Debye relaxator peaked at frequency γ_T [57]

$$\epsilon''(\omega) \propto \frac{T\gamma_T\omega}{\omega^2+\gamma_T^2} \tag{2.7}$$

Quasi-Debye mechanism contribution is proportional to the temperature because it needs a thermally generated phonon to absorb the photon of electromagnetic field. Therefore the main contribution to this process comes from the thermally populated acoustic branches (number 4 in see Figure 2.1) or from the lowest optical branch.

In centrosymmetric (pseudo-cubic) crystals the quasi-Debye losses are forbidden by symmetry and MW losses are mainly determined by two-phonon difference transitions in the vicinity of C_4-lines of degeneracy between the two transverse optic branches. It can be shown that in this case losses obey the following expression [58]

$$\epsilon'' \simeq \frac{\mu}{6v^2\epsilon_\infty^3}\ln\left(\frac{\Omega_{LO}}{2\gamma_T}\right)\frac{\gamma_T}{\Omega_{LO}^2}\omega\epsilon^5(0) \tag{2.8}$$

which predicts much steeper dependence of losses on permittivity than quadratic given by Equation 2.4. It helps to understand the behavior of $Ba(B'_{1/2}B''_{1/2})O_3$ MW ceramics in which $\epsilon'' \propto \epsilon^4(0)$ dependence has been observed [56].

Comparison of classical oscillator model of dielectric losses with rigorous phonon kinetic theory reveals that the classical model in the case of weak anharmonic cubic system yields essentially higher losses than predicted by rigorous approach. However, in the case of materials with higher permittivity, steep dependence on $\epsilon(0)$ (Equation 2.8) leads to much higher losses which might be comparable to those given by Equation 2.4. Thus often simplified classical oscillator model can be successfully used for extrapolation of losses in MW materials [60, 40].

2.2 Extrinsic losses

As it was already mentioned the extrinsic losses arise due to the presence of lattice defects. The defect-induced loss mechanisms can be roughly classified into four groups.

(i). Static disorder induced one-phonon absorption. It is caused by relaxation of the wave vector conservation rule due to break down of the translational symmetry. This process is temperature independent if the concentration of defects does not depend on temperature. The losses are roughly proportional to one-phonon density of states. For MW range ($\omega \ll \Omega_j$) losses are determined by activation of the linear part of acoustic branches. Microscopic calculations yield [57] $\epsilon'' \propto \omega$ for uncorrelated charged point defects [61] and uncharged planar defects, $\epsilon'' \propto \omega^2$ for uncharged linear defects and $\epsilon'' \propto \omega^3$ for uncharged point defects. In the case of correlated charged point defects where the charge neutrality is realized in the correlation volume, MW losses obey $\epsilon'' \propto \omega^3$ up to the frequency $\omega_c \simeq \bar{v}/\xi$ where $\bar{v}$ is the mean transverse acoustic velocity and ξ the correlation length [61]. Estimation of typical values gives $\xi \simeq 10 \div 100$ Å and $\omega_c \simeq 10^{10} \div 10^{12}$ Hz.

(ii). Phonon scattering on defects. It reduces the phonon lifetime and increases the damping. The main effect on the loss spectrum concerns the enhanced damping of polar phonon modes and increase in γ_T (see Equations 2.4 and 2.8).

(iii). Absorption associated with localized defect vibrations. Usually it contributes to losses in submillimeter and infrared range, but the inversion symmetry breaking around the defect can give rise to a quasi-Debye type contribution which increases MW loss as well.

(iv). Losses directly connected with anharmonic motion of charged defects. At high temperatures this mechanism gives rise to broad relaxation-like loss maxima with thermally activated relaxation times. At low temperatures quantum tunneling of the defects in disordered systems might become important.

Note that first two groups of loss mechanisms can result in linear frequency dependence of extrinsic losses similarly to intrinsic losses. Therefore the known frequency dependence of the loss factor is not always sufficient to estimate contribution of the extrinsic losses. However the mentioned loss mechanisms are direct, i.e. do not involve thermally populated phonons, and their contributions are temperature independent. At the same time, intrinsic loss contribution vanishes at low temperatures. Thus the measurements of temperature dependence of losses allows to separate intrinsic and extrinsic loss factors. This procedure has been applied to the analysis of submillimeter losses in $Ba(B'_{1/2}B''_{1/2})O_3$ compounds [56, 62].

Regardless of the mechanism of extrinsic losses, its contribution is small comparing to intrinsic losses in high-frequency THz and far IR region ($\Omega_i \gg \omega \gg \gamma_T$). Therefore THz spectroscopy of MW materials combined with FTIR spectroscopy in a broad temperature range is able to provide good estimation of intrinsic losses or directly reveal the presence of additional loss contribution.

2.3 Experimental results

Our experimental task was to study THz dielectric response of different MW ceramics and compare it with the data obtained by FTIR spectroscopy and MW measurements in order to estimate intrinsic and extrinsic losses. Another aim was to find out how the chemical composition and the parameters of technological processing affect the quality of investigated materials.

In far IR spectroscopy commonly measured characteristics of materials are complex permittivity ($\epsilon' - i\epsilon''$) or refractive index ($n - i\kappa$) at different temperatures. On the other hand, MW characterization usually involves values of the permittivity ϵ', the quality factor $Q = \epsilon'/\epsilon''$ (or $Q \times f$, which should be frequency independent if $\epsilon'' \propto f$) and of the temperature coefficient of resonance frequency τ_f defined as

$$\tau_f = \frac{1}{f_r}\frac{df_r}{dT} \tag{2.9}$$

where f_r is the eigenfrequency of a dielectric resonator made of investigated material. Temperature coefficients of the permittivity τ_ϵ and of the refractive index τ_n can be introduced in the similar way. They are related to each other by the simple relations [63]

$$\begin{aligned} \tau_f &= -\alpha - \tau_n, \\ \tau_n &= \tau_\epsilon/2, \end{aligned} \tag{2.10}$$

where α is the linear coefficient of thermal expansion.

2.3.1 $Ba(Mg_{1/3}Ta_{2/3})O_3$ ceramics

Complex perovskite $Ba(Mg_{1/3}Ta_{2/3})O_3$ (BMT) ceramics, which contain Mg- and Ta-ions arranged in an ordered fashion, possess the highest Q-factor ($Q \simeq 35000$ at 10 GHz) among the known microwave dielectric materials [64]. These materials are also characterized by a low temperature coefficient ($\tau_f = 5$ ppm/℃) and relatively large permittivity ($\epsilon' \simeq 25$). The MW properties of BMT were first investigated by Nomura *et al.* [65]. They reported that BMT is difficult to sinter and suggest doping with Mn which greatly improves sinterability. The far IR dielectric response of BMT ceramics have been studied so far by means of infrared and microwave spectroscopy [66, 55]. Recently IR reflectivity study of BMT samples with different sintering time has been made by Shimada [67]. It was found that MW losses depend on technology of preparation [64, 68, 69, 70]. In particular, two-step mixed oxide process produces ceramics with higher quality factor than conventional single-step oxide process [64]. The sintering temperature also influence quality of ceramics. It was demonstrated that there exists an optimal sintering temperature which provides highest MW quality factor for given preparation technology of $Ba(Mg_{1/3}Ta_{2/3})O_3$ ceramics [71]. Microwave dielectric properties of BMT materials can be appreciably improved by Zr-doping in two-step mixed oxide process or lead to degradation of the quality factor in the case of single-step process [70]. The $Ba_5Ta_4O_{15}$ which can appear as a secondary-phase incorporated into BMT perovskite was found to significantly decrease the density and MW quality of the BMT materials [68]. X-ray diffraction study reported by Youn *et al.* [72] revealed presence of several secondary Ba-Ta-O phases in initial perovskite structure of BMT ceramics. Besides already mentioned $Ba_5Ta_4O_{15}$, also $Ba_3TaO_{5.5}$, $Ba_4Ta_2O_9$, $Ba_7Ta_6O_{17}$ and $BaTa_2O_6$ phases has been detected.

TDTTS was used for preliminary investigation of sub-mm response of BMT ceramics by Tsai *et al.* [73] and later on by Lin *et al.* [74]. Recently it has been also applied to the (x)$Ba(Mg_{1/3}Ta_{2/3})O_3$-(1-x)$Ba(Mg_{1/3}Nb_{2/3})O_3$ complex perovskite system [75].

The aim of our study was to investigate THz and far IR dielectric response of different BMT ceramics produced using various preparation technologies. The samples were provided by I-Nan Lin (Materials Science Center of Tsing-Hua University, Taiwan). The studied samples were divided into three groups according to the technology of preparation. First group consisted of samples prepared by two-step calcination mixed oxide technology. Chemically pure $BaCO_3$, MgO and Ta_2O_5 powders were used as starting materials. The process consists of two stages: (i) the $MgTa_2O_6$ powders were prepared by mixed-oxide process, viz. calcining $MgO : Ta_2O_5 = 1 : 1$ mixture at 1200℃ during 2 hours; (ii) the $BaCO_3$ and $MgTa_2O_6$ powders were mixed together with $BaCO_3 : MgTa_2O_6 = 3 : 1$ molar ratio, followed by calcining at 1150-1250℃ to form pure perovskite $Ba(Mg_{1/3}Ta_{2/3})O_3$ powders.

The second group of samples was prepared by alkoxide process which is believed to improve the mixing homogeneity and increase the activity of the calcined powders [76]. In this process, the metallic-Ba, metallic-Mg and $Ta(OC_2H_5)_5$ were dissolved separately into 2-methoxyle-enthanol (2-MOE) at 125℃ and then mixed to form $Ba^{2+} - Mg^{5+} - Ta^{5+}$ alkoxide precursors in 3:1:2 molar ratio. Thus obtained precursors were than sprayed into ketone aqueous solution (H_2O:ketone = 1:15) at room temperature. The $Ba^{2+} - Mg^{5+} - Ta^{5+}$ containing powders were then vacuum dried and calcined at 1000-1150℃ for 4 hours to convert the amorphous mixture into crystalline BMT phase.

Table 2.1: List of investigated BMT ceramics

Preparation technology	ϵ'	$Q \times f$ (THz)			Reference
		TDTTS	IR	MW	
mixed oxide	26.7	70-80	220	556	[55], [76]
Zr-doped	25.6	75-90	-	35-40	[70]
alkoxide	25.6	≈ 20	-	608	[76]

The third group was prepared by the two-step mixed oxide technology as the first group. In addition, $BaZrO_3$ was added into the mixture in the ratio of 2 mol % and then calcined at 1200℃ for 4 hours. Thus pure perovskite phase of Zr-doped $Ba(Mg_{1/3}Ta_{2/3})O_3$ has been obtained.

BMT phases produced by all mentioned methods were then pelletized and sintered at 1450-1600℃ for 4 hours. The densities of the sintered pellets were about 97% of theoretical density for pellets prepared by mixed oxide method and about 92% for alkoxide pellets. The samples intended for TDTTS were prepared in the form of plane-parallel pellets with the diameter of 6 mm and the thickness of 0.2-0.25 mm. For FTIR reflectivity measurements more than 2 mm thick samples with optically polished front side have been used. The measured far-IR reflectivities of all BMT samples are very similar and the origin of small deviations between them is more likely related to the optical quality of the surface than to the technological reasons. Typical spectra of samples from each group (sintering temperature 1500℃ for alkoxide and mixed oxide and 1550℃ for Zr-doped ceramics) together with the fits are shown in Figure 2.2. According to [66], ordered $Ba(Mg_{1/3}Ta_{2/3})O_3$ perovskite lattice has trigonal structure (space group $P\bar{3}m1$) with three formula units ($Z = 3$) per unit cell. The fitting procedure was performed using factorized four-parameter oscillator model (Equation 1.29) by 16 oscillator predicted by factor group analysis [77]. The example of complex permittivity obtained from the fitting is shown in Figure 2.3 for Zr-doped BMT sample. It can be seen that there are eight modes which give main contribution to the permittivity (two of them are located above 400 cm^{-1} and are not seen in Figure 2.3). The remaining eight modes are very weak and only slightly improve the quality of reflectivity fits. We did not find any essential difference between mode frequencies of all measured samples. However there is some difference between damping constants of the strongest IR modes which determine the difference in MW absorption. The complex permittivities of the best quality BMT samples from each group measured by TDTTS are shown in Figure 2.4. The continuous increase of the permittivity with frequency is due to a phonon resonance at 138 cm^{-1} (see Figure 2.3). The permittivities of the samples are close to each other, the fit gives static permittivity of 25.6 for Zr-doped and alkoxide samples and 26.7 for mixed oxide sample. They are in good agreement with MW permittivity values ($\epsilon_{MW} \simeq 24 - 25$) [64]. For alkoxide BMT samples we observe an additional resonances around 30 and 45 cm^{-1} [39]. Since the other samples do not present this kind of resonances we conclude that the enhanced losses in alkoxide BMT ceramics are related to the traces of a secondary non-perovskite phase. However this second phase is probably not usually detected $Ba_5Ta_4O_{15}$ satellite of BMT perovskite phase because TDTTS does not reveal any modes below the lowest IR-mode around 70 cm^{-1} in pure $Ba_5Ta_4O_{15}$ [60]. Another candidates can be $Ba_7Ta_6O_{17}$ or other secondary Ba-Ta-O phases observed in BMT

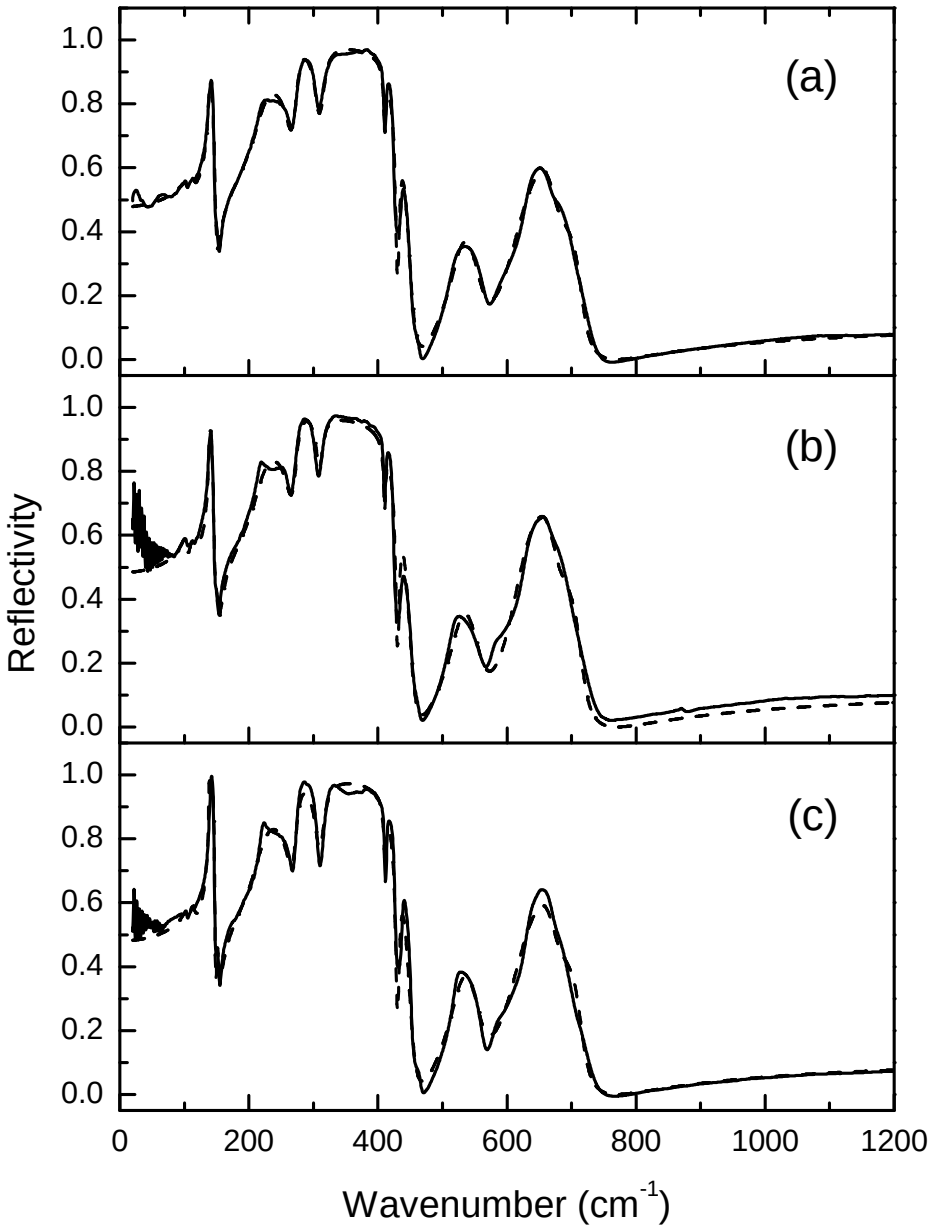

Figure 2.2: IR reflectivity spectra of chosen BMT samples. Solid and dash lines correspond to experimental and the fitted curves. BMT samples are Zr-doped mixed oxide (a), undoped mixed oxide (b) and alkoxide (c).

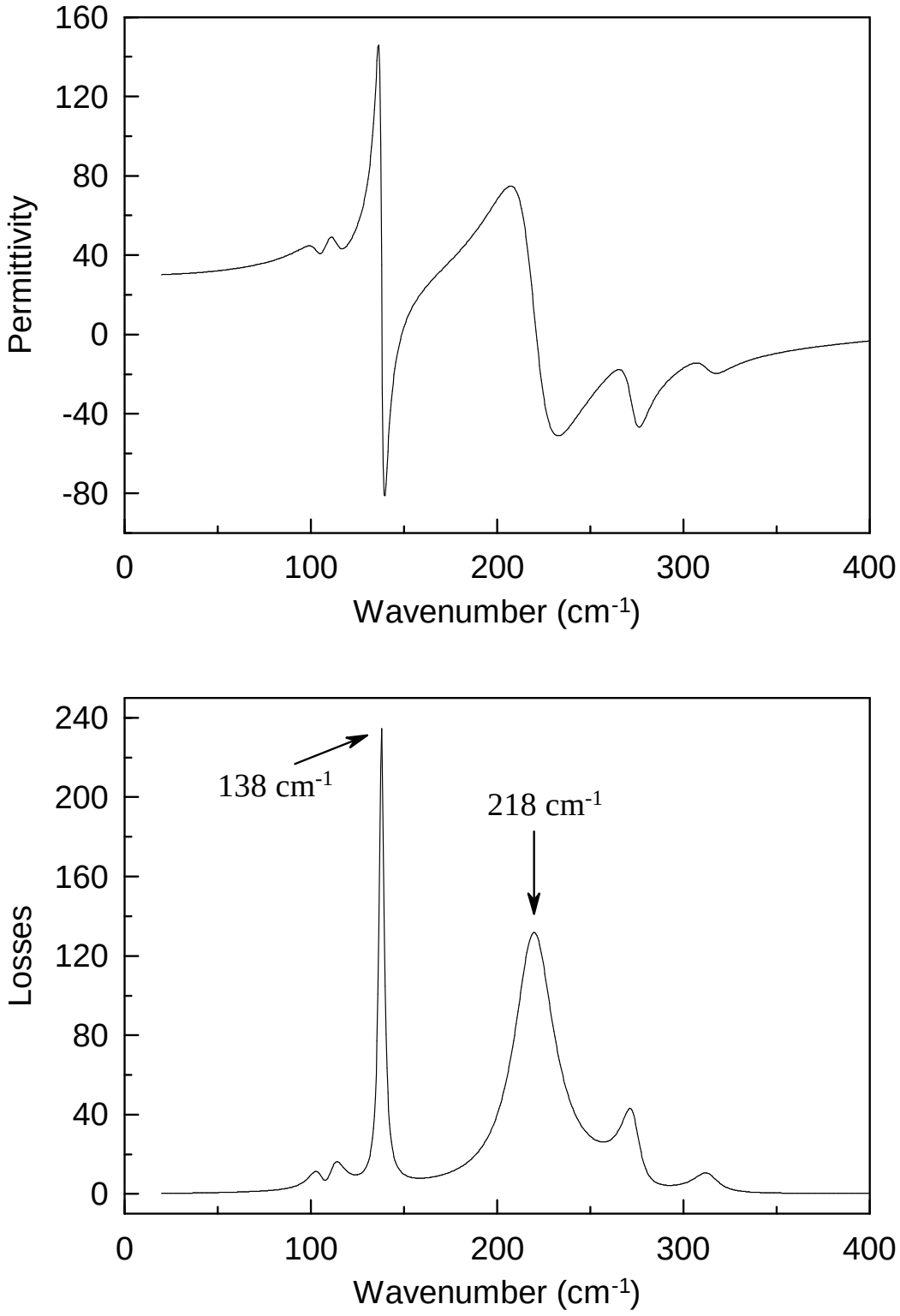

Figure 2.3: Permittivity and losses of Zr-doped mixed oxide BMT sample obtained from the fit

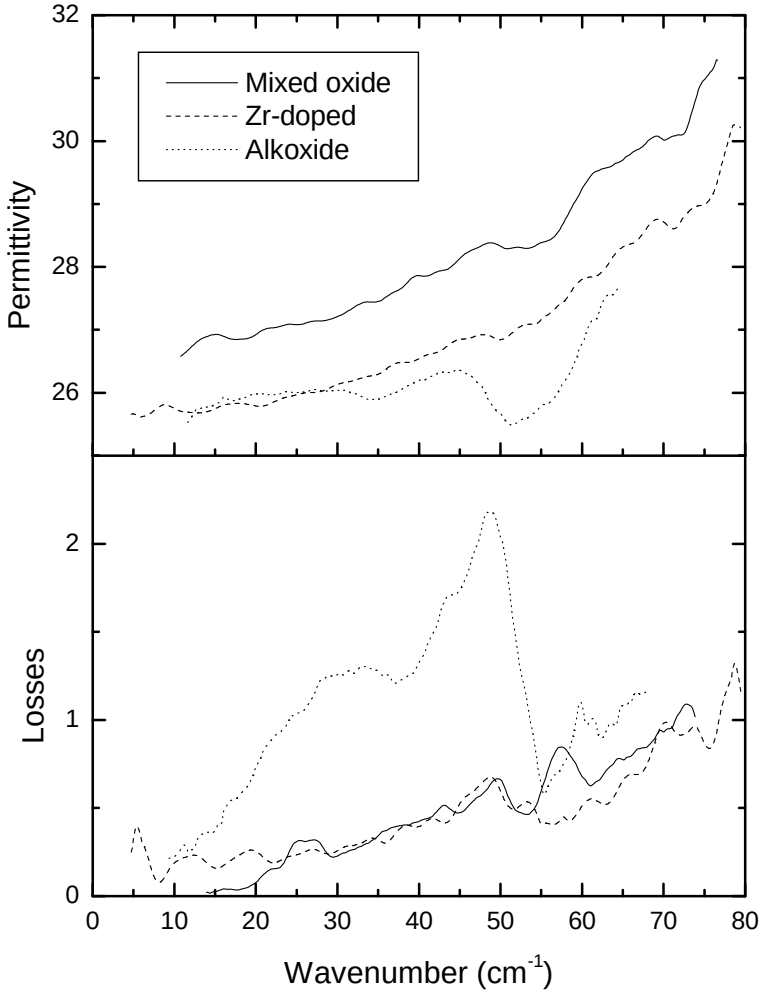

Figure 2.4: Permittivity and losses of BMT samples obtained by TDTTS.

ceramics [72] containing heavy groups of atoms with low eigenfrequencies. The results of our sub-mm measurements of BMT ceramics are summarized in Table 2.1 where permittivities and quality factors determined by TDTTS are compared with the published IR and MW data. The comparison shows a large scattering (about an order of magnitude) of quality factors published in literature and determined in the present study. It rises the question of reliability of loss values obtained by different measuring techniques and the validity of the linear extrapolation of THz losses down to MW region. In particular, the quality factors published in [76] seem to be overestimated by an order of magnitude.

Our TDTTS and FTIR spectroscopic study of BMT ceramics leads to following conclusions: (i) Zr-doping during two-step mixed oxide process increases quality factor of BMT ceramics in THz range in agreement with the results of MW measurements [70]; (ii) BMT ceramics prepared by alkoxide process are characterized by additional resonances in THz range due to the presence of secondary phase of unknown structure and have appreciably higher intrinsic losses than BMT ceramics prepared by mixed oxide technology. The latter result is in contradiction to MW measurements [76] probably due to the overestimation of MW quality factor or failure of a simple classical oscillator model in the case of additional resonances in sub-mm range.

2.3.2 $CaTiO_3$-based complex ceramic systems

$CaTiO_3$ (CT) is a good candidate for a microwave dielectric since it has a high permittivity of 160, quality factor $Q = 8000$ at 1.5 GHz but unfortunately it has a large positive temperature coefficient of resonant frequency ($\tau_f = +850$ ppm/℃) [78]. In order to produce a MW material with τ_f close to zero, one may form a solid solution combining $CaTiO_3$ with a material exhibiting a negative τ_f. We have studied four complex ceramic systems in which $CaTiO_3$ is mixed in different ratios with MW perovskites: $Sr(Mg_{1/3}Nb_{2/3})O_3$ (SMN), $Sr(Zn_{1/3}Nb_{2/3})O_3$ (SZN), $LaGaO_3$ (LG) and $NdAlO_3$ (NA). The samples were provided by "Materials Research Institute, Sheffield University, UK". They were synthesized by a conventional mixed oxide route using $CaCO_3$, TiO_2, Nd_2O_3, Al_2O_3, La_2O_3, Ga_2O_3, $SrCO_3$, MgO, ZnO and Nb_2O_5 high purity powders. The weighted starting regents were mixed in appropriate ratios and milled. The powders were calcined for 4-6 hours at temperatures between 1300 ℃ and 1550 ℃, depending on composition. Calcined powders were re-milled, pressed into discs and sintered for 4-6 hours at the temperatures between 1500 ℃ and 1650 ℃. The samples for TDTTS were prepared in the form of plane-parallel pellets with the diameter of 6 mm and the thickness of approximately 0.2 mm. For FTIR reflectivity measurements more than 2 mm thick samples with optically polished front side have been used.

$CaTiO_3$-$Sr(Mg_{1/3}Nb_{2/3})O_3$ and $CaTiO_3$-$Sr(Zn_{1/3}Nb_{2/3})O_3$ ceramics

$Sr(Mg_{1/3}Nb_{2/3})O_3$ is a material with small negative temperature coefficient ($\tau_f = -14$ ppm/℃), permittivity $\epsilon = 33$ and $Q = 20000$ at 3 GHz [78]. It is one of the candidates to compensate the positive temperature coefficient of $CaTiO_3$ in solid solution systems. Structural investigation of SMN revealed 1:2 stoichiometric B-site cations ordering in trigonal complex perovskite structure (space group $P\bar{3}m1$) [79]. However, in (1-x)$CaTiO_3$– x$Sr(Mg_{1/3}Nb_{2/3})O_3$ this kind of ordering is maintained for $x > 0.9$ only [80]. Additional evidence for B-site ordering was given by observation of two Raman peaks near 391 and 825 cm^{-1} in CT-SMN which are not present in pure $CaTiO_3$. First peak is related to the long-range order and vanishes for $x \leq 0.8$. Second peak at 825 cm^{-1} is present even for higher concentrations of $CaTiO_3$ and it becomes wider with decreasing x. It was suggested that it reflects the degree of short-range ordering (nonrandom B-site distribution) in CT-SMN [81]. The temperature coefficient of resonant frequency τ_f tunes through zero at $x \simeq 0.8$ with $\epsilon \simeq 45$. However the quality factor is rather poor for this composition $Q \times f = 11$ THz [80, 81]. Therefore it is very important to determine whether the fundamental (intrinsic) or extrinsic losses are responsible for decrease of quality factor in CT-SMN ceramics.

We have studied set of eight CT-SMN ceramics with different compositions (x = 0; 0.1; 0.25; 0.4; 0.5; 0.6; 0.8; 1). The obtained FTIR reflectivity and TDTTS spectra were fitted together using factorized oscillator model (Equation 1.29). In the case of ordered $A(B'_{1/3}B''_{2/3})O_3$ compounds ($Sr(Mg_{1/3}Nb_{2/3})O_3$ is a particular case), factor group analysis in the paraelectric phase ($P\bar{3}m1$, $Z = 3$) yields 16 IR-active modes [77]. Pure $CaTiO_3$ has 25 IR-active modes (only 14 of them are strong enough to be detected [82]). We have used 16 four-parameter oscillators for the fitting of pure SMN, 9 oscillators for $0.4 \leq x \leq 0.8$ where long-range ordering of B-sites does not exist and 11-13 oscillators for $x \leq 0.25$. The measured reflectivity of pure

$Sr(Mg_{1/3}Nb_{2/3})O_3$ ceramics agrees with the data published by Fukuda *et al.* [83]. However they used 20 oscillators for the fitting of reflectivity which is obviously redundant for $Sr(Mg_{1/3}Nb_{2/3})O_3$. The fitted permittivity and dielectric losses of chosen samples are shown in Figure 2.5 together with the directly measured submillimeter and MW data. It is seen that MW and submillimeter permittivity values are in a good agreement with the fitted curves. However, MW dielectric loss values are somewhat higher than intrinsic losses extrapolated by the fitting procedure. This difference is more pronounced for $x \geq 0.8$. In order to demonstrate this effect more clearly $Q \times f$ values measured in the MW range and those obtained from the fits are plotted as functions of CT-SMN composition (Figure 2.6). Quality factors tend to decrease when the concentration of SMN is decreasing. However this dependence is steeper in the case of intrinsic losses obtained from IR data. Thus for $x \leq 0.1$ the dielectric loss is fully determined by the fundamental intrinsic losses and for $x = 0.8$ the extrapolated quality factor is twice smaller than the measured one. Taking into account the comparison in Figure 2.6, we can conclude that the poor quality factor of CT-SMN ceramics with $\tau_f \approx 0$ ($x \approx 0.8$) is mostly a consequence of extrinsic losses which may be eliminated by reducing the defect density in the ceramics. On the other hand, MW dielectric losses are rather close to the fitted intrinsic losses for $x \leq 0.25$. It indicates a high quality of $CaTiO_3$ ceramics moderately doped with $Sr(Mg_{1/3}Nb_{2/3})O_3$.

Ordered $Sr(Zn_{1/3}Nb_{2/3})O_3$ has the same structure as $Sr(Mg_{1/3}Nb_{2/3})O_3$, its permittivity is a slightly higher $\epsilon \simeq 42.7$ and the quality factor ($Q = 3850$ at 3 GHz) is appreciably lower than that of $Sr(Mg_{1/3}Nb_{2/3})O_3$. Temperature coefficient of resonant frequency in pure $Sr(Zn_{1/3}Nb_{2/3})O_3$ $\tau_f = -26.8$ ppm/℃ [84]. Solid solutions (1-x)$CaTiO_3$-x$Sr(Zn_{1/3}Nb_{2/3})O_3$ has not been investigated in MW and far IR ranges until recently. Initial X-ray diffraction study revealed perovskite structure in the full range of concentrations. Therefore, despite of rather high dielectric losses in CT-SZN system, its investigation is interesting from the point of view of comparison with CT-SMN. The important point is that the temperature stable MW ceramics with higher permittivity ($\tau_f \simeq 0$ for $x = 0.87$) can be obtained.

We have studied set of seven CT-SZN ceramics with different compositions (x = 0; 0.2; 0.4; 0.5; 0.6; 0.8; 1). The number of IR modes used for the fitting of FTIR reflectivity and TDTTS complex permittivity data was varied from 8 (for x = 0.6) to 16 (for x = 1). The measured reflectivity and the parameters of the fitting model of pure $Sr(Zn_{1/3}Nb_{2/3})O_3$ agrees with previously published data [83]. The fitted permittivity and dielectric losses of several samples are shown in Figure 2.7 together with the directly measured submillimeter and MW data. The observed correspondence between the fitted and the directly measured permittivity values is rather good. MW dielectric losses are somewhat higher than the intrinsic losses predicted by the fits. However this difference is not so essential as in the case of CT-SMN system. Thus we can conclude that the low quality factor of CT-SZN ceramics are mostly related to the fundamental (intrinsic) loss mechanisms due to multiphonon absorption processes. In contrast to CT-SMN ceramics there is no technological way to achieve appreciably higher quality of investigated CT-SZN ceramics.

$CaTiO_3$-$LaGaO_3$ ceramics

Lanthanum gallate ($LaGaO_3$) has attracted much attention as a substrate for epitaxial growth of superconducting $YBa_2Cu_3O_{7-\delta}$ film. It was found that it can be good

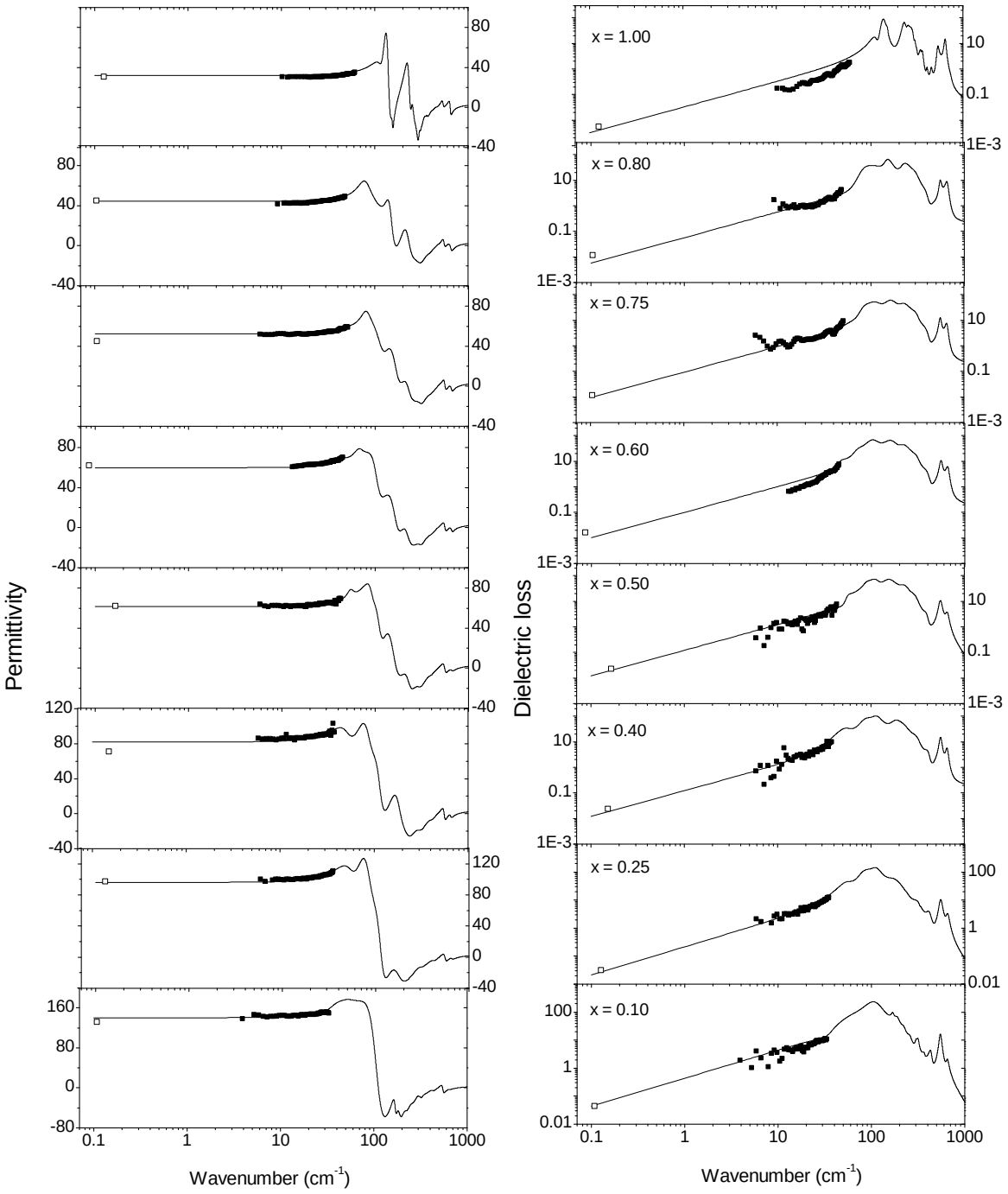

Figure 2.5: Permittivity and dielectric loss spectra of (1-x)$CaTiO_3$–x$Sr(Mg_{1/3}Nb_{2/3})O_3$ ceramics. Solid lines correspond to the fit, points are measured submillimeter and MW data.

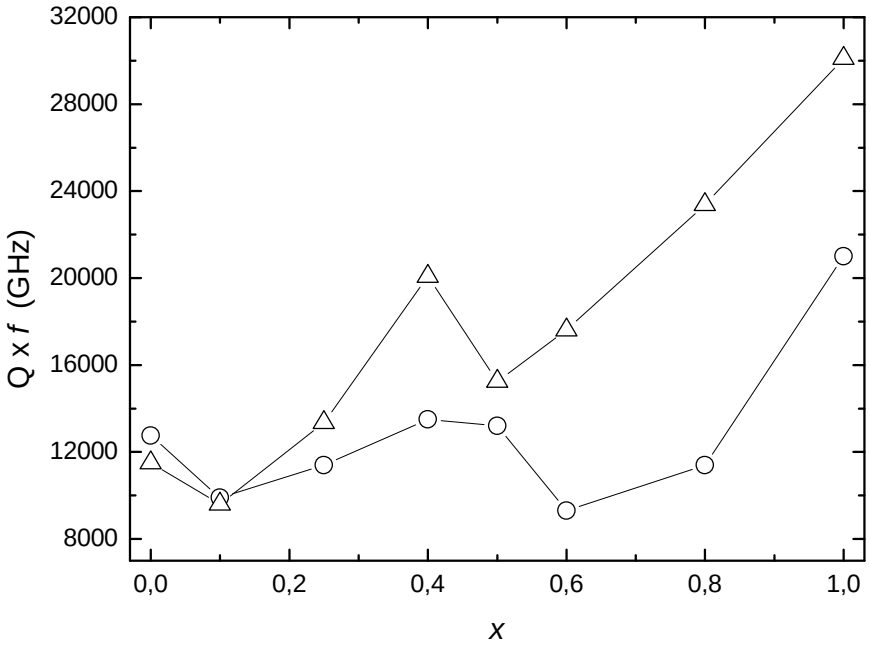

Figure 2.6: $Q \times f$ values of (1-x)$CaTiO_3$–x$Sr(Mg_{1/3}Nb_{2/3})O_3$ ceramics extrapolated from the fits of IR data (triangles) and directly measured at MW frequencies (circles).

alternative to $SrTiO_3$ because of better lattice match. Moreover $LaGaO_3$ possesses very low dielectric losses up to GHz frequency range having permittivity $\epsilon \simeq 25$ and it is promising material for microwave applications. Mixing $LaGaO_3$ with $CaTiO_3$ had been expected to improve permittivity and temperature stability of obtained compounds.

$LaGaO_3$ undergoes a phase transition at 145℃ in which it transforms from high-temperature rhombohedral phase to orthorhombic structure with *Pnma* space group [85, 86]. The factor group analysis predicts 24 Raman-active and 25 IR-active phonon modes for orthorhombic $LaGaO_3$ at room temperature. Raman spectroscopy of $LaGaO_3$ ceramics was reported in [87,88]. Fortunately, the dielectric and IR measurements were performed on single crystals that gives us a possibility to compare them with our results on ceramics. IR reflectivity has been measured and fitted by Calvani *et al.* [89] and later by Zhang *et al.* [90]. Dube *et al.* [91] reported low frequency (100 Hz – 1 MHz) and microwave dielectric properties of $LaGaO_3$ single crystals with (001) and (110) orientations.

We have studied set of nine (1-x)$CaTiO_3$-x$LaGaO_3$(CT-LG) ceramics with $x = l/8$ where $l = 0 \ldots 8$. The samples proved to be single phase by X-ray diffraction. The reflectivity spectra of the samples have been measured by FTIR spectroscopy and fitted by a four-parameter oscillator model. The number of oscillators required to obtain good fits vary from 9 to 12 depending on sample composition. Factor group analysis predicts 25 IR-active modes in $LaGaO_3$ [87] and the same number of modes in pure $CaTiO_3$ [82] though its space group *Pbnm* is different from *Pnma* group of $LaGaO_3$. The rest of predicted modes which have not been observed in experiment are probably very weak and their influence on dielectric permittivity and losses is negligible.

The fitted permittivity and dielectric losses of CT-LG samples are shown in Fig-

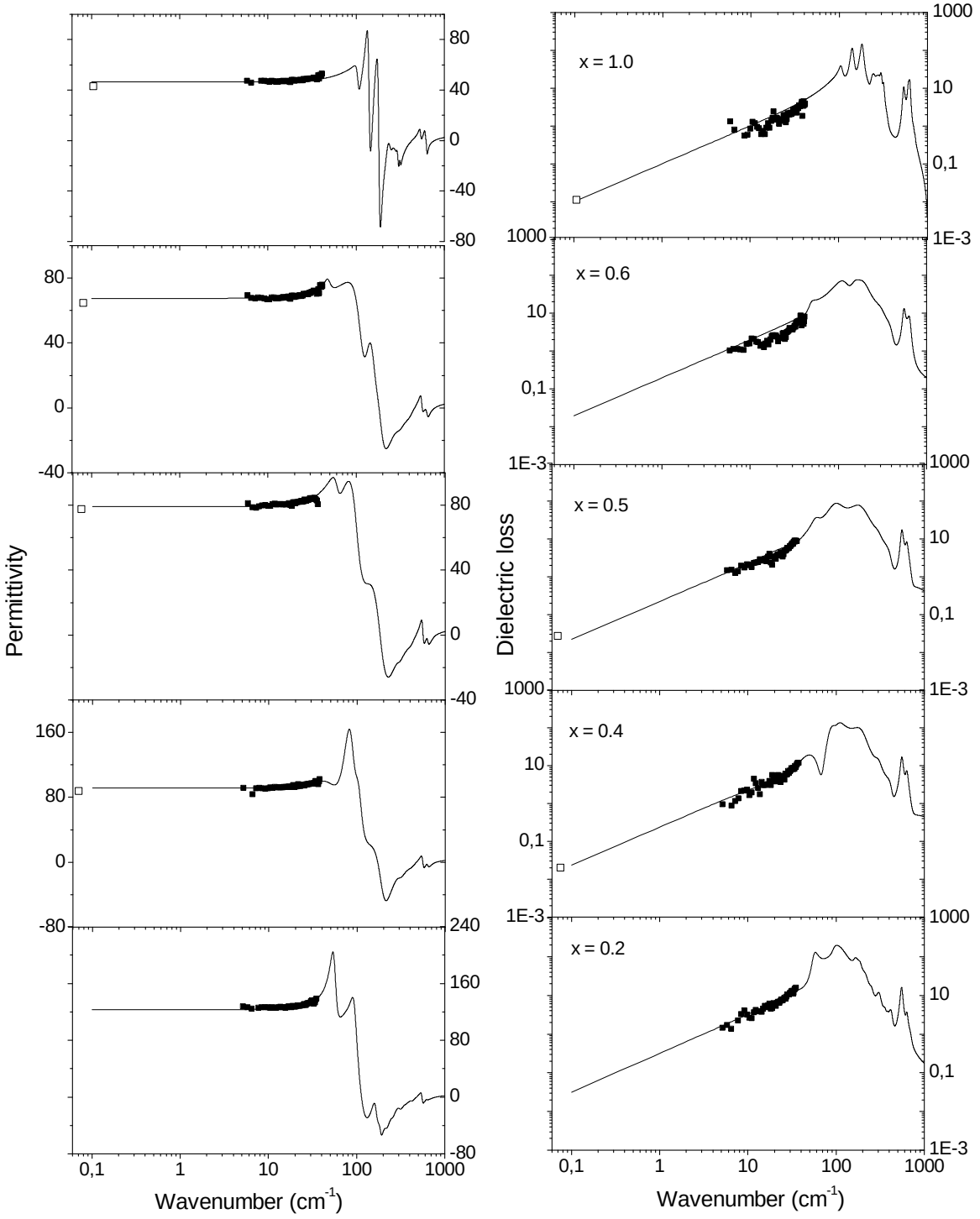

Figure 2.7: Permittivity and dielectric loss spectra of (1-x)$CaTiO_3$–x$Sr(Zn_{1/3}Nb_{2/3})O_3$ ceramics. Solid lines correspond to the fit, points are measured submillimeter and MW data.

ure 2.8 together with the directly measured submillimeter and MW data. The measured submillimeter permittivity and losses are in reasonable agreement with the oscillator fits. The MW dielectric losses are higher than the extrapolated intrinsic losses for $x = 1$ and $x < 0.375$ indicating presence of additional extrinsic losses for these compositions. Other CT-LG show only slight deviation from IR fits within the frames of fitting precision and can be considered as almost free from extrinsic losses.

We have tried to compare our results for pure $LaGaO_3$ ceramics to previous measurements performed on $LaGaO_3$ single crystals [90, 91]. For this purpose, we have simulated dielectric response of $LaGaO_3$ crystal at room temperature using the parameters of classical oscillator model determined by Zhang *et al.* [90]. The total number of oscillators was 10 and their parameters are in satisfactory agreement with our fits. The obtained permittivity values are in good agreement: $\epsilon(0) = 24.3$ from our fit, $\epsilon(0) = 22.6$ from the fit of Zhang *et al.* The product of MW quality factor and frequency obtained from the simulation is $Q \times f \simeq 83000$ GHz. The same quantity obtained using our fits is slightly higher $Q \times f \simeq 116000$ GHz. Such correspondence between extrapolated MW quality factors can be expected because they describe intrinsic losses which are related to phonon dynamics of material. This dynamics should not appreciably differ whether material is in form of single crystal or ceramics. Taking into account the results of the comparison, we can conclude that the defects in $LaGaO_3$ ceramics do not affect damping or dielectric strength of phonon modes in this material.

Let us now compare directly measured MW quality factors of $LaGaO_3$ single crystals and ceramics. Dube *et al.* [91] reported $Q = 10500$ at 7.9 GHz for (001)-oriented crystal. However, this values does not refer to the dielectric losses in [001] direction, because measurements were carried out by resonance method and the cylindrical electric field in the cavity does not define the response along a particular crystallographic direction. The measured quality factor of $LaGaO_3$ ceramics $Q \simeq 12600$ at 4.96 GHz. The corresponding products of the quality factor and measuring frequency are 83000 GHz for $LaGaO_3$ crystal and 62500 GHz for $LaGaO_3$ ceramics. One can note perfect correspondence between measured MW dielectric losses of the singe crystal and intrinsic losses extrapolated from far IR range. Thus the dielectric losses of $LaGaO_3$ single crystals are fully determined by the fundamental intrinsic losses as it could be expected. On the other hand, the dielectric losses of $LaGaO_3$ ceramics are higher than in single crystal by an amount of extrinsic loss contribution. For investigated $LaGaO_3$ ceramic sample (at 4.96 GHz) about 54% of losses are contributed by the intrinsic losses and 46% are due to the extrinsic losses.

In conclusion, comparison of dielectric losses for ceramic and crystalline forms of $LaGaO_3$ shows that the approach for estimation of intrinsic losses by extrapolation of oscillator model down to MW range gives reasonable results. Thus the verification of this approach demonstrated its validity typical MW material. The MW losses of CT-LG ceramics are mostly determined by intrinsic losses except pure $LaGaO_3$ and $x \leq 0.25$ where pronounced contribution of extrinsic losses is seen.

$CaTiO_3$-$NdAlO_3$ ceramics

$NdAlO_3$ is a rhombohedral perovskite with $\epsilon \simeq 22$, good quality factor ($Q \times f \simeq 58000$ GHz) and a negative temperature coefficient of resonant frequency ($\tau_f = -33$ ppm/℃) [92]. Depending on the chemical composition of the (1-x)$CaTiO_3$–x$NdAlO_3$ (CT-NA)

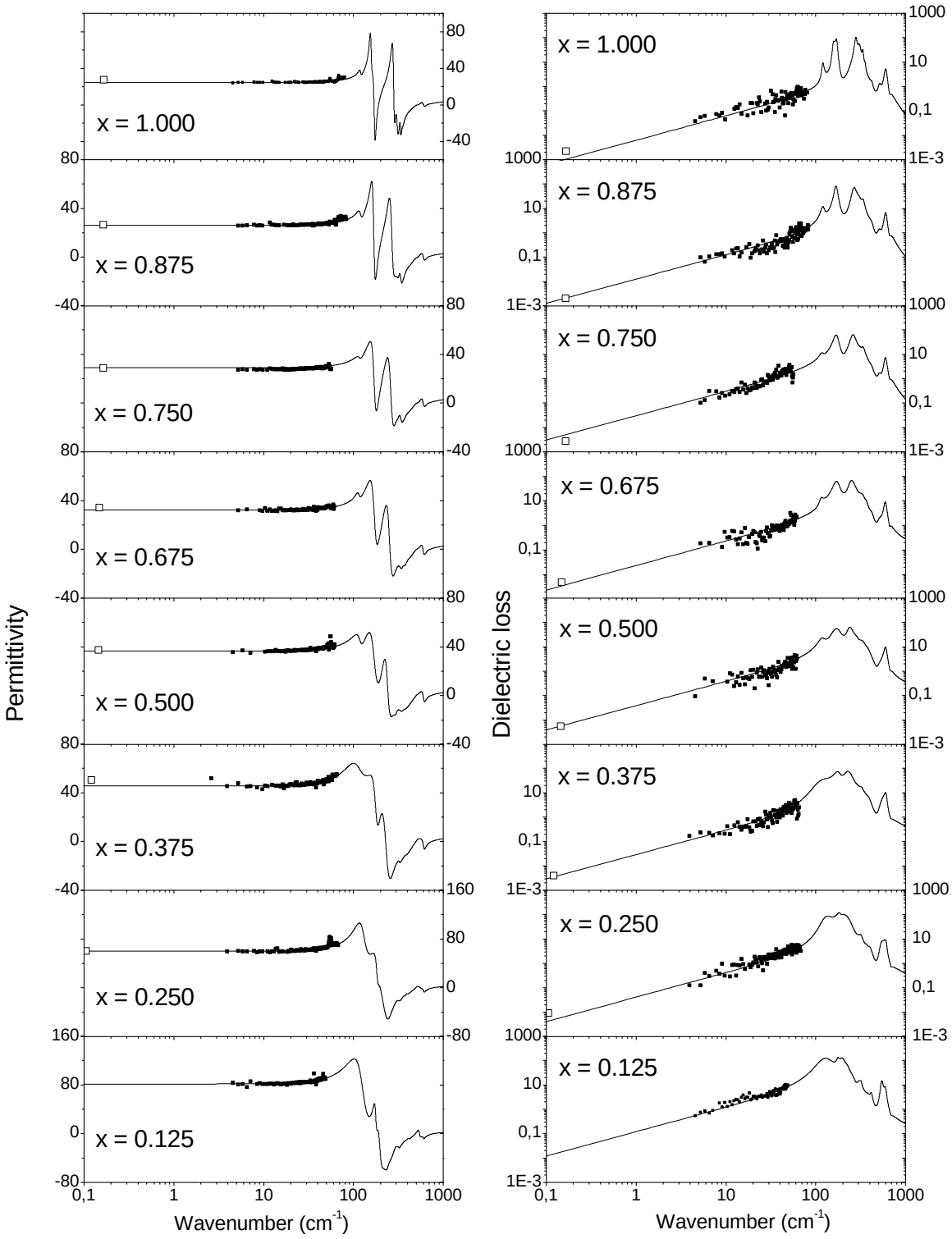

Figure 2.8: Permittivity and dielectric loss spectra of (1-x)$CaTiO_3$–x$LaGaO_3$ ceramics. Solid lines correspond to the fit, points are measured submillimeter and MW data.

solid solution, relative permittivities higher than 45 can be obtained with high quality factors ($Q \times f > 40000$ GHz) and a relatively small temperature coefficient τ_f. The value of τ_f close to zero is observed for $x \simeq 0.3$ [93]. Regarding the crystal structure, depending on composition the X-ray analysis shows the existence of at least two distinct regions. In the range $0 < x < 0.85$ the structure symmetry is orthorhombic similar to that of pure $CaTiO_3$ (space group $Pbnm$) and for $x > 0.90$ it is trigonal as in pure $NdAlO_3$ (space group $R\bar{3}c$) [94]. Microstructural characterization of CT-NA ceramics demonstrated that the heating conditions during sintering and subsequent cooling strongly affect the number of structural defects and correspondingly the dielectric losses ($Q \times f$ may vary from 30000 to 45000 GHz) [95, 94]. Raman scattering study of CT-NA revealed short-range ordering of B-site cations which appears as a broad Raman band around 800 cm^{-1}, this band is absent in both pure CT and NA and it has the strongest intensity for $x = 0.5$ [81].

We have studied set of nine CT-NA ceramics with $x = l/8$ where $l = 0 \ldots 8$. The reflectivity spectra of the samples measured by FTIR spectroscopy and their fits by a four-parameter oscillator model are shown in Figure 2.9. The number of oscillators required to obtain good fits vary from 11 to 13 depending on sample composition. Factor group analysis predicts 25 IR-active modes in pure $CaTiO_3$ (only 14 of them are strong enough to be detected [82]) and 8 IR-active modes for pure $NdAlO_3$ [87]. The correspondence between the number of predicted and observed IR-active modes is thus considered to be reasonable with exception of pure $NdAlO_3$ ($x = 1$) where the activation of additional 4 weak modes can be due to a partial relaxation of selection rules related to the existence of the symmetry-breaking defects in ceramic sample.

The permittivity and the dielectric loss obtained from the fit are shown in Figure 2.10 together with the values directly measured by microwave and TDTTS. It is seen that the permittivity values are in good agreement for all compositions. However, linear extrapolation of dielectric loss from THz to MW range by oscillator model gives overestimated losses for intermediate concentrations of $CaTiO_3$ ($0.375 \leq x < 0.75$). Moreover, the THz loss data are also slightly below the values predicted by the fits for this range of concentrations though the reflectivity curves are perfectly described by the fits (see Figure 2.9). Actually, oscillator model is exactly valid only close to phonon frequencies and it can fail at $\omega \ll \omega_{TO}$. Nonetheless our experience obtained on many ceramics shows that the extrapolation of oscillator model from THz range to MW range describes well intrinsic losses in many systems. CT-NA system seems to be exception from this rule in contrast to other investigated $CaTiO_3$-based microwave ceramics. Nevertheless, one can see that the measured submillimeter losses can be linearly extrapolated to the MW loss values (dotted lines in Figure 2.10). This fact agrees with the predictions of the microscopic theory of intrinsic losses [57] which should correctly describe the losses in CT-NA system.

Since the oscillator model fails in the case of CT-NA, the only conclusion we can make from comparison of submillimeter and MW losses is absence of appreciable extrinsic losses for $0.125 \leq x \leq 0.75$. The pure $NdAlO_3$ sample and CT-NA with x = 0.875 have extrinsic losses which are due to lower samples quality. Thus CT-NA ceramics with compositions close to the point of temperature stability ($x \approx 0.44$ according to our MW data) can be considered as promising materials for MW applications.

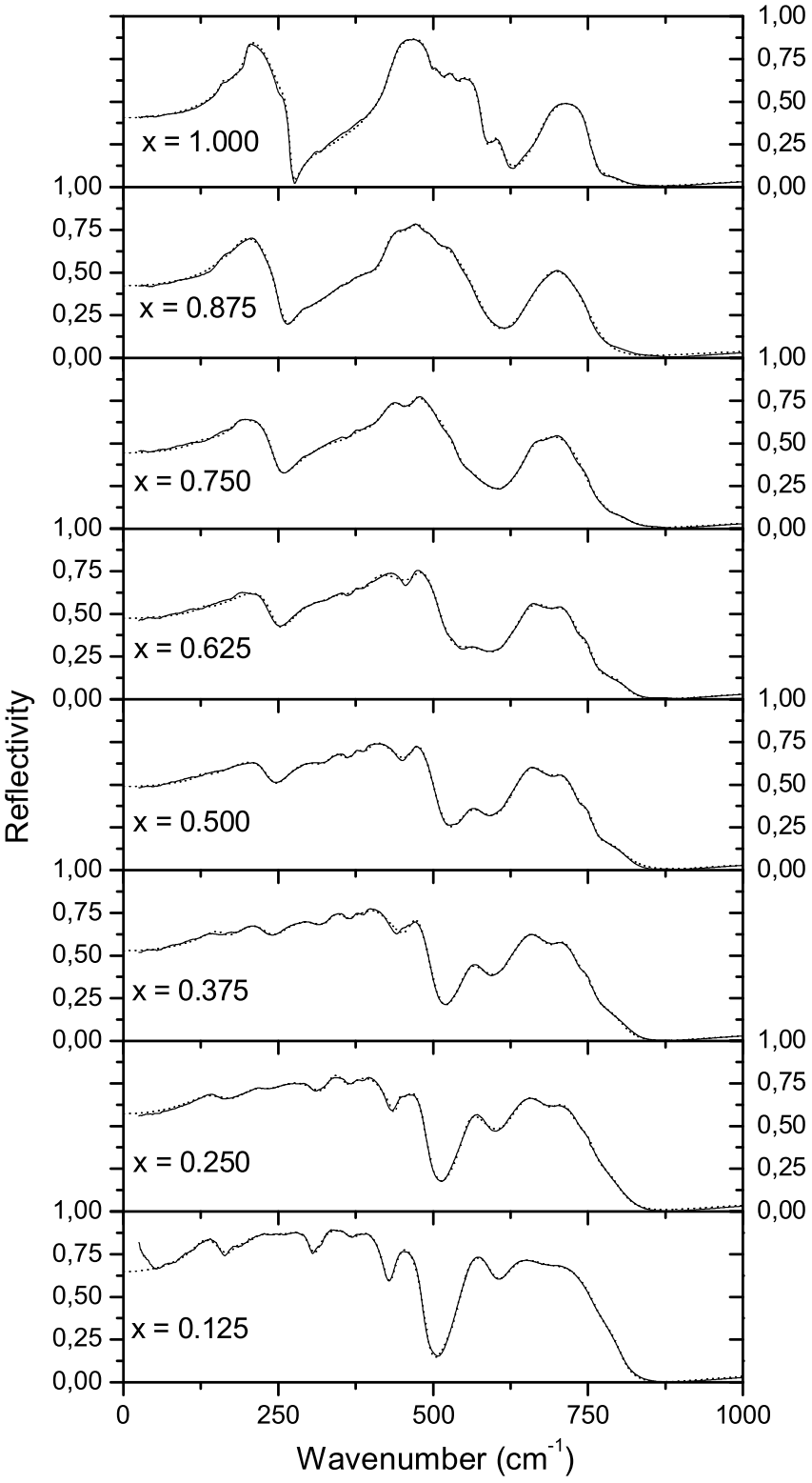

Figure 2.9: IR reflectivity spectra of (1-x)$CaTiO_3$– x$NdAlO_3$ ceramics. Solid and dash lines correspond to the experimental and fitted curves respectively.

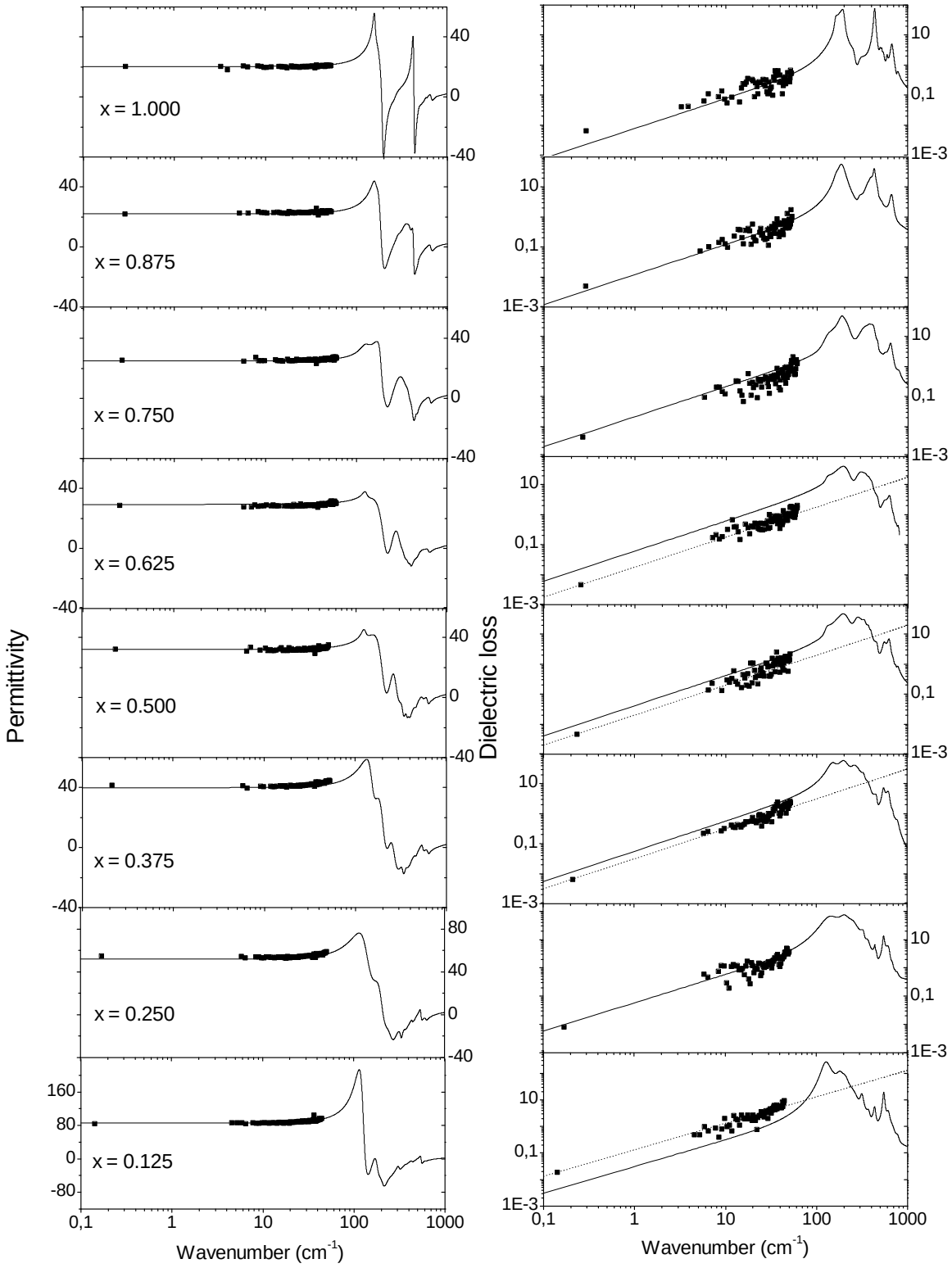

Figure 2.10: Permittivity and dielectric loss spectra of (1-x)$CaTiO_3$– x$NdAlO_3$ ceramics. Solid lines correspond to the reflectivity fits, points are measured submillimeter and MW data. Dotted line are linear fits of submillimeter and MW losses.

2.3.3 Doped CeO_2 ceramics

Cerium oxide (ceria, CeO_2) with a cubic fluorite structure (space group $Fm\bar{3}m$) is a very attractive dielectric material because of its chemical stability, relatively high dielectric constant ($\epsilon \simeq 23$) and close lattice match with silicon which very useful for its application in capacitors and buffer layers of superconducting materials [96]. It was shown that the doping with divalent and trivalent cations (e.g. Mg^{2+}, Ca^{2+} and Y^{3+}) has a dramatic effect on the sintering and grain growth behavior of CeO_2 ceramics [97]. Though considerable amount of papers devoted to the various aspects of ceria has been published, a very little attention has been paid to the MW dielectric properties of CeO_2 until recently. Kim *et al.* [98] reported MW dielectric measurements on $x$$TiO_2$–*(1-x)*$CeO_2$ ceramics system and demonstrated that it has excellent characteristics as a material for MW resonators. Combination of negative temperature coefficient of CeO_2 ($\tau_f = -104$ ppm/℃) and positive coefficient of TiO_2 ($\tau_f = 350$ ppm/℃) leads to a temperature-stable permittivity in the composition range $x = 0.2 \div 0.4$ [98].

Our investigation is devoted to the analysis of MW dielectric properties of pure and Ca- and Ti-doped CeO_2 ceramics. The samples were provided by M. T. Sebastian (Regional Research Laboratory, Trivandrum, India). The starting materials for preparation were CeO_2, TiO_2 and $CaCO_3$ high-purity powders. Cerium oxide was calcined at 800 ℃ for 3 hours and mixed in appropriate ratio with TiO_2 (0.43, 0.86, 2.15 and 2.15 mole%) or $CaCO_3$ (0.5–20 mole%). The obtained mixtures were well-grounded two times, dry-pressed into cylinders and heated to 1675 ℃ at the rate 10 ℃/min and soaked for 2 hours (sintering). Then they were cooled to 1000 ℃ at the rate of 5.5 ℃/min and cooled down to room temperature by natural cooling. The density of the obtained pure CeO_2 ceramics was of about 94 % of the theoretical density. The addition of a small amount of Ca^{2+} (< 2 mole%) and Ti^{4+} (< 2 mole%) increases the density of CeO_2 ceramics. However, further increase of dopants concentration decreases the density. The samples for far IR measurements were prepared in the form of plane-parallel disks with thicknesses in the range of 0.5–1.5 mm.

Infrared reflectivity spectra of pure and doped CeO_2 ceramics at room temperature are shown in Figure 2.11. The shape of the reflectivity curve of pure ceria corresponds to that observed for CeO_2 single crystals [99], however the absolute value of reflectivity is slightly lower for the ceramics. The reflectivity spectra were fitted together with the complex permittivity spectra obtained by TDTTS using three-parameter oscillator model (Equation 1.28). Although only one IR-active phonon mode of F_{1u} symmetry is allowed in the cubic $Fm\bar{3}m$ structure of CeO_2, two oscillators were needed for the fit of each reflectivity curve. The second one with the frequency near 400 cm^{-1} could be either a Raman F_{2g} mode (reported frequency: 465 cm^{-1} [100]) activated in IR due to the local breaking of inversion symmetry near lattice defects or it could have a multiphonon origin. It is by about two orders of magnitude weaker than the F_{1u} mode. The changes in the parameters of the main IR-active phonon mode F_{1u} in CeO_2 with Ti^{4+} and Ca^{2+} doping are presented in Table 2.2. With TiO_2 doping ω_0 decreases and $\Delta\epsilon_0$ increases; this explains the observed increase of MW permittivity in TiO_2-doped ceria. The opposite effect is observed in the case of $CaCO_3$ doping: ω_0 increases and $\Delta\epsilon_0$ decreases with increasing dopant concentration. These changes are also in agreement with MW results [101]. Samples highly doped with $CaCO_3$ ($\geq 10\%$) show a new heavily damped mode in the spectra near 130 cm^{-1} apparently related to the structural changes caused by high concentration of the dopant.

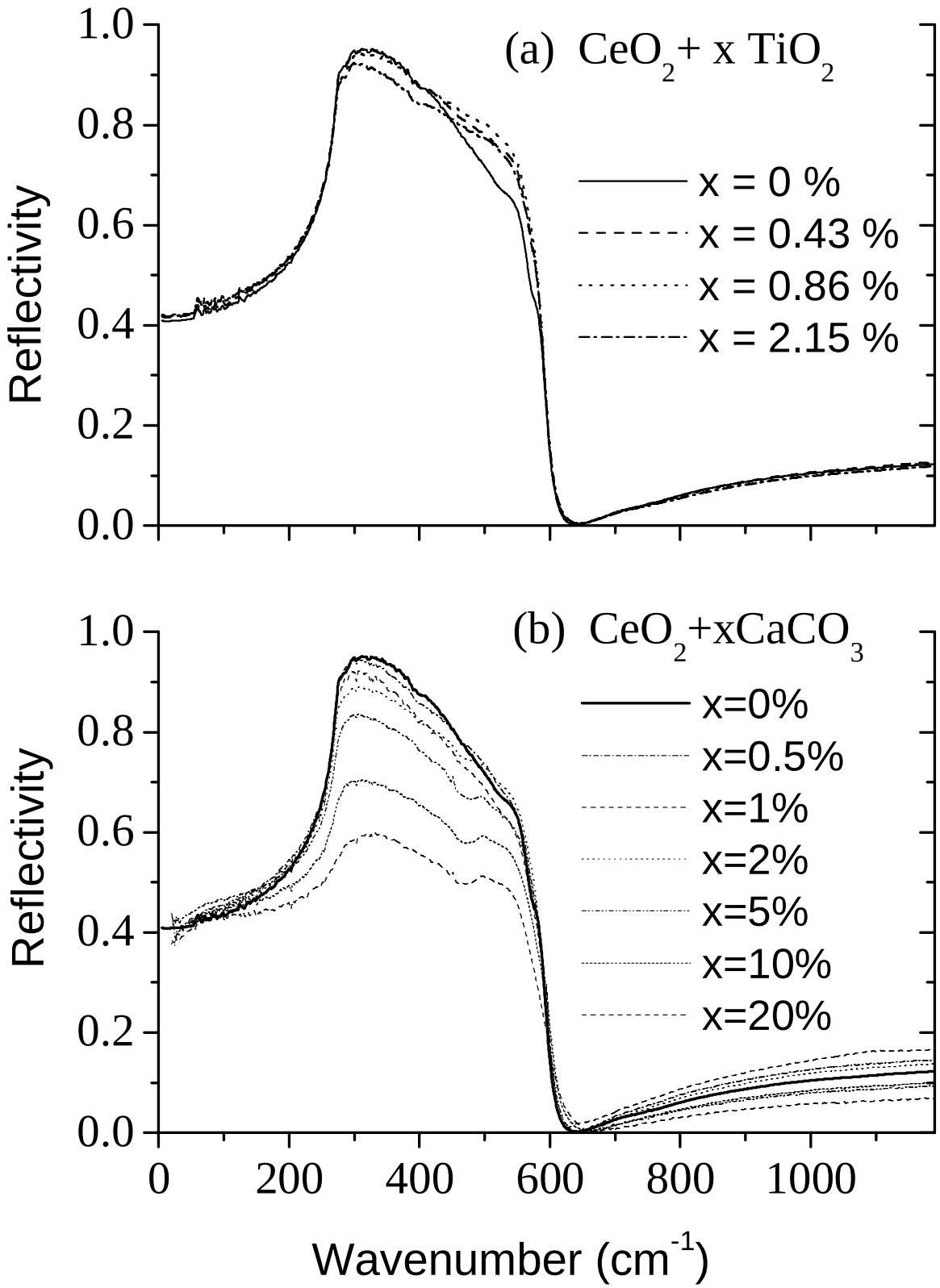

Figure 2.11: IR reflectivities of TiO_2 doped (a) and $CaCO_3$ doped (b) ceria.

Table 2.2: Parameters of F_{1u} phonon mode in doped CeO_2 ceramics at room temperature

Doping (mole %)	$\Delta\epsilon_0$	ω_0 (cm^{-1})	γ_0 (cm^{-1})
undoped	16.9	282.6	7.0
0.43 % TiO_2	18.2	278.7	12.3
0.86 % TiO_2	18.8	276.2	13.0
2.15 % TiO_2	18.7	273.2	13.4
0.5 % $CaCO_3$	16.9	279.8	8.2
1 % $CaCO_3$	15.5	283.2	7.8
2 % $CaCO_3$	17.0	280.6	19.2
5 % $CaCO_3$	17.3	269.4	37.4
10 % $CaCO_3$	12.9	290.6	64.1
20 % $CaCO_3$	9.8	290.6	64.1

Extrapolation of IR and submillimeter fits down to MW frequencies provides a good correspondence with the directly measured MW values of permittivity. However, the dielectric losses and quality factors show a significant difference. This is clearly demonstrated in Figure 2.12 where the values of $Q \times f$ measured at MW frequencies are plotted together with the results of the fits. For all investigated samples the measured quality factors are smaller than the quality factors related to the intrinsic loss only which are extrapolated from the fits of IR and submillimeter measurements. This fact indicates the presence of extrinsic loss in the studied ceramics. Comparing Figures 2.12a and 2.12b one can note that doping with TiO_2 decreases the quality of ceria much more than doping with $CaCO_3$. Furthermore, small concentrations of $CaCO_3$ (about 1 mol%) even increase the quality factor of the ceramic system. On the other hand, the intrinsic losses are comparable in both cases (in $CaCO_3$ doped sample they are slightly larger due to higher damping constants of the phonon modes).

In order to clarify the origin of high extrinsic losses in pure and doped ceria the low temperature measurements have been performed. Figure 2.13 shows temperature dependence of dielectric losses in pure CeO_2 ceramics obtained from the fits of IR reflectivity and THz complex permittivity in comparison with directly measured MW dielectric losses. It is clearly seen that the MW losses decrease faster on cooling than the extrapolated intrinsic losses. A more detailed view of the temperature behavior of dielectric losses in investigated samples at a particular MW frequency (5.58 GHz) is given in Figure 2.14. One can see a pronounced peak in the temperature dependence of dielectric loss in pure CeO_2 which gives evidence of the extrinsic loss caused by the temperature activated relaxation of defects in the ceramics sample. On the other hand, dielectric loss in Ca-doped ceria is lower than in pure CeO_2 and it is a monotonous function of temperature: the pronounced relaxation mechanism is absent here. However, irrespectively to relaxational losses, comparison of MW losses with the intrinsic loss values estimated from the IR and submillimeter measurements shows that both samples have appreciable extrinsic contribution to dielectric loss. This additional contribution varies with temperature approximately linearly (small intrinsic three-quantum loss depends quadratically on temperature above 100 K). Taking into account the fact that extrinsic losses caused by disorder induced one-phonon absorption or increased phonon scattering do not depend on temperature appreciably, one comes to the conclusion that the mechanism responsible for extrinsic loss is the quasi-

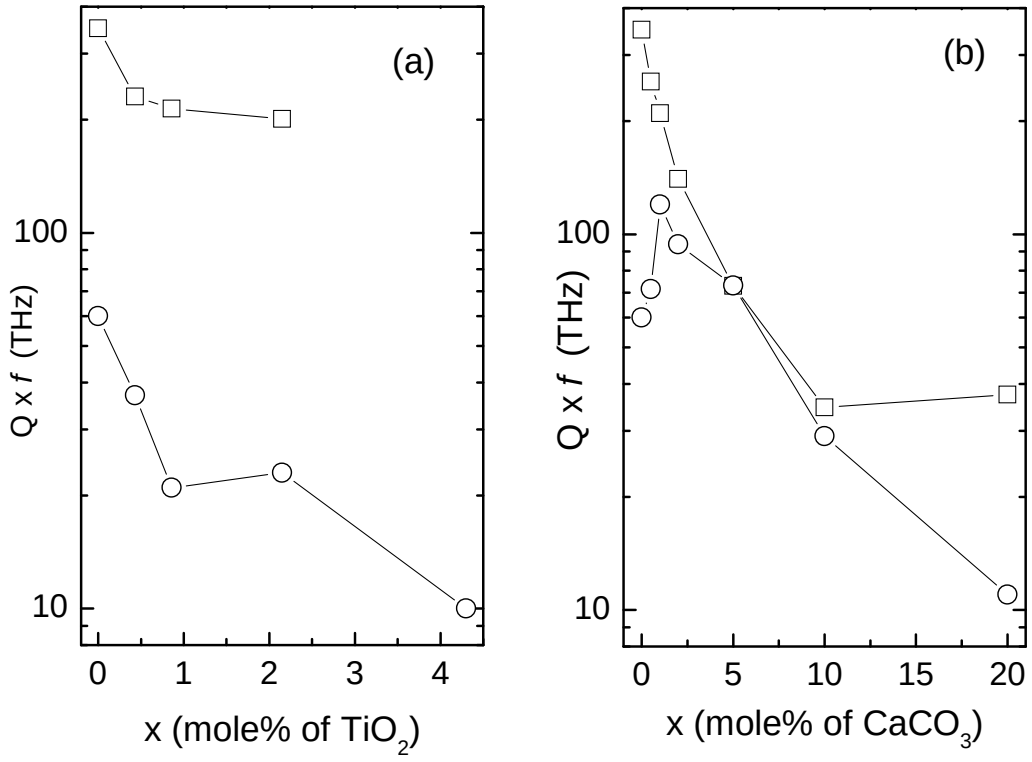

Figure 2.12: Microwave quality factors of TiO_2 doped (a) and $CaCO_3$ doped (b) ceria. Open circles are results of MW measurements, open squares are values extrapolated from the fits of IR and submillimeter data.

Debye type contribution (see Section 2.1, Equation 2.7). This kind of extrinsic loss is present in non-centrosymmetric lattices and can be activated in distorted grain boundaries of CeO_2 ceramics. This assumption also correlates with the activation of F_{2g} Raman mode in IR spectra due to the breaking of inversion symmetry. Similar kind of grain boundary activity was observed in $SrTiO_3$ ceramics [102].

In conclusion, our TDTTS, microwave and infrared spectroscopic study of Ca^{2+} and Ti^{4+} doped CeO_2 ceramics has revealed following features: (i) the quality factor and the dielectric constant are improved by the addition of 1 mol% $CaCO_3$, but they deteriorate as the Ca^{2+} content further increases, (ii) the addition of TiO_2 essentially decreases the quality factor, (iii) two sources of extrinsic losses (thermal relaxation and quasi-Debye loss) were found in pure ceria, however, the first loss mechanism (thermal relaxation of the defects) is suppressed by the doping with 1 mol% of $CaCO_3$ which indicates a possibility of improvement of the CeO_2 ceramics quality factor by Ca^{2+} doping.

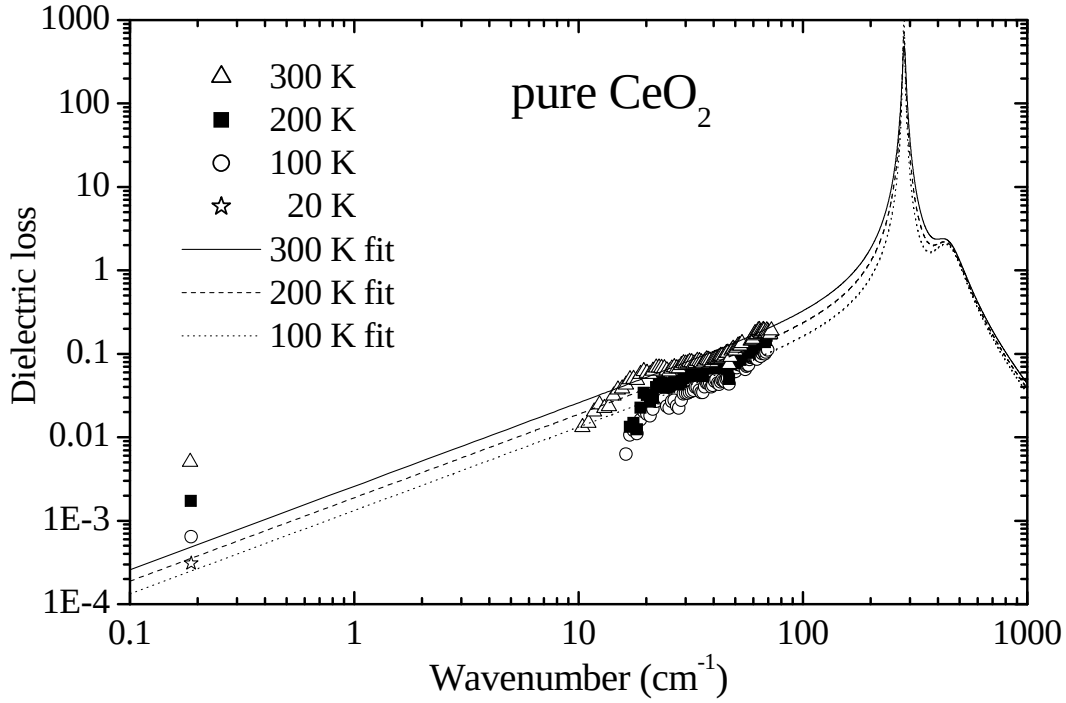

Figure 2.13: Temperature dependence of MW and submillimeter dielectric losses in pure CeO_2 compared with the fit of IR reflectivity.

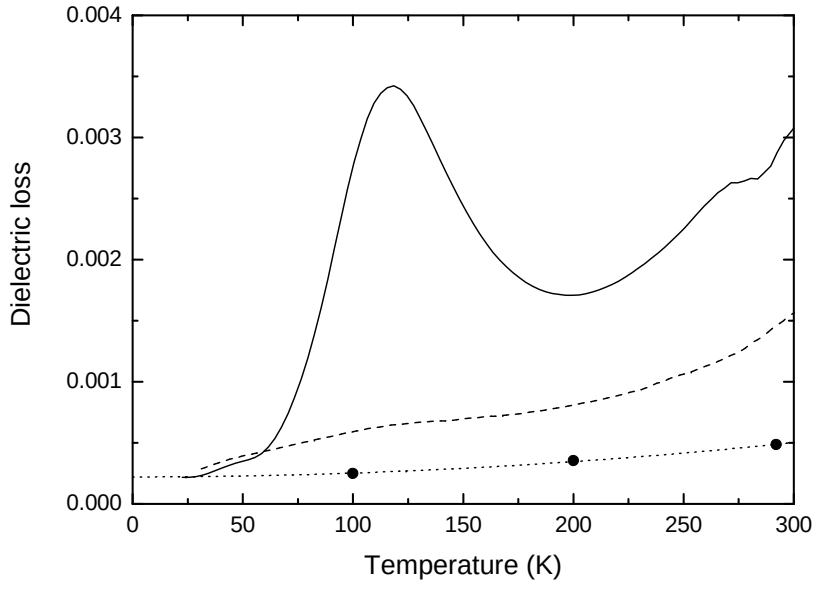

Figure 2.14: Temperature dependence of MW dielectric losses of pure CeO_2 (solid line) and 1 mol% Ca-doped CeO_2 compared with intrinsic losses of pure CeO_2 extrapolated from IR and submillimeter measurements (full circles). Dotted line is the fit of intrinsic losses with $(a + bT^2)$ law. Measuring frequency - 5.58 GHz.

Part 3

Perovskite oxides with relaxor properties

3.1 Introduction

Among the great variety of ferroelectric materials the ABO_3 perovskite oxides constitute an important class of ferroelectrics. Their relatively simple chemical and crystallographic structures stimulated extensive investigation of their properties. The typical member of ABO_3 family is $BaTiO_3$ which was the first discovered (in 1944) perovskite ferroelectric [103]. Its structure in paraelectric phase (cubic space group $Pm\bar{3}m$) and the temperature dependence of the permittivity taken from Ref. [104] are shown in Figure 3.1. Below ferroelectric phase transition at 120 ℃, $BaTiO_3$ lattice transforms to tetragonal symmetry with non-zero spontaneous polarization. On further cooling there are two other phase transitions at 0 ℃ and -70 ℃ characterized by a change of the direction of spontaneous polarization. The temperature dependence of the permittivity has a sharp peak at the transition point near 120 ℃ and above the transition it can be described by the Curie-Weiss law

$$\epsilon(T) = \epsilon_r + \frac{C}{T - T_c}, \tag{3.1}$$

where T_c is the critical temperature, C is the Curie-Weiss constant and ϵ_r is the temperature independent part of permittivity.

It was found that the structural change during phase transitions of displacive type is related to the slowing down of a single phonon mode frequency - such a mode is called *soft mode* [105]. In the case of ferroelectric phase transition this mode is IR-active, i.e. it possesses non-zero dipole moment which freezes below the transition temperature and gives raise to the spontaneous polarization. The sketch of the cubic perovskite unit cell distortion corresponding to the ferroelectric soft-mode is depicted in Figure 3.2. If we assume the other phonon modes to be temperature independent in the vicinity of the transition, the relation between the soft mode frequency and the static permittivity can be obtained using the factorized model of dielectric response (Equation 1.29). It is written here as a simplified form of Lyddane-Sachs-Teller (LST) relation [106]

$$\epsilon(T) = \frac{A}{\omega^2_{TO_1}(T)} \tag{3.2}$$

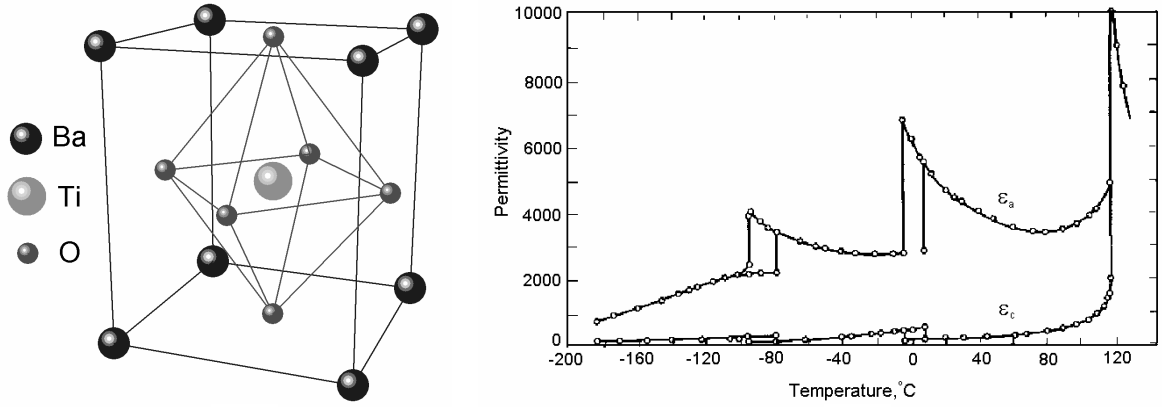

Figure 3.1: Cubic perovskite structure of $BaTiO_3$ (a) and its temperature dependence of permittivity along polar c-axis and non-polar a-axis (b).

where $\omega_{TO_1}(T)$ is the soft mode frequency and A is a proportionality constant. It is easy to see from Equation 3.2 that the permittivity divergence according to the Curie-Weiss law is connected to the vanishing of the soft mode frequency: $\omega_{TO_1} \propto \sqrt{T - T_c}$. This behavior of the soft mode is known as the Cochran law [107].

Besides ordinary perovskite ferroelectrics with phase transition occurring at relatively high temperatures, like $BaTiO_3$, $PbTiO_3$ and $KNbO_3$ where quantum effects can be neglected, there is a group of incipient ferroelectrics with perovskite structure in which the ferroelectric phase transition does not occur down to 0 K. The most extensively studied compounds of this family are $SrTiO_3$, $KTaO_3$ and $CaTiO_3$. Permittivity of these materials obeys Curie-Weiss law at high temperatures but saturates at low temperatures. The simplest expression that describes this behavior was found by Barrett [111] who extended the classical Slater's theory of ferroelectricity in perovskites [112] by treating the ionic polarizability quantum mechanically instead of classically

$$\epsilon(T) = \epsilon_r + \frac{C}{\frac{1}{2}T_1 \coth(\frac{T_1}{2T}) - T_0}. \tag{3.3}$$

Here $T_1 = h\nu/k$ is a characteristic temperature (ν is eigenfrequency of a quantum oscillator) and T_0 is the generalized Curie-Weiss temperature. For $T \gg T_1$, Equation 3.3 asymptotically approaches the Curie-Weiss law. On the other hand, for $T \to 0$, the permittivity saturates near the value $\epsilon_r + C/(0.5T_1 - T_0)$. The parameters of the Barrett formula for the main incipient ferroelectrics are summarized in Table 3.1. The

Table 3.1: Room-temperature ϵ(RT) and low-temperature ϵ_{max} values of permittivity and parameters of the Barrett law (Equation 3.3) for the incipient ferroelectrics.

Material	ϵ(RT)	ϵ_{max}	ϵ_r	C, 10^4 K	T_0, K	T_1, K	Reference
$SrTiO_3$	305	$\simeq 20000$		8	35.5	80	[108]
$KTaO_3$	239	3840	47.5	5.45	13.1	56.9	[109]
$CaTiO_3$	168	331	43.9	4.77	-111	110	[110]

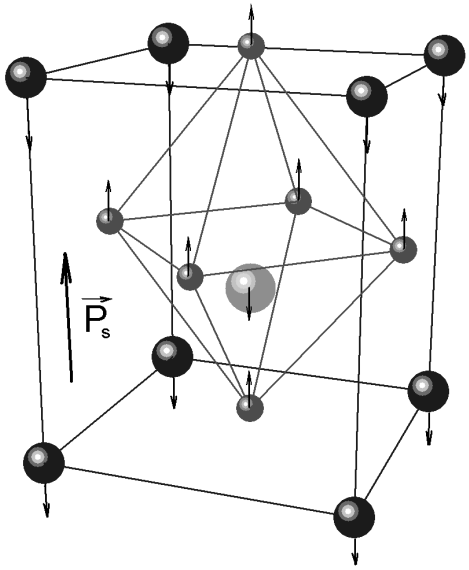

Figure 3.2: Ion motion for the ferroelectric soft mode in a simple perovskite.

Curie-Weiss temperature T_0 for $SrTiO_3$ and $KTaO_3$ is positive, however, the phase transition is suppressed in these materials due to the quantum fluctuations (zero-point motion). Therefore sometimes they are referred as quantum paraelectrics. On the other hand, for $CaTiO_3$ T_0 has formally a negative value from the viewpoint of Equation 3.3. The ferroelectric phase transition does not occur in $CaTiO_3$ at any temperature because the soft mode force constants remain positive maintain down to 0 K maintaining the stability of nonferroelectric state [113]. Quantum effects do not play a decisive role in this case. Nevertheless, the Barrett law can be used for the fitting of $CaTiO_3$ permittivity as a convenient empirical expression.

3.1.1 Complex perovskite relaxors

Another class of ferroelectric materials is formed by complex compounds, often having perovskite structure, which are characterized by a broad frequency dependent maximum in the temperature dependence of permittivity (Figure 3.3). This behavior is related to strong dielectric relaxations observed in these materials. Therefore the common name for this class of ferroelectrics is "relaxors" or "relaxor ferroelectrics" [114]. The relaxor ferroelectrics comprise a large number of stoichiometric complex perovskites with the chemical formula $A(B'_xB''_{1-x})O_3$, for example $Pb(Mg_{1/3}Nb_{2/3})O_3$ (PMN), $Pb(Sc_{1/2}Ta_{1/2})O_3$ (PST) and $Pb(Sc_{1/2}Nb_{1/2})O_3$ (PSN), and some perovskite solid solutions: $(Pb_{1-3x/2}La_x)(Zr_{1-y}Ti_y)O_3$ (PLZT $x/y/(1-y)$) and $(Pb_{1-x}Ba_x)(Zr_{1-y}Ti_y)O_3$ (PBZT). Compared to conventional ferroelectrics they are distinguished by a broad peak in the real part of the dielectric permittivity as a function of temperature. The magnitude of this peak decreases and its position shifts to higher temperature with increasing measurement frequency (from Hz to GHz). The imaginary part of the permittivity exhibits a similar shifts of the peak position, while its magnitude shows an increase with increasing measurement frequency (Figure 3.3).

It was found that relaxor behavior occurs if a static or dynamical disorder exists in the lattice. In particular, it was shown that PST ceramics with B-site ordering

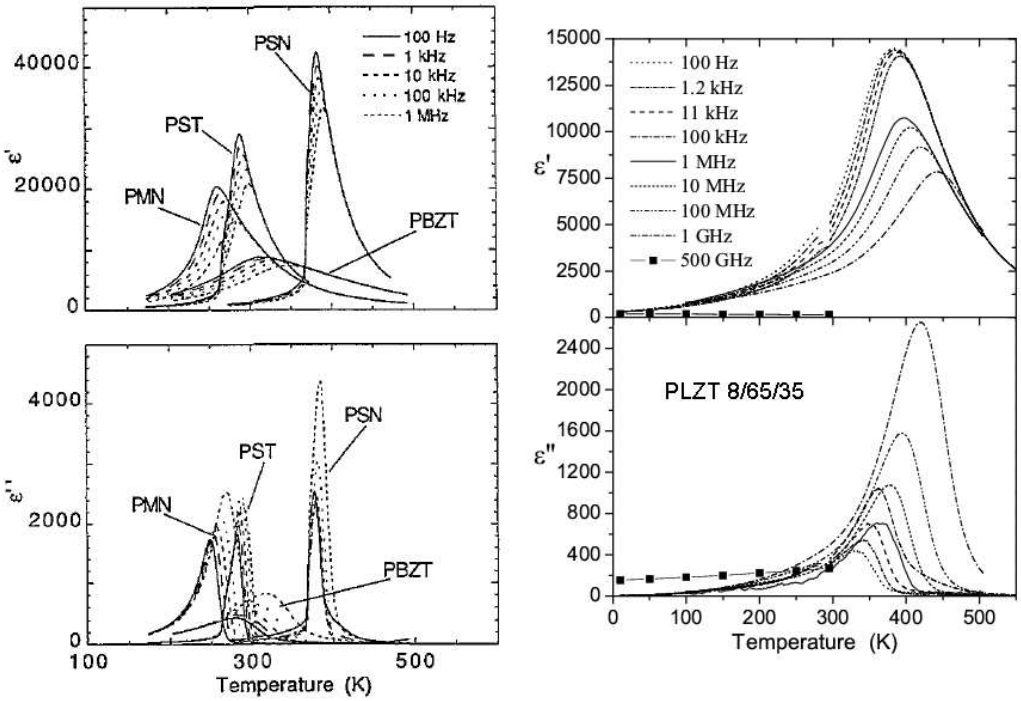

Figure 3.3: Real (a) and imaginary (b) parts of permittivity of typical relaxors as a function of temperature. Taken from [115] and [116].

demonstrates a usual ferroelectric behavior whereas disordered PST shows the dielectric properties typical for relaxor ferroelectrics [117]. X-ray diffraction, transmission electron microscopy and infrared spectroscopy study of the disorder in PMN, PST and other $A(B'_{1/2}B''_{1/2})O_3$ perovskites are presented in [118].

The Curie-Weiss law is valid in relaxor ferroelectrics only above a temperature T_d (called Burns temperature) which is appreciably higher than the temperature of the permittivity peak. For example, in PMN the maximum of permittivity is around 270 K and $T_d \simeq 600$ K. Burns and Dacol analyzed temperature behavior of refractive index of PLZT [119], PMN and PZN ($Pb(Zn_{1/3}Nb_{2/3})O_3$) [120] relaxor crystals and demonstrated that these crystals possess a local randomly oriented polarization below T_d. In contrast to ordinary ferroelectrics with macroscopic polarization domains, the non-vanishing polarization is a local property of relaxor ferroelectrics on a nanometer scale. Owing to the random orientation of the polarization nanoclusters, which are closely related to the lattice disorder, the average macroscopic polarization in the sample is zero.

The difference between relaxors and ordinary ferroelectrics appears in the temperature behavior of hysteresis loop and its parameters such as remanent polarization P_r and saturation polarization P_s. The large remanent polarization observed in ordinary ferroelectrics below T_c is a manifestation of the cooperative nature of the ferroelectricity (Figure 3.4a). A relaxor, on the other hand, exhibits a so-called slim loop, as it is shown on the right-hand side of the Figure. For sufficiently high electric fields the polar nanodomains can be oriented by the electric field which leads to a large macroscopic polarization; however, on removing the field most of these domains randomize their orientations resulting in a small P_r. The small but non-vanishing P_r value is an evidence of the presence of some degree of cooperative freezing of nanodomains.

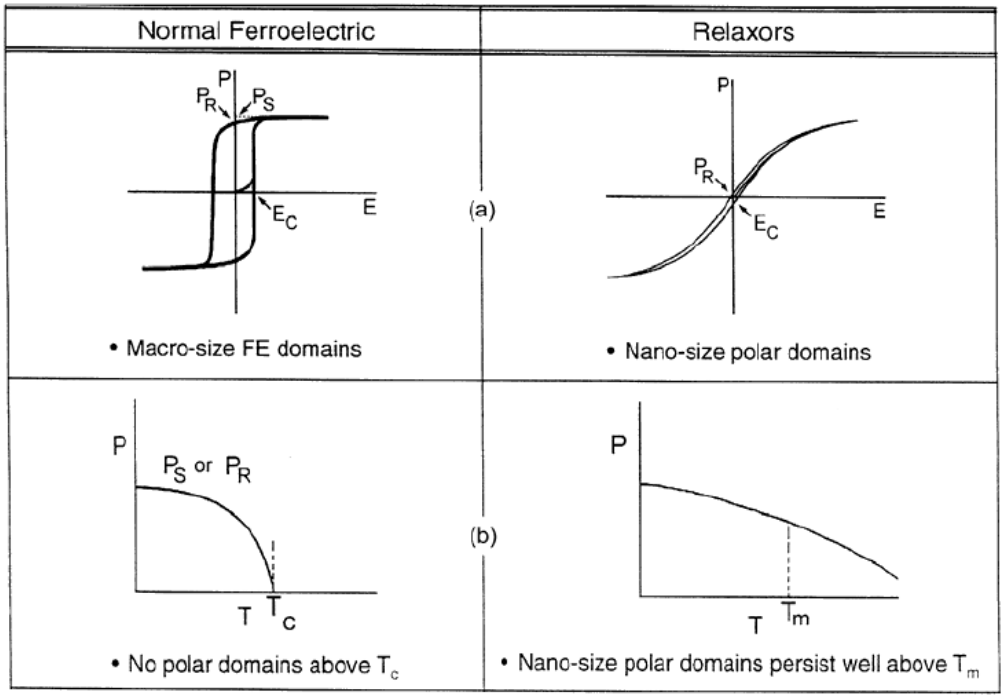

Figure 3.4: Comparison of polarization response of relaxors and ordinary ferroelectrics. Taken from [121].

The saturation and remanent polarization of normal ferroelectrics decrease with increasing temperature and vanish at the transition point (Figure 3.4b). No polar order exists above T_c. By contrast, the field-induced polarization of a relaxor decreases smoothly through the temperature of permittivity maximum T_m and persists to Burns temperature T_d well above T_m.

The deviation from the Curie-Weiss law in relaxors caused by the appearance of nanoclusters was described in analogy with the spin glass behavior [122]. Temperature dependence of the permittivity can by fitted by the modified Curie-Weiss law with an additional parameter of local order $q(T) = \langle P_i P_j \rangle^{1/2}$, where P_i and P_j denote the neighboring clusters dipole moments. $q(T) \simeq 0$ above T_d and increases below this temperature indicating an onset of short-range dipolar correlations. Fluctuations (hopping) of nanocluster polarization leads to the relaxational dielectric response. In the case of a single relaxation time τ, the complex permittivity is described by relation

$$\epsilon(\omega) = \epsilon'(\omega) - i\epsilon''(\omega) = \frac{\Delta\epsilon}{1 + i\omega\tau} + \epsilon_\infty \tag{3.4}$$

where $\Delta\epsilon$ is the dielectric contribution of relaxator and ϵ_∞ is the high frequency permittivity. Equation 3.4 was introduced by Debye [123] for the relaxation of polar molecules in liquids where the potential energy of the dipole can be considered as isotropic. In solids this situation does not hold and the symmetry of the potential is determined by the lattice symmetry. Thus the local dipole moment can switch between several minima of potential energy. It is easy to show that Equation 3.4 is valid for this case as well.

In the case of a thermally activated hopping of the dipole moment between equilibrium states, the relaxation time is temperature dependent and can be described by

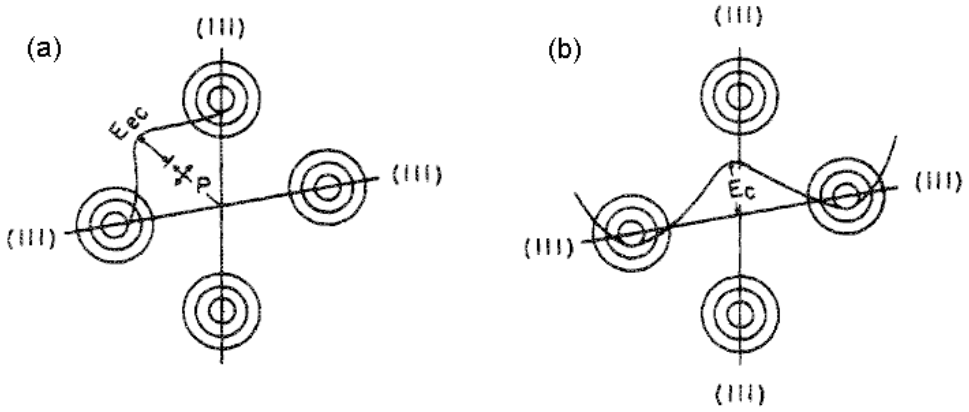

Figure 3.5: Potential well diagrams which illustrates activation energy for relaxational hopping between adjacent and opposite states of cluster polarization. Taken from [124].

the Arrhenius law

$$\tau(T) = \tau_0 \exp\left(\frac{E_a}{kT}\right) \tag{3.5}$$

where E_a is the activation energy (barrier between equilibrium states) and τ_0 is the characteristic time of thermal motion being of the order of inverse phonon frequencies. The most probable hopping mechanism corresponds to the lowest potential barrier between the polarization states. It can be illustrated by the example of PMN family of relaxors which are rhombohedral and have the potential wells along (111) directions (Figure 3.5). Generally the electrocrystalline anisotropy energy (barrier between adjacent states) is smaller than the heterophase fluctuation energy (barrier between opposite states) [124].

Equation 3.4 results in a peak of $\epsilon''(\omega)$ at frequency $\omega_m = 1/\tau$. Therefore it is easy to find $\tau(T)$ from the measurements of $\epsilon(\omega)$ spectra at different temperatures. However, often $\epsilon(T)$ curves are measured at few different frequencies ω only. Then the temperatures of permittivity or losses maxima T_m at different measurement frequencies ω are analyzed. In the simplest case of Debye relaxation with the relaxation time following the Arrhenius law, such approach can be used in the sense that $T_m(\omega)$ will also follow Arrhenius law. This is due to the fact that losses (or permittivity) as a function of temperature reaches the maximum when ω_m is approximately equal to the measuring frequency ω. However, the dielectric spectrum of relaxors is strongly multidispersive, i.e. contains a broad distribution of relaxation times. In this case, the permittivity can be described by empirical relations [125]. The most popular among them is the Cole-Cole relation

$$\epsilon(\omega) = \frac{\Delta\epsilon}{1 + i(\omega\tau)^{1-\alpha}} + \epsilon_\infty \tag{3.6}$$

where α is an empirical parameter describing diffuseness of the spectrum ($\alpha = 0$ for the Debye process). Another way to interpret diffused dielectric spectra is to introduce a distribution function of relaxation times $g(\tau)$ and consider the dielectric response of the relaxor ferroelectric as s sum of dielectric responses of Debye relaxators. Then

the complex permittivity can be presented in the form

$$\epsilon(\omega) = \Delta\epsilon \int_0^\infty \frac{g(\Omega) d\ln\Omega}{1 + i(\omega/\Omega)} + \epsilon_\infty \tag{3.7}$$

$$\int_0^\infty g(\Omega) d\Omega/\Omega = 1 \tag{3.8}$$

where $\Omega = 1/\tau$ is the relaxation rate and Equation 3.8 is the normalization condition. In the case of rather broad distribution $g(\tau)$, the behavior of $T_m(\omega)$ can essentially differ from the behavior of $\omega_m(T)$ (or generally $g(\tau, T)$). It was shown by Tagantsev [126] that the gradual broadening of the relaxation time distribution on cooling can lead to the Vogel-Fulcher behavior of $T_m(\omega)$. The latter behavior is described by the expressions

$$\omega_m^{-1}(T) = \tau(T) = \tau_0 \exp\left[\frac{E_a}{k(T - T_f)}\right], \tag{3.9}$$

$$T_m(\omega) = T_f - \frac{E_a}{k \ln \omega\tau_0} \tag{3.10}$$

where T_f is so called "freezing temperature" at which relaxation time tends to infinity. Equation 3.10 is commonly used for the systems with glassy behavior where below the finite temperature T_f system is frozen into a nonergodic state without macroscopic ordering [127]. In particular, it has been used to describe relaxation dynamics in PMN [128], PLZT [129] and other relaxor ferroelectrics [121].

One of the key questions related to the relaxor ferroelectrics is their ground state at low temperatures below T_f. Disordered polarization state of relaxor can be *empirically* considered as a dipolar glass state. However, the nature of transition into this state is still under debate. Two common points of view on this problem exist in the literature. The first one in based on the model of orientational glasses [130] and has been applied to PMN [131, 128] and PLZT [129] relaxor ferroelectrics. The following experimental facts support this model: (i) a Vogel-Fulcher-type critical slowing down of relaxation dynamics has been observed, (ii) the third order nonlinear susceptibility as a function of temperature has a maximum near the freezing point [128], (iii) the permittivity and remanent polarization below T_f depend on the sample history. The second point of view was proposed by Westphal, Kleemann and Glinchuk [132] and suggests the ground state of relaxor as nanodomain ferroelectric state. The main role in this model is played by quenched random fields which break the system into domains. Birefringence measurements done on PMN single crystals revealed hysteretic behavior and electric field induced Barkhausen jumps typical for system with ferroelectric domains [132].

Both mentioned models of relaxor ground state have some inconsistencies. Recently, a new spherical random-bond – random-field model of relaxor ferroelectrics [133] has been developed in order to provide a more general view on the nature of "freezing" in relaxors. In particular, it explains finite values of the nonlinear susceptibility at the freezing point. This model predicts a coexistence of two phases, namely, a glass phase without long-range order and a long-range ordered polarized ferroelectric phase. Therefore the predicted permittivity and nonlinear susceptibility do not diverge at freezing point as it could be expected for the permittivity of pure ferroelectrics or for nonlinear susceptibility of orientational glasses.

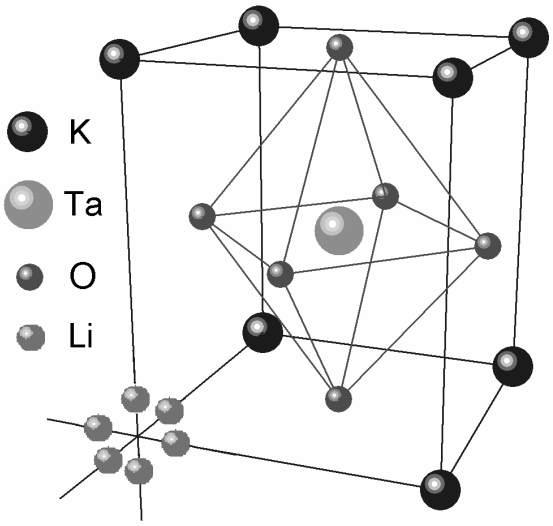

Figure 3.6: $KTaO_3$ unit cell with one off-center Li ion on A-site equally distributed among six local minima.

3.1.2 Doped incipient ferroelectrics

Perovskite relaxor materials, like PMN and PST, considered in Section 3.1.1 can be called "intrinsic relaxors". They are true chemical compounds with a fixed composition, in which the high level of structural disorder produces the relaxor state. On the other hand, materials like PLZT possess relaxor properties due to chemical substitution of lead ions in PZT by aliovalent La^{3+} ions above certain concentration threshold. In this case, the parent PZT material has a well defined ferroelectric phase transition and the La-doping induces smearing of this transition. In addition, there is another group of perovskite relaxors, in which the parent material is a quantum paraelectric (incipient ferroelectric), like $SrTiO_3$ or $KTaO_3$, in which the ferroelectric instability is suppressed at low-temperatures. In this case, doping with some kind of ions can induce the ferroelectric phase transition or lead to relaxor-type behavior [121]. The formation of glass-like state is also possible in such systems [134, 130].

Several mixed systems with typical relaxor behavior were reported in the literature. Among the most studied are $K_{1-x}Li_xTaO_3$ (KLT), $KTa_{1-x}Nb_xO_3$ (KTN) and $Sr_{1-x}Ca_xTiO_3$ (SCT). Recently, an increasing interest has been devoted to $Sr_{1-1.5x}Bi_xTiO_3$ system (SBiT) [135]. The formation of these solid solutions is based on substitution of ions of the parent (host) lattice by the impurity ions. Li^+ and Ca^{2+} are believed to substitute A-site ions in KLT and SCT, whereas Nb^{5+} substitute B-site Ta^{5+} ions in KTN. Polarization clusters in doped incipient ferroelectrics are formed around impurity ions which tend to occupy an off-center position at their site. The dipole moment produced by an off-center shift of the impurity ion polarizes the host lattice in the neighborhood which leads to an effective increase of the dipole moment. It can be written as [134]

$$d_i^* = d_i[1 + \gamma(\epsilon_{ph} - 1)/3] \tag{3.11}$$

where d_i^* is an effective dipole moment of the dipole i ($\gamma \approx 1$ is the local field correction factor), d_i is the permanent dipole moment of the impurity and ϵ_{ph} is the dielectric constant determined by the phonon contribution.

The ionic radius of lithium at the A-site of $KTaO_3$ is about twice smaller than that of potassium. Therefore KLT has a relatively large space for the off-center displacement of Li. An approximate calculation of the local potential minimum for Li ion in KLT performed by van der Klink and Khanna [136] demonstrated that there are six equivalent off-center positions which are shifted by 1.35 Å along $\langle 100 \rangle$ directions from the equilibrium potassium position. Schematic atomic arrangement in $KTaO_3$ unit cell with one Li ion hopping among six equivalent minima is shown in Figure 3.6. Recent *ab initio* calculations yield 0.6 Å [137] and 1.00 Å [138] for the $\langle 100 \rangle$ displacement. Experimental data for this value obtained by NMR study yield 1.26 Å [139]. Other investigations give values in the range from 0.5 to 1.6 Å (see [140] and references therein).

Situation in KTN is more complicated because Nb and Ta ions have approximately the same radius and the off-center displacement should be rather small. Nevertheless, Girshberg and Yacoby [141] have shown theoretically that a strong non-uniform electron-phonon interaction leads to the off-center displacements of Nb ions in KTN. The value of this displacement found by means of X-ray absorption fine-structure measurements [142] is 0.15 Å along $\langle 111 \rangle$ direction, i.e. by an order of magnitude smaller than Li displacement in KLT. On the other hand, *ab initio* calculations performed by Kvyatkovskii [137] predict narrow potential well for Nb atoms in KTN without off-center minima and a local vibration frequency higher than for Ta atoms. Thus the question about the value of Nb displacement in $KTa_{1-x}Nb_xO_3$ and about its role in observed phase transition has not been satisfactory answered, yet.

The interaction of impurities dipole moments with the soft mode and with each other leads to the phase transition above certain concentration level of the doping denoted as x_c. Near this concentration level the transition temperature T_c tends to zero (the displacive quantum limit) and, consequently, quantum effects have to be taken into account. The theory of such "quantum ferroelectric" transitions has been developed [143]. It predicts the behavior of the transition temperature $T_c(x)$ and of the inverse dielectric constant $\epsilon^{-1}(T)$ which are different from those predicted by the classical mean-field theory

$$T_c(x) \propto (x - x_c)^{1/2} \tag{3.12}$$

$$\epsilon^{-1}(T) \propto (T - T_c)^2. \tag{3.13}$$

The critical concentrations x_c found from experiments are 0.008 for KTN [144], 0.0018 for SCT [145] and 0.0005 for SBiT [135]. As to KLT, x_c is not well-defined for this system because of slow dynamics of Li ions at low temperatures. One can define a concentration $x_r = 0.022$ marking onset of relaxor-like response and appearance of the phase transition at finite temperature [146]. For SBiT, in our opinion, the situation is similar to KLT and relaxor-like behavior occurs for $x > x_r = 0.0267$ [135] but no clear signs of the phase transition have been found.

The detailed theory of random electric dipole interaction in highly polarizable lattice has been developed by Vugmeister, Glinchuk and other authors (see [134] and references therein). It was found that for dipoles in highly polarizable lattice there are two limiting cases expressed in terms of the quantity nr_c^3, where n is the impurity concentration and $r_c \propto \sqrt{\epsilon_{ph}}$ is the dipolar correlation length (the mean radius of the polarized region around impurity):

(i). The low concentration limit. The separation between dipoles is greater than

r_c, i.e. $nr_c^3 < N^*$, where N^* is a characteristic quantity for the given system. In this case, fluctuations of the polarization suppress the ferroelectric order and glass-like or relaxor state is formed at low temperatures. For very small impurity concentrations where $r \gg r_c$, the correlation effects are negligible: at low temperatures the dielectric behavior of the system is characterized by a Debye-like relaxation response of impurity dipoles superimposed on the response of the undoped system.

(ii). The high concentration limit. The separation between dipoles is much smaller than r_c, i.e. $nr_c^3 > N^*$. In this case, the system undergoes a ferroelectric phase transition with spontaneous polarization $\langle P \rangle = n\langle d^* \rangle$ at low temperatures.

A general picture of the behavior of highly polarizable systems with dipole impurities is presented in Figure 3.7 which depicts the theoretically predicted phase diagram for $\langle 111 \rangle$ oriented dipoles in a cubic lattice (similar to KTN system). Three possible phases including paraelectric (P), metastable dipolar glass with short-range order (DG) and mixed phase with ferroelectric and dipole glass properties ($F + DG$) are predicted. Characteristic quantity separating ferroelectric and dipole glass phases at low temperatures is $N^* = n_{cr} r_c^3 = 4.65 \cdot 10^{-3}$. Using this diagram one has to keep in mind that the quantities on both axes are temperature dependent in the case of incipient ferroelectric host lattice, because ϵ_{ph} strongly increases on cooling. Therefore the system trajectory on the phase diagram is not a vertical line, but a more complicated curve defined by the temperature behavior of ϵ_{ph}. Three such curves are shown schematically by the arrows in Figure 3.7. Trajectories 1 and 3 correspond to the low and high concentration limits and illustrate transitions to dipole glass and ferroelectric phases, respectively. However, trajectory 2 (intermediate concentration) demonstrates that the system may evolve on cooling to the dipole glass state and then, at low temperatures, become ferroelectric with macroscopic dipolar order. Thus, from the point of view of the presented theory, the problem of the ground state in relaxor ferroelectrics mentioned in Section 3.1.1 becomes even more complicated. The relaxor system may reveal properties typical for dipole glass transition (Vogel-Fulcher slowing down, peak of nonlinear susceptibility, etc.) but it may also exhibit a long-range dipolar order at very low temperatures where a transition to the ferroelectric phase may occur.

Dynamic dielectric response of random dipole system can be also described by the random-local-field theory. It was shown that the nature of the dipolar relaxation remains unchanged while the effect of dipole interaction leads to a change in the single-impurity relaxation rate above the phase transition. The theory predicts a critical slowing down of relaxation rate near T_c. In addition, in disordered systems, when $nr_c^3 < 1$ there is an additional relaxation mechanism associated to the presence of closely spaced polar nanoclusters formed by the correlated dipole impurities. The relaxation of such clusters is impeded because the interaction of dipoles in the cluster gives rise to additional potential barriers, which impede the reorientation of the dipoles. This mechanism is characteristic for the dipole glass systems. Because of random spacing of dipoles in clusters, a distribution of relaxation times takes place, which results in the broad dielectric dispersion. Similar theoretical assumptions were made by Prosandeev *et al.* [147, 138] in the case of KLT, where Li-Li pairs reorientation was considered for the explanation of the observed additional broad relaxation peak.

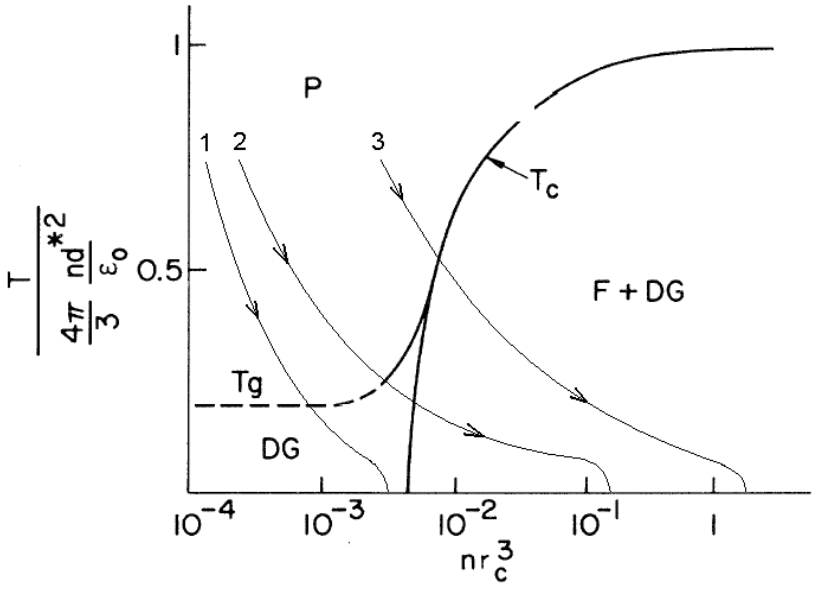

Figure 3.7: Phase diagram of the random dipole system taken from [134]. P is a paraelectric phase; DG is a dipolar glass state; $F + DG$ is a mixed phase with coexisting ferroelectric and dipole glass properties. The arrows schematically shows system trajectories on cooling.

Concerning the soft mode behavior in doped incipient ferroelectrics, there is a lack of theoretical models. In a sense, it is a consequence of the striking difference of the soft mode behavior in different systems. For instance, it was found that the soft mode frequency in KLT continuously decreases on cooling and increases with Li doping [148] while in KTN the soft mode frequency strongly decreases with Nb doping having minimum at phase transition temperature [149, 150].

The soft mode behavior in KTN can be rather well described by an Ising-like model which takes into account spin-phonon coupling [141, 151]. The theory predicts the value x_c of the critical concentration of quantum displacive limit which depends on the tunneling frequency of Nb ions among equilibrium positions. For $x > x_c$ the renormalized soft mode frequency tends to zero at T_c and KTN undergoes a displacive-type ferroelectric transition. More detailed analysis of the model including spin-spin correlations [141] leads to another important outcome which is the development of a central peak as temperature approaches T_c. The intensity of the central peak critically increases near T_c, while the soft mode frequency saturates at a value of a few cm^{-1}. These results are in agreement with Raman [152, 153] and hyper-Raman [149] results on the KTN system.

On the other hand, explanation of the soft mode stiffening in KLT is given only by the phenomenological model proposed by Vogt [154, 148] which suggests the local random electric fields as the main reason for the softening suppression. The model is based on an analogy with the action of macroscopic external electric field which is known to suppress soft mode softening in $KTaO_3$ and $SrTiO_3$ [155].

3.2 Experimental results and discussion

A great number of experimental work has been devoted to the investigation of relaxor ferroelectrics. A large number of known techniques including Raman [156, 157, 158, 159], hyper-Raman [160, 161, 149] and dielectric [145, 135, 162, 163] spectroscopies, optical measurements [132, 119, 164], inelastic neutron scattering [150, 165, 166, 167], x-ray study [168, 142, 169], magnetic resonance methods [170, 171] and others have been applied. However, concerning far IR and submillimeter spectroscopy, there are not so many publications comparing to other spectroscopic methods. Combined IR reflectivity and submillimeter transmission study of complex perovskite ceramics including PMN and PST was performed by Reaney *et al.* [118]. The results of IR spectroscopy of PLZT [172, 173] and PST [174] relaxors are devoted to the investigation of the influence of lattice disorder on phonon modes. Concerning doped incipient ferroelectric systems with relaxor properties, to the best of our knowledge, no systematic study by means of IR and THz spectroscopy has been published yet, except some publications of our lab [41, 175]. Nevertheless, such measurements can bring a valuable information about polar excitations in relaxor ferroelectrics and build a bridge between IR and MW ranges of dielectric spectrum in these materials.

The aim of the present study was to apply the terahertz spectroscopy to the investigation of dielectric response of relaxor systems and combine the results with those of other methods such as low frequency, microwave, FTIR spectroscopy etc., in order to determine the soft mode behavior, possible structural changes in the materials and the existence of "central peak"-like excitations. The studied doped incipient ferroelectrics systems were KLT, KTN single crystals and SBiT ceramics of different compositions.

3.2.1 $K_{1-x}Li_xTaO_3$ crystals

Composition of the studied samples

$K_{1-x}Li_xTaO_3$ single crystals were provided by P. P. Syrnikov (Ioffe Physical-Technical Institute, St-Petersburg, Russia) and S. Kapphan (University of Osnabrück, Germany). The crystal growth was carried out by spontaneous crystallization from a slowly cooled flux. More details can be found in [176]. KLT composition was formed in reaction:

$$Ta_2O_5 + (1-x)K_2CO_3 + xLi_2CO_3 \rightarrow 2K_{1-x}Li_xTaO_3 + CO_2. \qquad (3.14)$$

However, it is well-known that the concentration of Li in the grown KLT crystal is smaller than the concentration in the melt. Precise determination of actual Li content in KLT crystal is not an easy task because many physical methods of analysis are relatively insensitive to light atoms. One of the most reliable methods in this case is nuclear magnetic resonance (NMR) on the isotope ^{7}Li, which constitutes 92.4% of natural lithium. NMR experiments carried out by van der Klink and Rytz on KLT crystals revealed the empirical rule [177]

$$x_{\mathrm{NMR}} = (0.35 \pm 0.05)x_m \qquad (3.15)$$

which determines relation between Li concentration in the melt x_m and actual Li concentration in the crystal measured by NMR x_{NMR}. On the basis of NMR results,

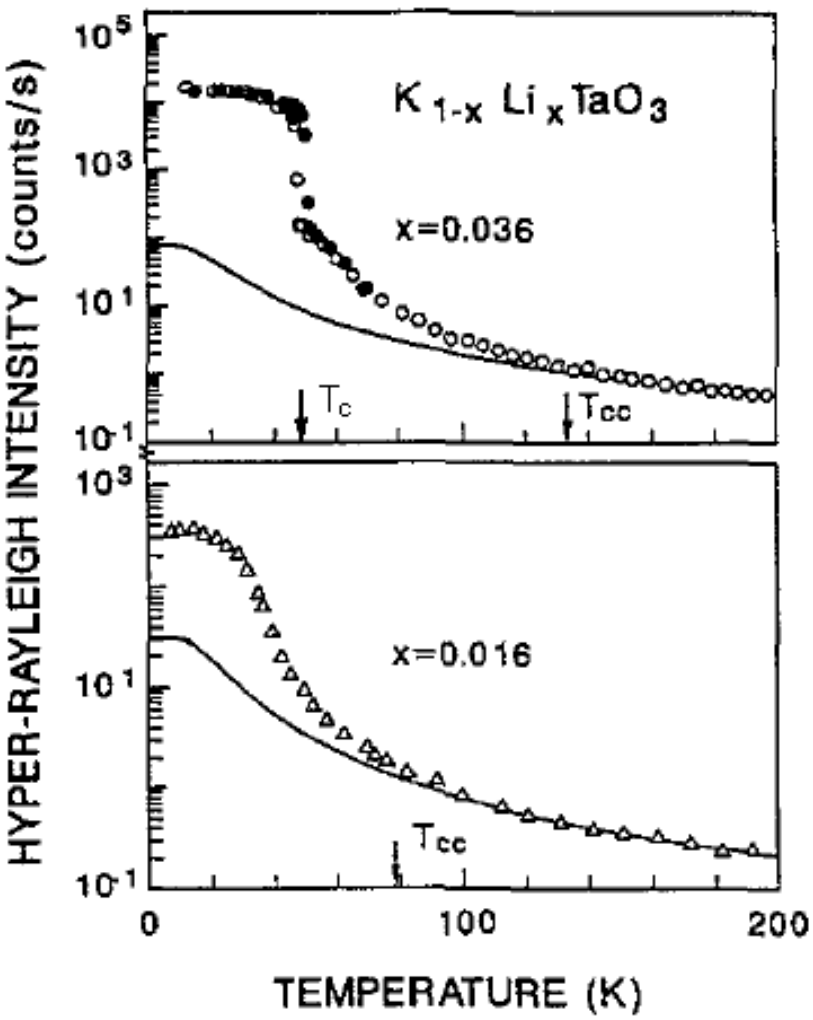

Figure 3.8: Temperature dependence of the SHG (hyper-Rayleigh) intensity of $K_{1-x}Li_xTaO_3$ taken from [154]. Thermal hysteresis is only observed for $x = 0.036$ (open circles refer to cooling, full circles to heating). The solid lines describe the asymptotic behavior in the limit of uncorrelated polarization clusters.

Voigt and Kapphan [178] suggested another indirect method of Li concentration analysis using second harmonic generation (SHG) technique. Their method is based on the measurement of temperature dependence of SHG in KLT crystal which shows a step-like increase below some characteristic temperature $T_{ch}^{\pm}$ ("-" or "+" signs designate cooling or heating cycle, respectively). The average temperature $T_{ch} = 0.5(T_{ch}^{-} + T_{ch}^{+})$ was found to be linearly related to Li concentration by the following formula

$$T_{ch} = 955x + 22. \tag{3.16}$$

SHG, which is forbidden in centrosymmetric $KTaO_3$, does not vanish in KLT due to the local breaking of inversion symmetry near off-center Li ions and a weak signal can be observed already at room temperature. The coherence length for SHG in $KTaO_3$ is $L_c = 2.8$ µm and it is almost temperature independent according to [179]. Therefore the SHG process can be considered as non-phase-matchable for small values of dipolar correlation length ξ_d compared to the coherence length ($\xi_d \ll L_c$). It was shown that for this conditions the SHG intensity behaves as $I^{2\omega} \propto \xi_d L$, where L is the crystal

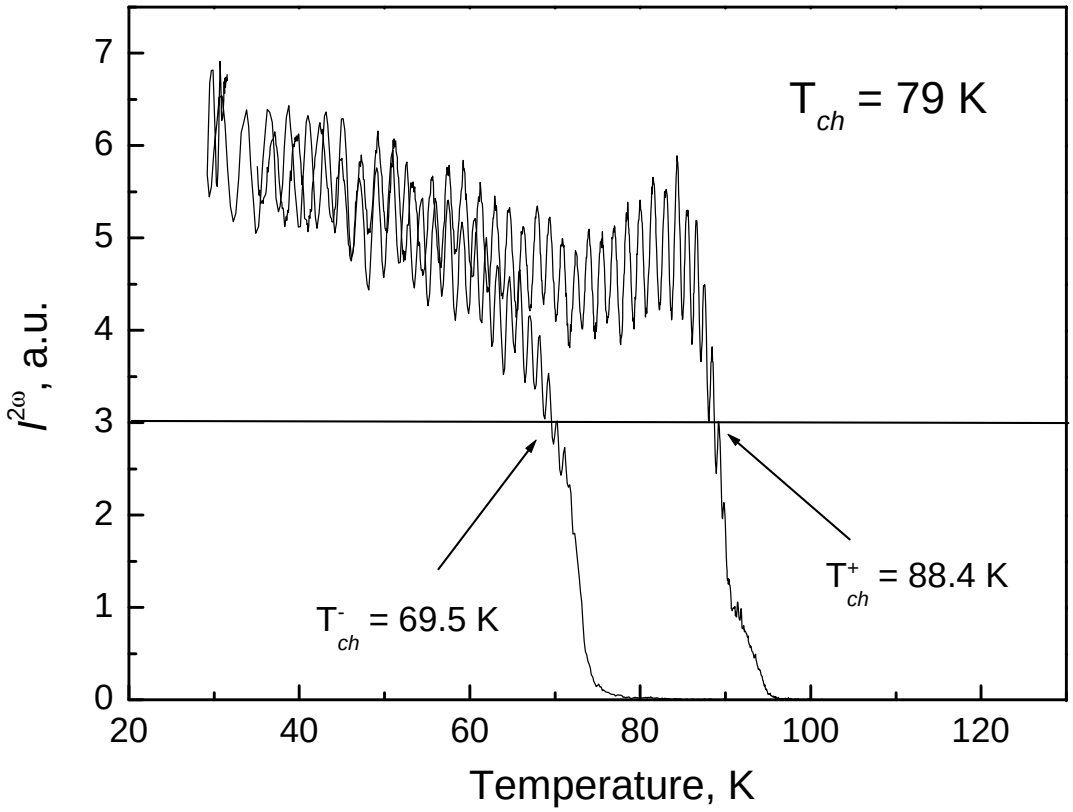

Figure 3.9: Temperature dependence of the SHG intensity for KLT-10 on cooling and heating cycles.

length [180]. Thus $I^{2\omega}$ continuously increases on cooling starting from the room temperature because $\xi_d \simeq r_c \propto \sqrt{\epsilon_{ph}(T)}$. This is demonstrated in Figure 3.8 taken from [154]. On further cooling, below cluster coalescence temperature T_{cc} introduced by Vogt [154] at which nearest polar clusters start to overlap, $\xi_d > r_c$ and $I^{2\omega}$ increases faster than $\sqrt{\epsilon_{ph}(T)}$. A step-like increase of $I^{2\omega}$ may occur at lower temperatures for KLT with $x > 0.022$ indicating an onset of long-range dipole correlation in the system [181, 182, 154]. This phenomenon can be considered as a phase transition of the first order, i.e. it is characterized by thermal hysteresis (see Figure 3.8). We denote the transition temperature on cooling as T_c, obviously for $K_{1-x}Li_xTaO_3$ with $x > 0.022$ $T_c = T_{ch}^-$.

The above described picture of SHG process in KLT is consistent with the theoretical predictions for random-dipole systems mentioned in Section 3.1.2. $K_{1-x}Li_xTaO_3$ system with $x < 0.022$ corresponds to the phase trajectory 1 in Figure 3.7 which crosses the line between paraelectric and dipole glass states at temperature $T_g = T_{cc}$. For $x \geq 0.022$ the trajectory 2 describes situation when, in addition to the glass transition, another ferroelectric-like transition occurs at the point where trajectory 2 crosses the line between glass and ferroelectric phases.

The samples of nominally pure $KTaO_3$ and $K_{1-x}Li_xTaO_3$ with $x = 0.016$ and 0.043 were supplied by S. Kapphan; the provided Li concentrations x were determined using Equation 3.16 and SHG method. Other two KLT samples were provided by P. P. Syrnikov and they are identical to the samples investigated in [147] with nominal Li concentrations $x = 0.006$ and 0.043. The last sample has $x_m = 0.1$ and we designate it as KLT-10 in order to avoid confusion with KLT sample with $x = 0.043$ provided

by S. Kapphan. In order to check Li content in these samples we have performed measurement of SHG as a function of temperature. The samples were prepared in the form of few millimeters thick plate with polished surfaces. The SHG signal was generated by a pulsed Q-switched Nd-YAG laser (pulse energy 0.15 mJ, pulse duration 7 ns, repetition frequency 20 Hz) and detected by a photomultiplier and a gated boxcar integrator. The obtained SHG intensity for KLT-10 is shown in Figure 3.9. Oscillations of SHG intensity below the phase transition are probably due to the interference of second harmonic wave inside the sample. The obtained characteristic temperature, $T_{ch} = 79$ K, gives $x \simeq 0.06$ using Equation 3.16. Thus Li concentration in KLT-10 is even higher than can be expected from van der Klink and Rytz empirical rule (Equation 3.15). Similar characterization of $K_{1-x}Li_xTaO_3$ having the nominal concentration $x = 0.006$ was not possible because of very weak SHG signal and the restricted validity of Equation 3.16 is the range of small Li concentrations ($x < 0.01$).

Far IR and THz data

FTIR spectra of all studied samples were measured in the temperature range 10 – 300 K. Typical reflectivity spectra of nominally pure $KTaO_3$ and KLT with $x = 0.043$ at three chosen temperatures are presented in Figure 3.10. For cubic perovskite $KTaO_3$ crystal (space group $Pm\bar{3}m$) three phonon modes with F_{1u} symmetry are observed as predicted by the factor-group analysis. The soft mode frequency is the only phonon eigenfrequency which exhibits appreciable changes on cooling. This appears in the spectra as a shift of the low-frequency wing of the reflectivity curve towards lower frequencies.

The spectra of KLT sample do not reveal any additional phonon modes within the experimental sensitivity. Generally, the reflectivity curves of all KLT samples are very similar except the soft mode behavior and some difference in damping constants of phonons (this is discussed below).

THz complex permittivity of KLT samples was measured by TDTTS and BWO spectroscopy techniques. The samples were prepared for the measurements in the form of plane-parallel (100)-oriented plates with thicknesses around 100 µm. A combined fitting of the FTIR reflectivity spectra with the THz spectra of complex permittivity was performed using factorized oscillator model (Equation 1.29). Example of such a fit for KLT with 1.6% of Li at 150 K is shown in Figure 3.11.

The deviation of the measured reflectivity from the fit near the high frequency edge of the spectrum is due to measurement errors related to the weak signal of the source. One can notice that dielectric permittivity and losses in submillimeter range are in good correspondence to the fit, though the reflectivity shows some deviations from the fitting curve especially in the region of transverse soft mode frequency ($\omega_{TO1} \simeq 64.5$ cm^{-1} at 150 K) where a sharper increase of reflectivity should be observed. This is typical for the fits of KLT with $x \geq 0.016$ at low temperatures and can be due to the surface layer effect. The development of a chemically heterogeneous near-surface layer in $KTaO_3$ crystals with a structure that is different from the bulk $KTaO_3$ was demonstrated by Szot *et al.* [183]. The IR reflectivity is expected to be particularly sensitive to the dielectric properties of the surface layer (which are different from the bulk properties) within the reststrahl band (between TO_1 and LO_1 frequencies) where the penetration depth of probing radiation is very small and is comparable to the surface layer thickness. Therefore, for the fitting of the soft mode parameters, we

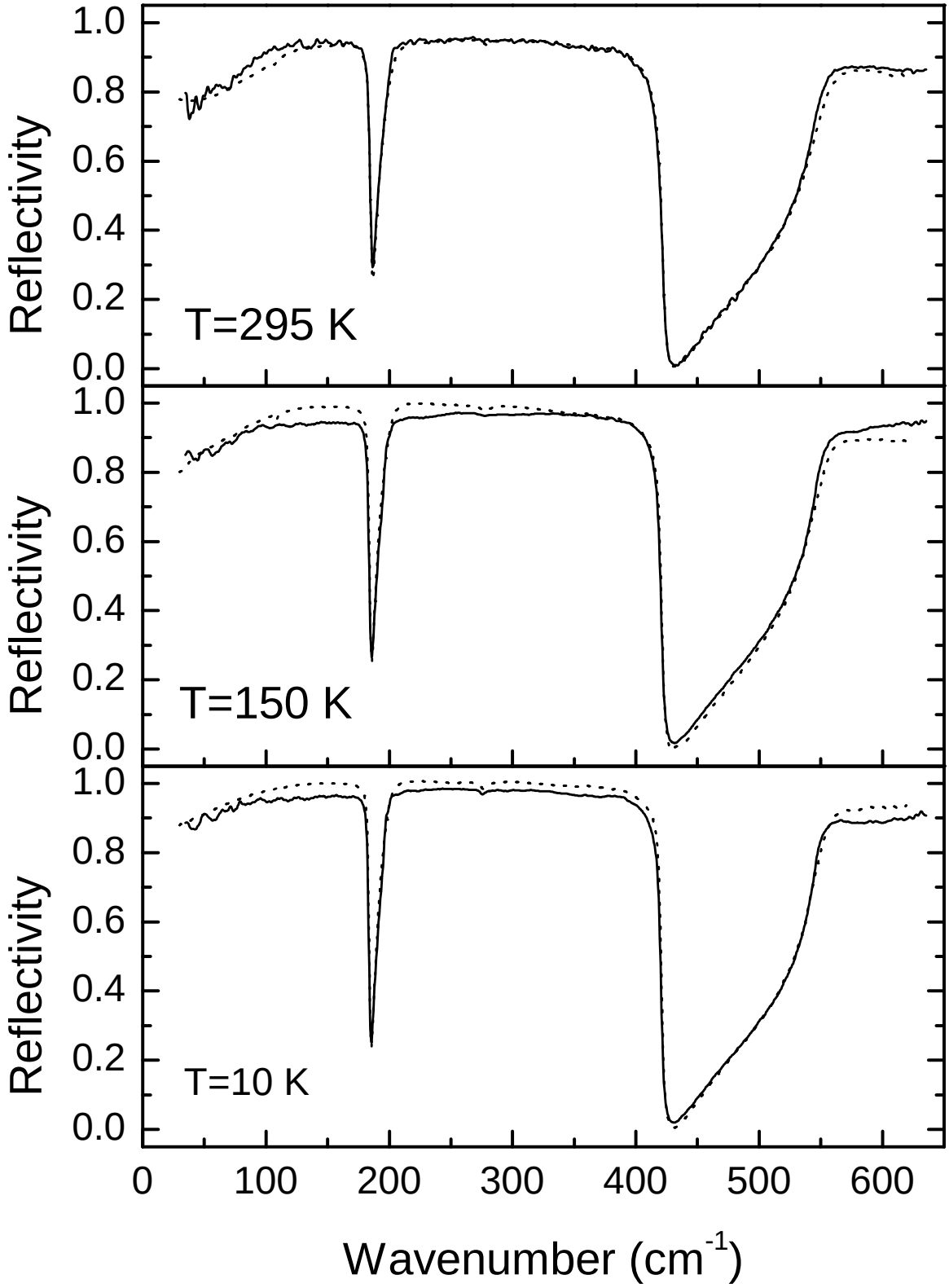

Figure 3.10: Far infrared reflectivity spectra of $KTaO_3$ (dotted line) and KLT with $x = 0.043$ (solid line) at 295, 150 and 10 K.

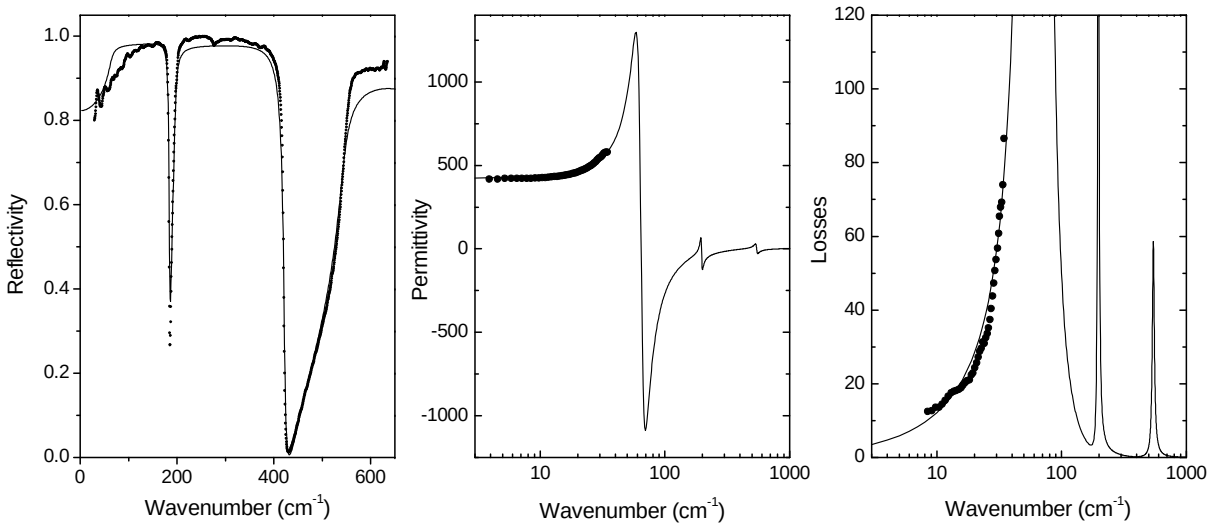

Figure 3.11: Results of combined fitting of IR reflectivity and THz complex permittivity of KLT with $x = 0.016$ at 150 K. Points are experimental results, lines correspond to the fit.

relied mostly on submillimeter permittivity data which are known to be more precise than IR reflectivity in this frequency range.

Frequencies of the phonon modes

As it was found from the fits, IR-active TO_2 and TO_4 phonon modes in $K_{1-x}Li_xTaO_3$ are located near 196 cm^{-1} and 543 cm^{-1}, respectively, and they are almost temperature and concentration independent. These results correspond rather well to previous IR measurements on pure $KTaO_3$ [184]. On the other hand, the soft TO_1 mode frequency is strongly temperature dependent as it is expected for quantum paraelectric systems. Figure 3.12 shows the temperature dependence of the soft mode frequency for all studied KLT samples. It is seen that the soft mode frequency monotonously hardens on Li doping, with exception of KLT $x = 0.006$. Hyper-Raman measurements of the soft mode frequency dependence on x in $K_{1-x}Li_xTaO_3$ [148] have demonstrated that it can be described rather well by the formula

$$\omega^2_{TO_1}(x,T) = \omega^2_{TO_1}(0,T) + x\beta(T) \tag{3.17}$$

where $\beta(T)$ is a temperature dependent coefficient. Similar dependence was found by Höchli *et al.* [185] from low frequency measurements of the KLT permittivity near 0 K. It can be obtained from Equation 3.17 using LST relation (Equation 3.2), because near 0 K all relaxations are frozen and do not contribute to the low-frequency permittivity.

The Li-induced hardening of the soft mode was explained by Vogt [148] as the frequency shift of an anharmonic oscillator biased by an external static force. In the case of KLT, the quasistatic (comparing to the soft mode frequency) polarization due to the off-center Li ions is supposed to act as a bias displacement of the soft mode, so that one expects

$$[\omega^2_{TO_1}(x,T) - \omega^2_{TO_1}(0,T)] \propto \langle P_s^2 \rangle \tag{3.18}$$

where $\langle P_s^2 \rangle$ is the mean square of Li-induced polarization averaged over the scale of the measurement wavelength λ. If the dipolar correlation length is much shorter than

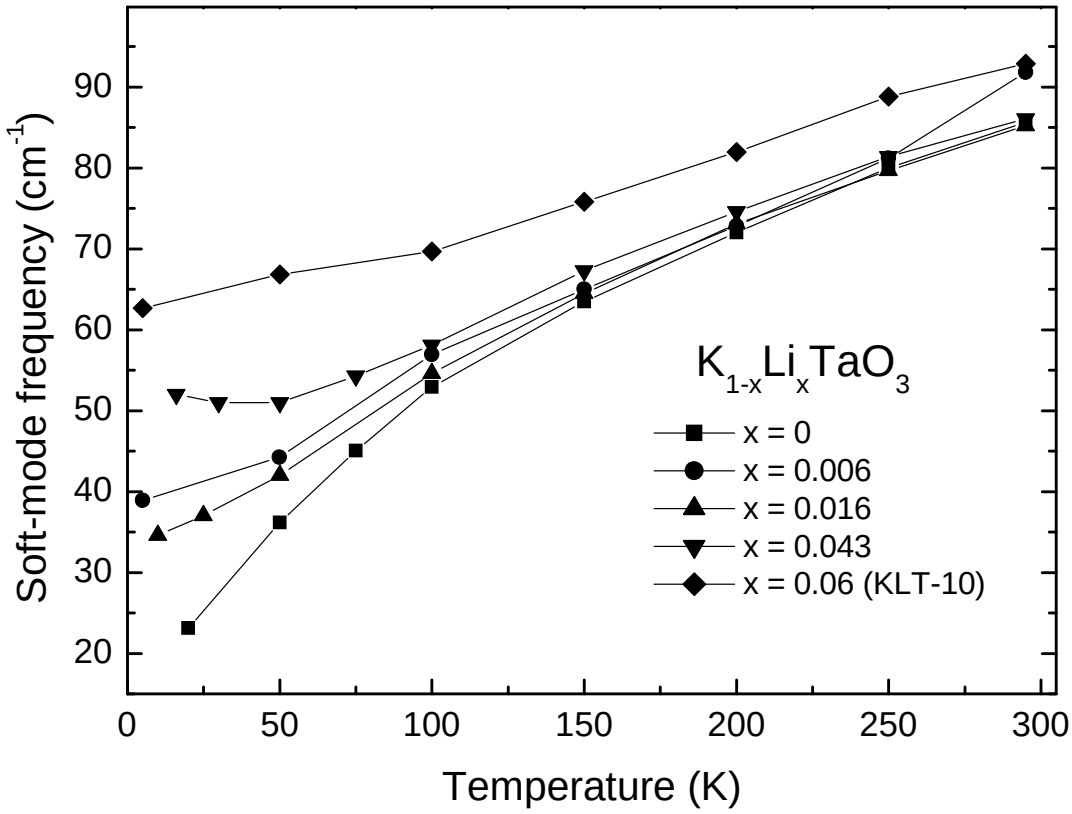

Figure 3.12: Soft mode frequency as a function of temperature for studied KLT samples.

the measurement wavelength ($\xi_d \ll \lambda$) which is fulfilled for the IR spectroscopy of KLT, then $\langle P_s \rangle = 0$ and $\langle P_s^2 \rangle \propto x$. Thus we obtain Equation 3.17.

The soft mode frequencies obtained from the fits are in good correspondence with hyper-Raman data [154, 148] for KLT with $x = 0.016$ and 0.043. On the other hand, KLT samples with $x = 0.006$ and KLT-10 have much higher soft mode frequencies than could be expected for their composition. According to precise measurements by Vogt [148], the soft mode in KLT saturates at a level below 30 cm^{-1} at helium temperature for $x = 0.008$ and below 60 cm^{-1} for $x = 0.087$. As it is seen in Figure 3.12, our samples have similar saturation near 40 cm^{-1} for $x = 0.006$ and above 60 cm^{-1} for $x = 0.06$ (KLT-10) though nominal Li concentrations for our samples are lower than for the samples studied by Vogt. The reason for these discrepancies can be the quality of KLT-10 and $K_{0.994}Li_{0.006}TaO_3$ single crystals which is probably lower than the quality of KLT with $x = 0.016$ and 0.043. The factors that affect the quality and decrease the permittivity of the crystals may be oxygen vacancies [186] or structural defects leading to internal stress.

Low-frequency relaxations in KLT

We have measured low-frequency (100 Hz – 1 MHz) dielectric spectra of the permittivity and losses in KLT. Figure 3.13 shows the spectra of KLT with $x = 0.043$. They demonstrate the behavior typical for moderately doped ($x \geq 0.016$) KLT crystals and they are similar to the spectra of classical relaxor ferroelectrics (see Figure 3.3). One can resolve two main relaxation processes which correspond to the peaks in

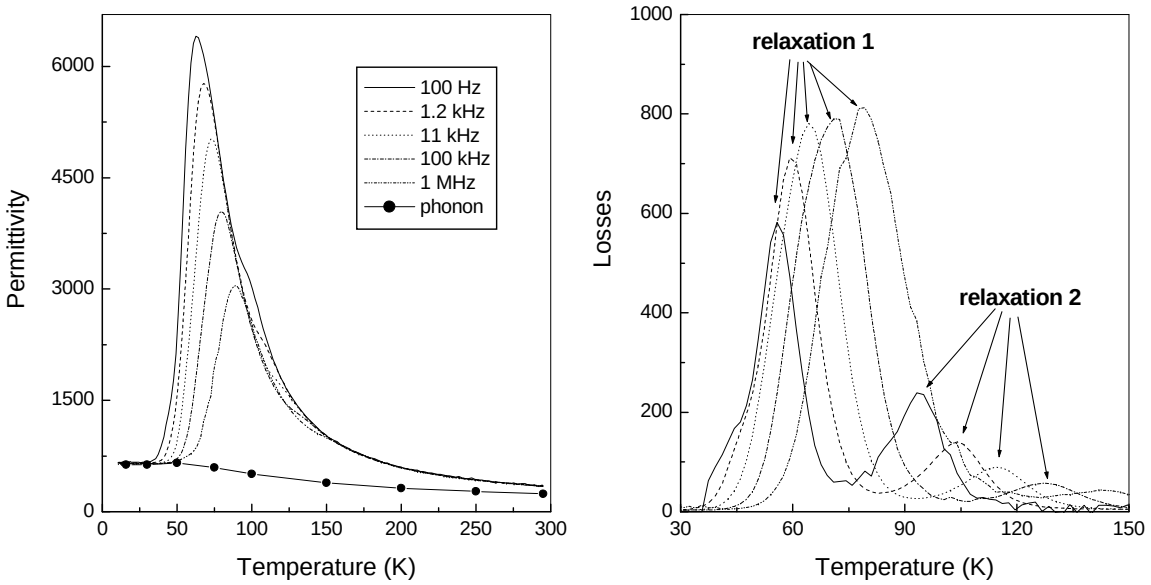

Figure 3.13: Low frequency spectra of permittivity and losses in $K_{1-x}Li_xTaO_3$ with $x = 0.043$ (cooling cycle). Full circles show the phonon contribution to permittivity obtained from the fits.

the temperature dependence of dielectric losses. They are denoted as "relaxation 1" (low temperature process) and "relaxation 2" (process at higher temperatures). The relaxation process 1 is related to the single lithium ions hopping between adjacent off-center positions (so called "$\pi/2$-jumps") [187]. The activation energy for this process $E_a = 931$ K is in agreement with the values reported in the literature [187, 170, 176]. The activation energy for the "π-jumps" which is about 0.4 eV (4640 K) [136] makes the probability of this kind of relaxation almost negligible. In this respect, relaxation in KLT is similar to that found in PMN where the potential barriers for cluster reorientation are suggested to exhibit the same kind of anisotropy [124] (see Figure 3.5). The relaxation process 2 has $E_a = 2554$ K and is assumed to be related to dipole pairs reorientation. It was suggested in [147] and confirmed by *ab initio* calculations [138] that this relaxation corresponds to π-reorientations of nearest Li dipoles which become energetically favorable due to the electric interaction between the dipoles. This point of view is supported by the observed increase of the dielectric contribution of relaxation 2 for higher Li concentrations.

It should be noted that no sharp dispersionless maximum of the permittivity corresponding to a ferroelectric phase transition is observed around temperature $T_{ch}^{-} \simeq 70$ K where the jump of SHG occurs in KLT-10. This fact indicates that the ferroelectric state below the transition probably has the same nature as the nanodomain ferroelectric state of PMN proposed in [132]. The sharp permittivity peak is smeared by the influence of random fields in KLT which are created by locally correlated Li ions. On the other hand, application of external electric field on cooling can align Li ions and induce a macroscopic ferroelectric state at low temperatures in KLT. Then the typical sharp maximum of permittivity is observed in the low-frequency measurements on zero-field heating cycle in KLT-10 [176, 188].

Full circles in Figure 3.13 show the phonon contribution to the permittivity evaluated from the fits of IR and THz data. Comparing this contribution with the low frequency permittivity we can make some conclusions about the dielectric strength

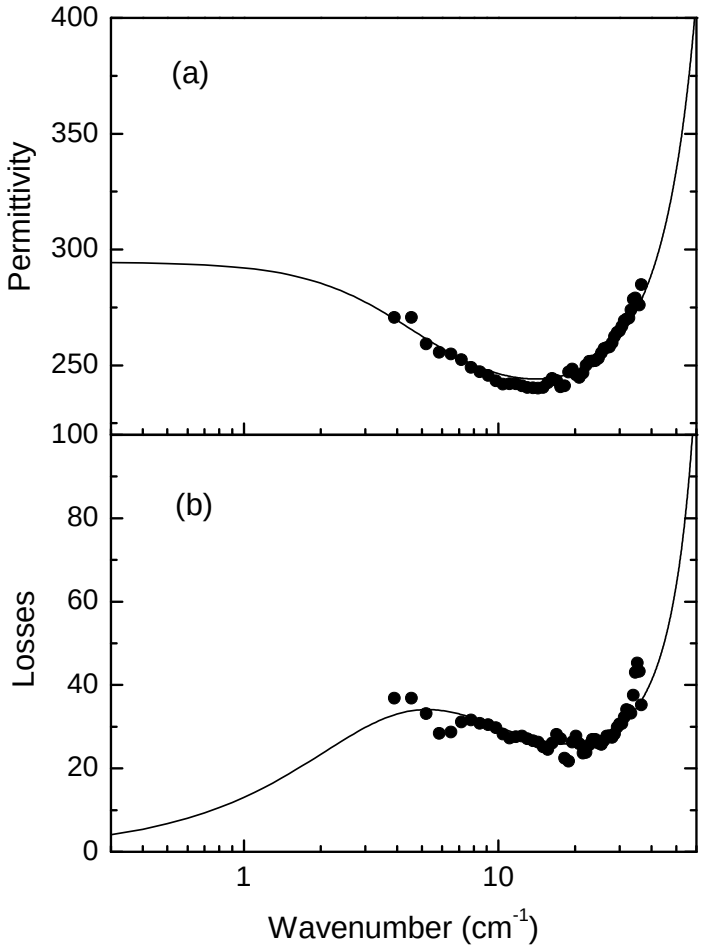

Figure 3.14: Room temperature THz permittivity (a) and losses (b) of KLT with $x = 0.043$. Lines show the fits with an additional overdamped oscillator mode describing the central peak.

of relaxation processes. At room temperature the low-frequency permittivity has no dispersion and it is slightly higher than the phonon contribution. Thus both relaxations are rather weak and lie above 1 MHz. The dielectric contribution of relaxations increases on cooling as it is seen from remarkable difference between IR and low frequency permittivities. Finally, at low temperatures ($T < 30$ K), both relaxation processes are slow compared to the measuring frequencies and do not contribute to low-frequency permittivity anymore. Therefore the phonon contribution coincides with the low frequency permittivity below 30 K.

"Central peak"-like dispersion

We have already pointed out that the soft mode hardens in Li-doped $KTaO_3$ compared to the pure one. Another significant difference between the THz spectra of these materials is an additional polar excitation which has been detected in KLT crystals below the soft mode frequency at room temperature. Figure 3.14 shows such "central peak"-type (CP) mode for KLT with $x = 0.043$. It has been fitted by an overdamped oscillator model (Equation 1.28). The same, even more pronounced, mode has been found in KLT-10. On the other hand, THz spectra of KLT with $x = 0.016$ show only

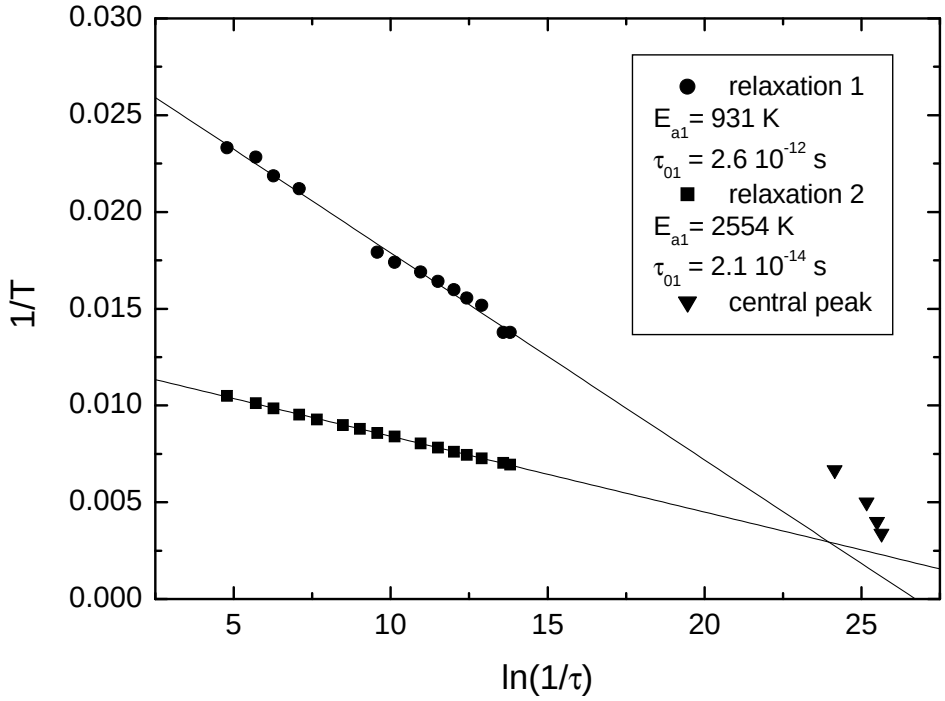

Figure 3.15: Arrhenius plot of relaxation time as a function of temperature for two low frequency relaxation processes and central peak in $K_{1-x}Li_xTaO_3$ with $x = 0.043$.

weak sign of the CP and it is completely vanishes in KLT with $x = 0.006$.

The observed central peaks shift to lower frequencies on cooling and disappear from the THz spectra below 150 K. Therefore one of the most probable mechanisms responsible for this excitation is a thermally activated hopping of Li ions. Figure 3.15 shows the Arrhenius plot for the relaxation processes 1 and 2 revealed by the low-frequency measurements (Figure 3.13) and for the CP. One can see that the straight lines corresponding to the Arrhenius law for relaxations 1 and 2 are crossing each other near the room temperature where the relaxation rates of both processes are approximately equal. However, the dielectric strength of relaxation 2 strongly decreases on heating as it can be seen in Figure 3.13. It is explained by the fact that the correlated motions of Li pairs related to relaxation 2 are suppressed by thermal fluctuations. Thus, at room temperature, the dielectric contribution of process 2 is expected to be negligible compared to process 1. We can conclude that the observed CP is a high frequency tail of relaxation 1 related to uncorrelated hopping of Li ions. The difference between the obtained relaxation rates of CP and the extrapolated rates of the relaxation 1 using Arrhenius law may come from the fitting model of the THz data. A simple Debye-like overdamped oscillator model has been used, while more relevant Cole-Cole model cannot be applied because of the restricted frequency range.

The THz spectra and the soft mode splitting below T_c

As it has been pointed out, KLT with $x > x_c$ undergoes the phase transition at temperature T_c. It is accompanied by an abrupt increase of the SHG intensity [154] and birefringence [157]. This kind of transition has been observed in our samples: KLT with $x = 0.043$ ($T_c \simeq 65K$) and in KLT-10 ($T_c \simeq 70K$) which have Li concentration above the critical limit $x_c = 0.022$ [182].

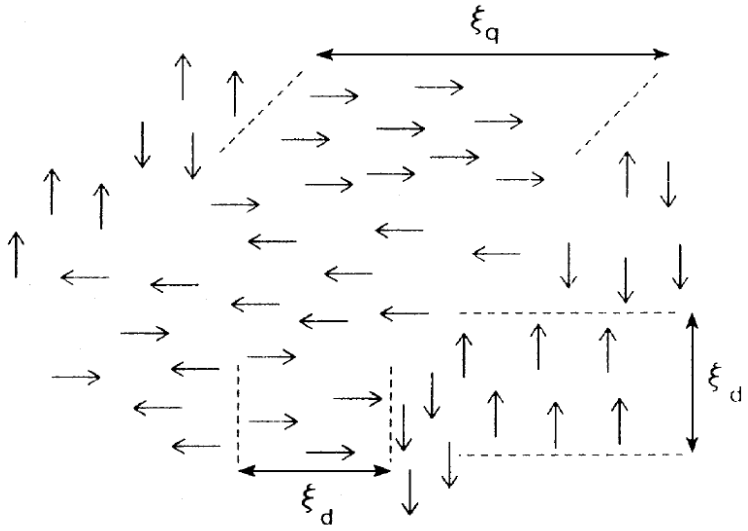

Figure 3.16: Schematic representation of dipolar and quadrupolar correlation lengths indicated by ξ_d and ξ_q, respectively. Taken from [189].

The temperature dependencies of SHG and birefringence in KLT are very similar. However, their origin is related to different correlation effects. While SHG intensity depends on dipolar correlation length ξ_d, the birefringence pattern is determined by quadrupolar correlation length ξ_q. The former length is defined by the linear size of the regions where dipoles have the same direction and orientation. The latter length ξ_q is defined by the linear size of the regions in which dipoles are parallel or antiparallel to each other. Two types of local dipoles ordering is schematically shown in Figure 3.16. One can note that $\xi_q > \xi_d$ in the figure. It was conclusively shown that the dipolar correlations are much smaller than the quadrupolar correlations [189]. Birefringence measurements demonstrated that the quadrupolar order spans over hundreds of nanometers [157, 182] (in [157] this correlation length was associated by mistake to ξ_d). On the other hand, the dipolar correlation length in KLT below T_c was found to be temperature independent: $\xi_d = 23$ nm for $x = 0.06$ and 12 nm for $x = 0.034$ [189]. For weaker Li doping ξ_d is smaller, for $x = 0.016$ the SHG experiments give $\xi_d \simeq 6$ nm [189], combined birefringence and SHG measurements yield $\xi_d \simeq 8$ nm [190] and the Raman measurements provide $\xi_d \simeq 1 \div 2$ nm [159].

Other manifestations of the phase transition in KLT are tetragonal distortion of the cubic KLT lattice [168] and splitting of the soft mode into A_1 and E components detected by inelastic neutron scattering [191] and Raman spectroscopy [157]. On the other hand, it was found that the soft mode splitting does not appear in hyper-Raman spectra of KLT with $x = 0.043$ [192]. This difference between Raman and hyper-Raman spectra of KLT was explained by Vogt [192] in terms of selection rules which are different for these techniques. The first-order Raman scattering is forbidden in centrosymmetric $KTaO_3$ lattice. Therefore the observed Raman signal is produced only inside polar nano-regions and the wavelength of the probed phonon is comparable to the size of nano-region. On the other hand, the hyper-Raman scattering is not forbidden in $KTaO_3$ and it typically probes phonons with wavelength about 120 nm [154]. Therefore if dipolar correlation length ξ_d is smaller than the wavelength of phonon probed by hyper-Raman, the split component A_1 of the soft mode will not be observable whereas Raman phonon wavelength is smaller than ξ_d and A_1 component is

visible. Based on this point of view, the soft mode splitting should not be observed in IR spectra as well because the probed wavelength is much larger than in hyper-Raman spectroscopy. However, the identification of the mode splitting in IR spectra is not straightforward as in the light scattering techniques and it needs a careful examination of the measured far IR reflection and THz transmission data.

Let us first examine complex permittivity calculated from THz transmission data. Figure 3.17 shows THz spectra of $K_{1-x}Li_xTaO_3$ with $x = 0.043$ at different temperatures. The permittivity gradually increases on cooling reaching its maximum value at 50 K and it saturates on further cooling. On the other hand, dielectric losses increase on cooling without any sign of saturation below 50 K and the sample becomes almost opaque below 15 K. Such a behavior of the complex permittivity cannot be fitted by a single soft mode oscillator. This is easily understandable, the permittivity behavior below 50 K would require a leveling-off of the soft mode frequency while the behavior of the losses would require further softening. Obviously, more complicated model which includes an additional polar excitation has to be used in order to describe the increase of the THz losses.

Nevertheless, one can conclude that the anomalous behavior of the complex THz permittivity is related to the phase transition in KLT even using simple single soft mode oscillator model fitting taking into account only the real part of complex permittivity. The soft frequency in KLT with $x = 0.043$ obtained from such a fit is shown in Figure 3.18 in comparison with hyper-Raman and Raman data of Vogt measured on a crystal with nominally the same Li concentration and provided from the same source. Above the phase transition temperature, the IR and hyper-Raman data are in reasonable agreement. Below the transition temperature, as it was pointed out, the hyper-Raman spectra reveal only the lower E-doublet and the higher A_1 component frequencies have been found from the fitting of Raman spectra published in [192]. The soft mode frequency obtained from IR spectra slightly increases on cooling below T_c and lies between the frequencies of E and A_1 modes. The fact that IR soft mode frequency starts to deviate from Raman and hyper-Raman frequencies around T_c indicates that the appearance of local polarization below T_c is responsible for the anomalous THz dielectric response.

Fitting of the THz and IR spectra below T_c

In order to fit the IR spectroscopy data of KLT below T_c we have to elaborate a model which takes into account ferroelectric-like state of the sample. For this purpose we consider the KLT crystal to be in a nano-domain state similar to that suggested by Westphal *et al.* for PMN [132]. The nano-domains are randomly oriented so that the net polarization is zero $\langle P_s \rangle = 0$. However, inside the domains the spontaneous polarization is non-zero and induces tetragonal splitting of the soft mode. Therefore the dielectric response of a single nano-domain is anisotropic and it is determined by the A_1 soft mode component along the polar c-axis and by the E soft mode component along a-axis. The size of nano-domains in KLT which affects the propagation of transverse optical modes (the soft mode in particular) [189] is of the order of dipolar correlation length ξ_d which is obviously much smaller than the wavelength of IR radiation in the sample. Therefore we have to calculate an effective complex permittivity averaged over a large number of nano-domains and use it for the fitting of the measured THz spectra.

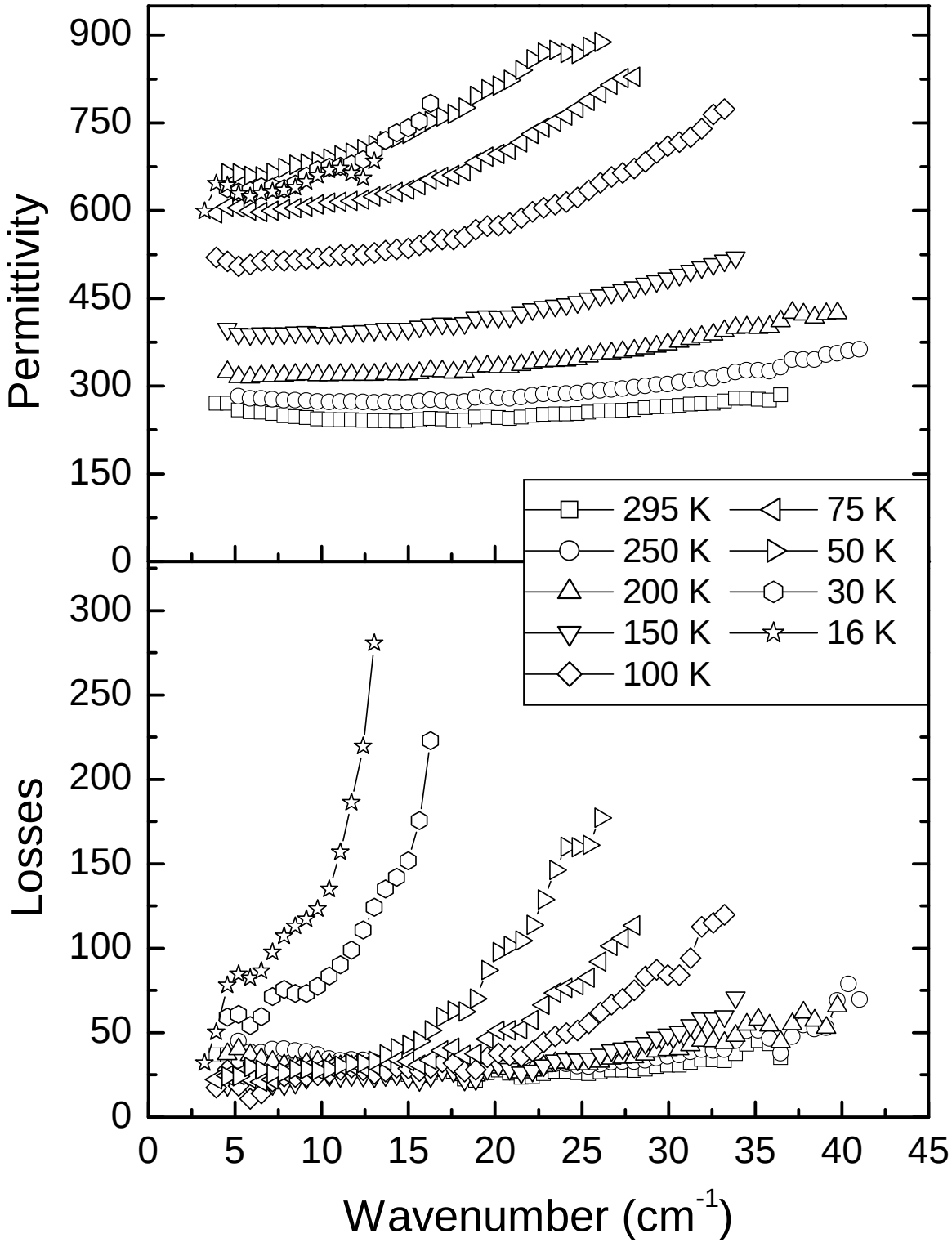

Figure 3.17: THz permittivity and losses in $K_{1-x}Li_xTaO_3$ with $x = 0.043$ at different temperatures.

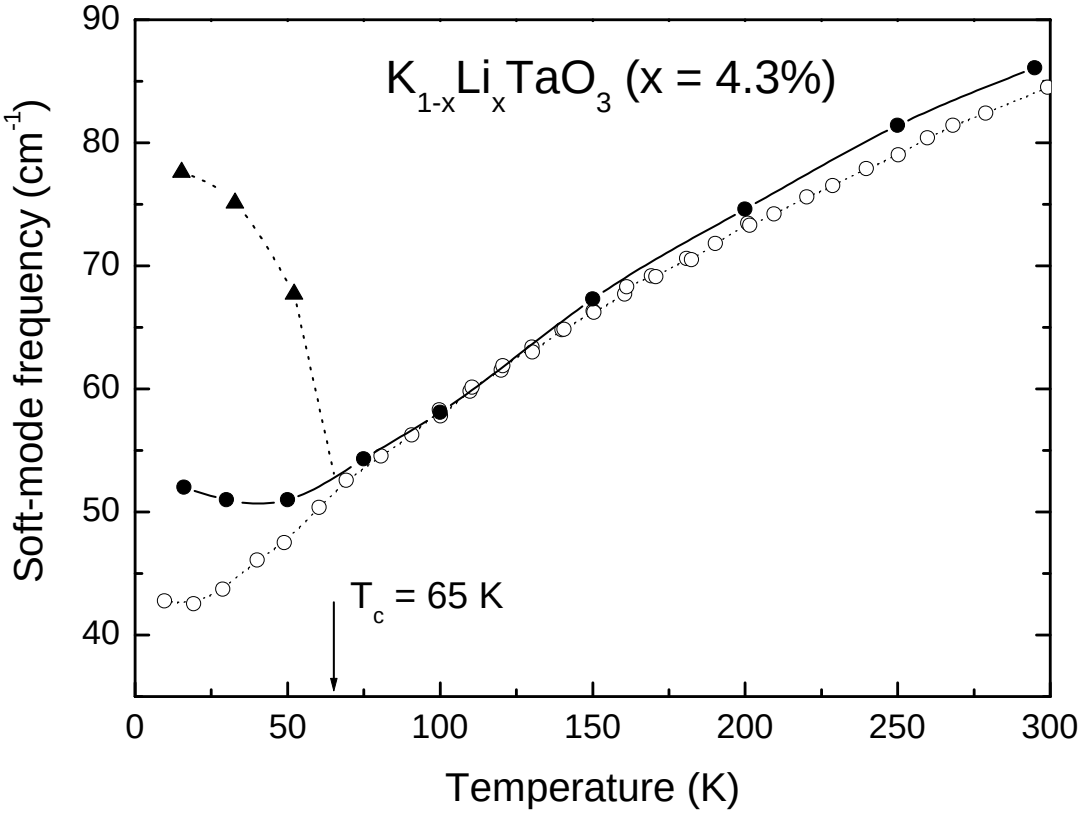

Figure 3.18: Soft mode frequency as a function of temperature in $K_{1-x}Li_xTaO_3$ with $x = 0.043$ determined by the fitting of IR reflectivity data together with THz permittivity (regardless of losses) compared to hyper-Raman (open circles) and Raman (triangles, A_1 component) spectroscopy data taken from [148, 192]. Lines are guided by eye.

Table 3.2: Phonon contribution to the permittivity below $T_c = 65$ K found from THz spectra ϵ_{THz} and calculated using EMA ϵ_{EMA} and permittivities of domains along c-axis ϵ_c and along a-axis ϵ_a together with the respective frequencies ω_{A_1} and ω_C of the soft mode components. The sample is $K_{1-x}Li_xTaO_3$ with $x = 0.043$.

Temperature	ϵ_{THz}	ϵ_{EMA}	ϵ_c	ω_{A_1}, cm^{-1}	ϵ_a	ω_E, cm^{-1}
50 K	655	645	385	67.7	808	46.7
30 K	630	668	312	75.1	911	44.0
16 K	630	694	293	77.6	976	42.5

The approach which we use for the calculation of effective dielectric response consists in following. The nano-domains are regarded as components of a composite material depending on their orientation with respect to external electric field. It means that domains having spontaneous polarization along the field have smaller permittivity (defined by the A_1 component of the soft mode) than domains where polarization is normal to the field (softer E mode is active in this case). There are several methods for calculation of the effective dielectric response of a composite with known permittivities of its components which are appropriate for different mixing topologies [193]. The effective medium approximation (EMA) approach is one of the most general among these methods and expresses the effective permittivity ϵ_{eff} of the composite consisting of two components with permittivities ϵ_1 and ϵ_2 by an implicit equation

$$f\frac{\epsilon_1 - \epsilon_{eff}}{\epsilon_1 + 2\epsilon_{eff}} + (1-f)\frac{\epsilon_2 - \epsilon_{eff}}{\epsilon_2 + 2\epsilon_{eff}} = 0, \tag{3.19}$$

where f is the relative concentration of component 1. The EMA is valid in the whole interval of relative concentrations $f = 0 \div 1$ of spherical particles of one component imbedded into the second component [193]. In our case, $\epsilon_1 \equiv \epsilon_c$ is the permittivity along the c-axis of nano-domain and $\epsilon_2 \equiv \epsilon_a$ is the corresponding permittivity along the a-axis. If there are some unpolarized regions of the lattice, we assume their permittivity to be equal to ϵ_a. This is plausible assumption because the soft mode frequency in the direction normal to polarization is only slightly different from the soft mode frequency in unpolarized crystal [155]. Random orientation of dipole moments implies $f = 1/3$ if the whole crystal volume is occupied by polarized nano-regions.

Our calculations have shown that application of EMA approach to KLT below the phase transition yields overestimated values of the permittivity at low temperatures if we use the soft mode frequencies (E component for ϵ_a and A_1 component for ϵ_c) from hyper-Raman and Raman spectra. The results of the calculations are summarized in Table 3.2 where the measured phonon contribution to the permittivity ϵ_{THz} is presented together with EMA permittivities ϵ_{EMA} and values used in EMA calculations. One can see that at 30 K and 16 K $\epsilon_{EMA} > \epsilon_{THz}$. On the other hand, the dielectric losses resulting from the model are much smaller than those observed in the experiment. As it was pointed out above, an additional fitting term is thus needed to describe the anomalous loss behavior. However, it cannot be included in the EMA model because there is no space for its contribution to the permittivity. The only way to get lower ϵ_{EMA} is to assume $f > 1/3$, i.e. larger relative concentration of the component with low permittivity. However assuming $f > 1/3$ means that nano-domains are not randomly oriented but have preferential orientation along measuring

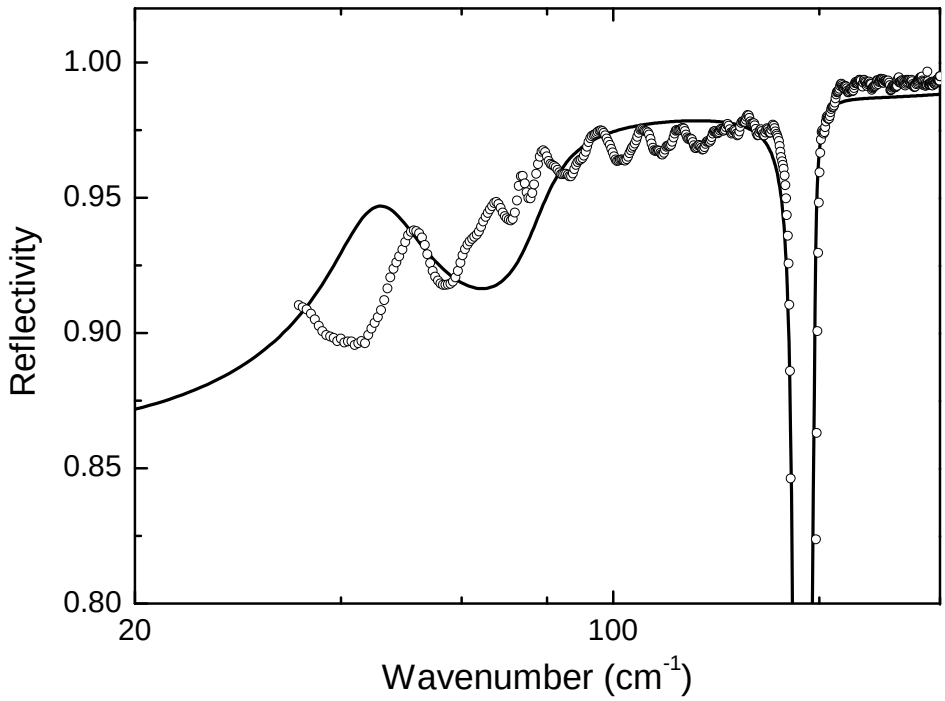

Figure 3.19: Reflectivity of KLT $x = 0.043$ at 16 K measured by FTIR spectroscopy (points) and calculated by EMA approach (line).

field direction. This would imply non-zero macroscopic polarization $\langle P_s \rangle \neq 0$ and would be in contradiction with experimental observations in KLT crystals [170].

Additional disadvantage of EMA approach consists in the soft mode splitting which is predicted to be noticeable in the reflectivity spectra. Figure 3.19 shows the calculated reflectivity at 16 K in comparison with the experimental data. The EMA model predicts a bump in the reflectivity due to the existence of A_1 component. The strength of this feature lies within the accuracy of FTIR measurements in this spectral range and a clear conclusion about its presence in the spectra cannot be made (see Figure 3.19). However, it seems that the FTIR reflectivity spectra rather exclude the splitting effect than confirm it.

The second possible approach for the calculation of effective dielectric response of a composite crystal is based on the Clausius-Mossotti equation (CME) which relates the permittivity of the material with microscopic polarizabilities of the atoms (or molecules). It can be written as

$$\frac{\epsilon - 1}{\epsilon + 2} = \frac{1}{3\epsilon_0} \sum_i n_i \alpha_i \tag{3.20}$$

where α_i and n_i are the polarizability and the concentration of atoms of kind i in the material. CME is based on the Lorentz approximation of local electric field which is valid in the case of simple cubic lattice or isotropic medium like gases and liquids. In more complicated cases the Lorentz field requires corrections according to the unit cell geometry and CME does not provide accurate results. This was demonstrated by Slater [112] for cubic perovskite lattices e.g. $BaTiO_3$. He found that local fields at B-site and oxygen site (lying on external field direction) atoms are enhanced by a factor of 8.2 comparing to the Lorentz field. This structural property of perovskites

is often responsible for their high values of the permittivity and for the ferroelectric instability. On the other hand, it was shown in [112] that the introduction of Lorentz field corrections in $BaTiO_3$ can be considered as a renormalization (namely enhancement) of Ti ionic polarizability in frame of CME. Therefore if we are not interested in the individual values of atomic polarizability and if we calculate permittivity of their mixture, CME can be the simplest and reasonable approximation.

In order to use CME for the calculation of effective composite permittivity we have to calculate first the polarizability factors of composite components. Taking into account Equation 3.20 their effective values can be found from the known values of permittivity

$$\Lambda_j(\omega) = \frac{\epsilon_j(\omega) - 1}{\epsilon_j(\omega) + 2} \tag{3.21}$$

where $j = 1$ or 2 for composite components (generally there may be more than two components). Then the resulted polarizability factor is written as linear combination of two components

$$\Lambda(\omega) = f\Lambda_1(\omega) + (1 - f)\Lambda_2(\omega). \tag{3.22}$$

The resulting effective permittivity can be found by inverting Equation 3.21

$$\epsilon_{eff}(\omega) = \frac{2\Lambda(\omega) + 1}{1 - \Lambda(\omega)} \tag{3.23}$$

One can show that the described method of calculations actually reduces to well-known formula of series capacitances in the case when permittivity of both components is rather high ($\epsilon_1, \epsilon_2 \gg 2$). Then the effective permittivity is expressed by the simple relation

$$\frac{1}{\epsilon_{eff}} = \frac{f}{\epsilon_1} + \frac{1 - f}{\epsilon_2}. \tag{3.24}$$

This approach was described by Böttcher [194]. Recently, the CME approach has been used by Levin *et al.* [195] for the calculation of permittivity and its temperature coefficient of $(1 - x)$ $Ca(Al_{0.5}Nb_{0.5})O_3$–$xCaTiO_3$ solid solution. To justify the applicability of this approach to solid solutions they refer to "the ion additivity rule" (analog of Equation 3.22) used by Shannon for determination of great number of ionic polarizabilities in oxides and fluorides [196].

The validity limits of the CME approach are not quite clear. For large enough particles (µm size or larger) of mixed components the EMA approach can be derived from the Maxwell's macroscopic equations [197] and thus it is more relevant than the CME approach. On the other hand, when components are mixed on atomic (molecular) level the application of CME seems to be reasonable and it is justified by the experimental results [195]. Hence the boundary between the regions of validity of the two mentioned approaches lies on the mesoscopic (nanometer) scale. We can suppose that nanodomains size in KLT is small enough and that the CME approach can be applied.

The fitting of the THz and IR results using the CME approach has been performed in the same way as for EMA calculations; the frequencies of the soft mode components and the corresponding permittivities used in the calculations are listed in Table 3.2. In contrast to EMA, CME calculations for $f = 1/3$ give underestimated permittivity values, i.e. the effective CME permittivity is affected by the low-permittivity component stronger than the EMA permittivity. Therefore, in order to fit the experimental

data, we treated f as a variable parameter. Moreover, an additional oscillator term have to be introduced in order to fit losses increasing below 30 K. The results of the fitting are presented in Figure 3.20. We show the reflectivity, permittivity and losses in comparison with the experimental data. The correspondence between measurements and fits is rather good. A small deviation is observed only in the low-frequency wing of the dielectric loss spectra at 16 and 30 K. Its origin is probably related to the fact that a single damped oscillator model is not fully adequate for the description of the additional polar excitation.

The results of the fits show that the relative concentration f exhibits a temperature dependence. One finds $f = 0.19$ at 50 K, $f = 0.25$ at 30 K and $f = 0.33$ at 16 K, i.e. f is gradually increasing on cooling reaching maximum value of 1/3 at 16 K. At higher temperatures $f < 1/3$. This indicates that polar nano-domains do not occupy the whole crystal volume and some regions with very short dipolar correlation length exist among them. The dielectric response of these regions is defined by the soft mode component E observed in hyper-Raman spectra and their relative concentration is equal to $1 - 3f$. Thus at 50 K about 60% of the crystal volume contain nano-domains with dipolar correlation and 40% is almost uncorrelated, the fraction of correlated volume increases to 75% at 30 K and practically the whole crystal volume is filled by nano-domains at 16 K. Owing to the approximate character of the CME approach used for the fitting and taking into account the approximation for the permittivity of uncorrelated lattice and existence of additional excitation in the spectra the relative concentrations of nano-domains given above are not precise. However they demonstrate qualitative picture of changes in polar ordering of KLT crystal below T_c and give deeper insight which could not be obtained by means of other experimental techniques.

Piezoelectric resonance in nanodomains

The observed additional polar excitation located around 15 cm^{-1} at 16 K and 30 K is responsible for increasing losses in the submillimeter range. Its contribution to the permittivity increases on cooling from 30 at 30 K to 55 at 16 K. As it was pointed out above, the shape of its absorption peak is more complex than for a simple damped oscillator. Let us discuss the nature of this excitation. Its rather high frequency at low temperature probably excludes the possibility that the process is thermally activated. On the other hand, the increasing dielectric contribution upon cooling excludes quasi-Debye loss mechanism (see Chapter 2) which should vanish at low temperatures. The reason for the enhanced THz losses can be a piezoelectric resonance in the nano-domains. Since the inversion symmetry is broken inside the nano-domains, acoustic deformation may couple to the electric field via piezoelectric effect. Similar mechanism was proposed for relaxor PLZT [116]. The frequency of acoustic resonance equals

$$f_r = \frac{1}{2d\sqrt{\rho s_{11}}}, \tag{3.25}$$

where d is the nano-domain size, ρ is the density of the material and s_{11} is the elastic compliance. Using the theoretical density of KLT $\rho \simeq 7400$ kg/m^3 and $1/s_{11} \simeq 370$ GPa for KLT with $x = 0.041$ taken from [198] and the experimental resonance frequency $f_r = 15$ $cm^{-1} = 450$ GHz we estimate the typical domain size $d \simeq 11$ nm. This value is rather close to the dipolar correlation length $\xi_d = 12$ nm in KLT $x = 0.034$

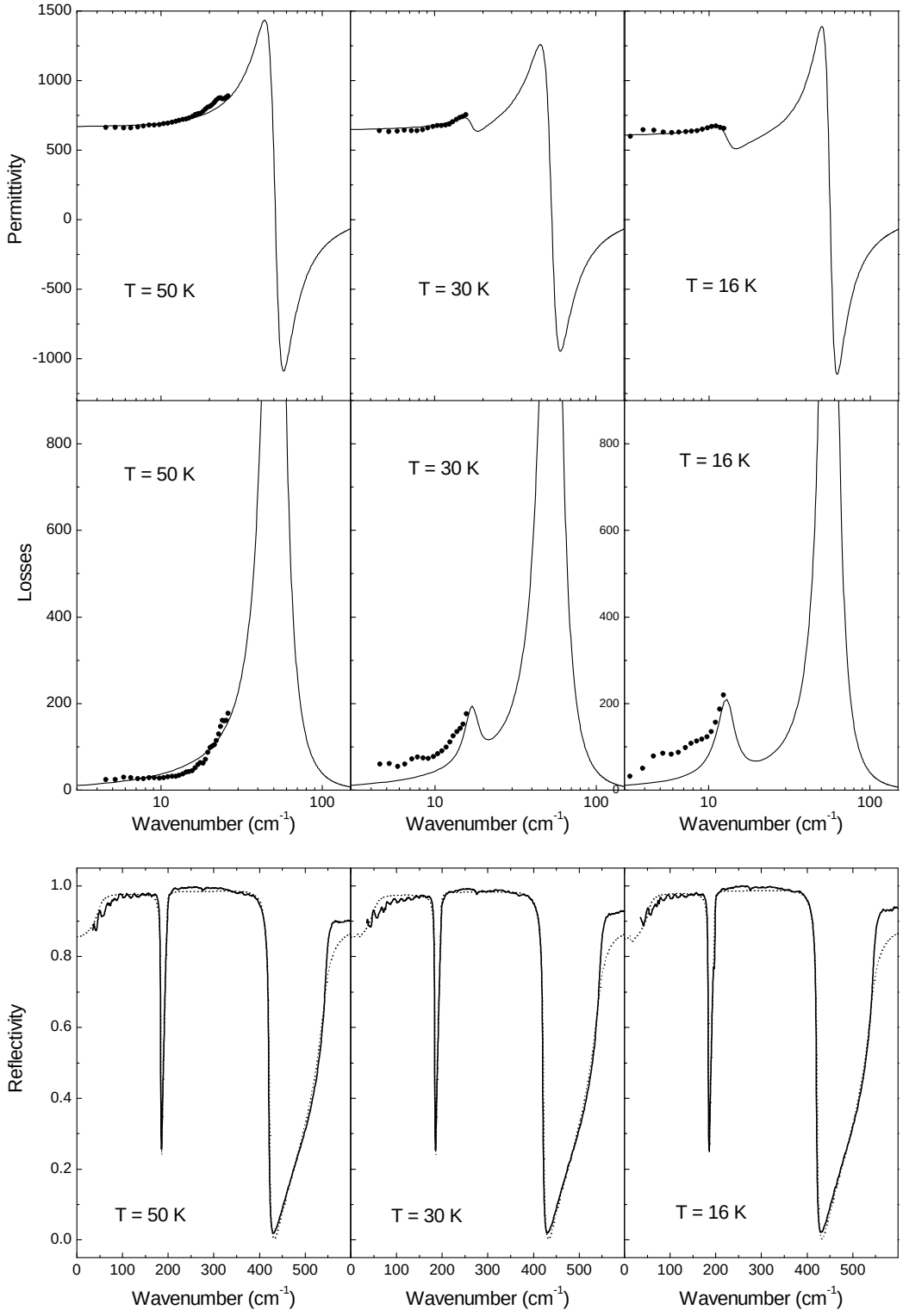

Figure 3.20: Measured THz permittivity and losses (points) and FTIR reflectivity solid lines for KLT with $x = 0.043$ at different temperatures. Fitting curves calculated using CME approach are shown by lines.

found by Azzini *et al.* [189] from SHG and birefringence measurements. Furthermore, the dielectric contribution of the acoustic resonance is expected to increase on cooling because the fraction of nano-domains (proportional to f) is increasing as it is found from the fitting of experimental data. However this increase is not linear because the piezoelectric constant and hence the dielectric contribution of the resonance depends on the value of polarization inside nano-domains. The polarization increases on cooling as it is seen from the increase of the soft mode splitting. Therefore the resonance peak is negligibly weak at 50 K because the piezoelectric effect is weak and the volume fraction of nano-domains is small.

Thus the assumption that the enhanced THz losses arise due to piezoelectric resonance in nano-domains is in agreement with our experimental observations.

Conclusion

In conclusion we summarize the results of far IR and THz spectroscopy of $K_{1-x}Li_xTaO_3$ system.

(i). Li doping of $KTaO_3$ does not change the number of IR-active phonon modes and the frequencies of hard TO_2 and TO_4 modes.

(ii). The soft mode frequency gradually stiffens with the increase of Li content.

(iii). The temperature behavior of the soft mode in KLT with $x = 0.016$ does not show any anomaly around the supposed glass transition. The soft mode frequency is in a good agreement with hyper-Raman data. FTIR reflectivity and THz permittivity spectra can be fitted by the standard factorized oscillator model.

(iv). THz spectra of complex permittivity of KLT with $x = 0.043$ demonstrate an anomalous increase of losses below the phase transition at ~ 65 K and a deviation of the effective soft mode frequency from the hyper-Raman and Raman data. The effective soft mode frequency can be obtained from the frequencies of A_1 and E soft mode components observed in hyper-Raman and Raman spectra using the approach based on Clausius-Mossotti equation. The enhanced losses are fitted with an additional oscillator mode which was assigned to piezoelectric resonance inside the polar clusters.

The qualitative picture of polar ordering in KLT crystals according to our investigation and previous publications of other authors [157, 189, 159, 192, 154] is the following.

In KLT with $x = 0.016$, the short range correlation of dipole moments related to off-center Li ions exists even above the freezing temperature T_f. This correlation persists down to 0 K changing its character from dynamic to quasi-static. The size of the correlated regions is small (several nanometers) so that the local polarization inside nano-clusters is small and does not lead to appreciable splitting of the soft mode. This is in agreement with experimental observations of Raman scattering.

In KLT with $x = 0.043$, a stepwise increase of dipolar correlation length occurs at the first order phase transition. However, due to the presence of random fields, the polar ordering does not extend over macroscopic distances. The ferroelectric nano-domains which appear below T_c have the size of tens of nanometers such that the Raman scattering is able to detect the soft mode splitting inside the domains, whereas

the effective dielectric response in the far IR range is defined by a mixing of both soft mode components. The total volume occupied by nano-domains just below T_c (at 50 K) constitutes only about 60% of the crystal volume. This volume corresponds to the regions with the strongest Li-Li interactions. Spontaneous nucleation of nano-domains continues on cooling below T_c and at 16 K the crystal consists of polarized regions only. The piezoelectric activity induced by spontaneous polarization inside nano-domains leads to resonance which is observed in the THz range. The strength of this resonance is increasing with the increase of number of nano-domains.

3.2.2 $KTa_{1-x}Nb_xO_3$ crystals

$KTa_{1-x}Nb_xO_3$ single crystals were grown in a similar way as KLT using spontaneous crystallization process. Two $KTa_{1-x}Nb_xO_3$ samples with Nb concentration $x = 0.018$ (provided by L. A. Boatner, Oak Ridge National Laboratory, USA) and $x = 0.022$ (provided by P. P. Syrnikov, Ioffe Physical-Technical Institute, St-Peterburg, Russia) were studied. The niobium concentration was checked by electron probe microanalysis and other analytical methods.

THz complex permittivity of KLN samples was measured by TDTTS. The samples were prepared for the measurements in the form of (100)-oriented plane-parallel plates. In view of the expected very high losses at low temperatures the samples were made as thin as possible having the thickness of 55 µm. A combined fitting of the IR reflectivity spectra along with the THz complex permittivity was performed using factorized oscillator model (Equation 1.29). Some results of THz complex permittivity measurements together with the fitting curves are presented in Figure 3.21. A satisfactory agreement is found all measured spectra. Both KTN samples were not transparent in the THz frequency range below 50 K down to liquid helium temperature. The permittivity increases on cooling as a result of the soft mode softening. Other two IR-active phonon modes TO_2 and TO_4 inherent to $KTaO_3$ are also seen in IR spectra of KTN and, similarly to KLT, their parameters only slightly differ from those of pure $KTaO_3$.

It should be stressed that no polar excitation similar to central peak is observed in KTN samples in the investigated temperature range (down to 50 K). This is in contrast to KLT samples where the mode assigned to the relaxational hopping of Li ions among off-center positions has been observed near the room temperature. Following the Debye theory of a relaxation [123] the dielectric strength of relaxation mode has to be proportional to the square of the dipole moment of a hopping ion in off-center positions. Based on this we can conclude that the effective dipole moment carried by off-centered Nb ions in KTN is appreciably smaller than the dipole moment of Li clusters in KLT. This agrees with theoretical and experimental predictions for impurity ions displacements in KLT [140, 136, 138] and KTN [142, 137] which state that Nb off-center shift is very small comparing to the shift of Li ions.

Additional evidence of the weak character of Nb ions relaxation in KTN far from T_c comes from the comparison of phonon contribution to the permittivity with the low frequency permittivity of the same sample taken from [176]. The results for $KTa_{1-x}Nb_xO_3$ with $x = 0.018$ are shown in Figure 3.22. One can see that within the experimental error there is no dielectric dispersion starting from the kHz range up to THz frequencies at temperatures above 60 K.

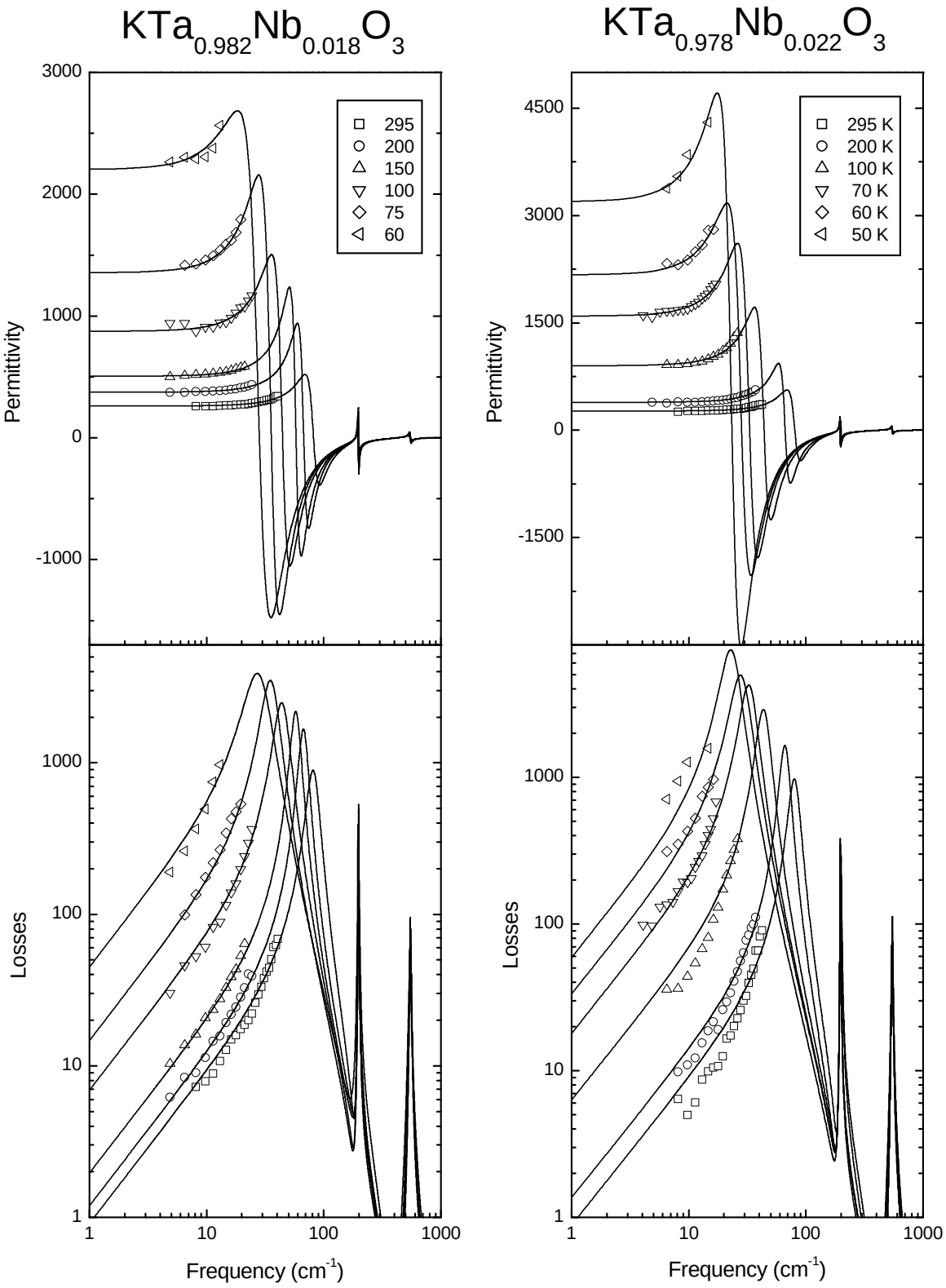

Figure 3.21: THz permittivity and losses in $KTa_{1-x}Nb_xO_3$ with $x = 0.018$ and 0.022. Solid lines are the fits by oscillator model.

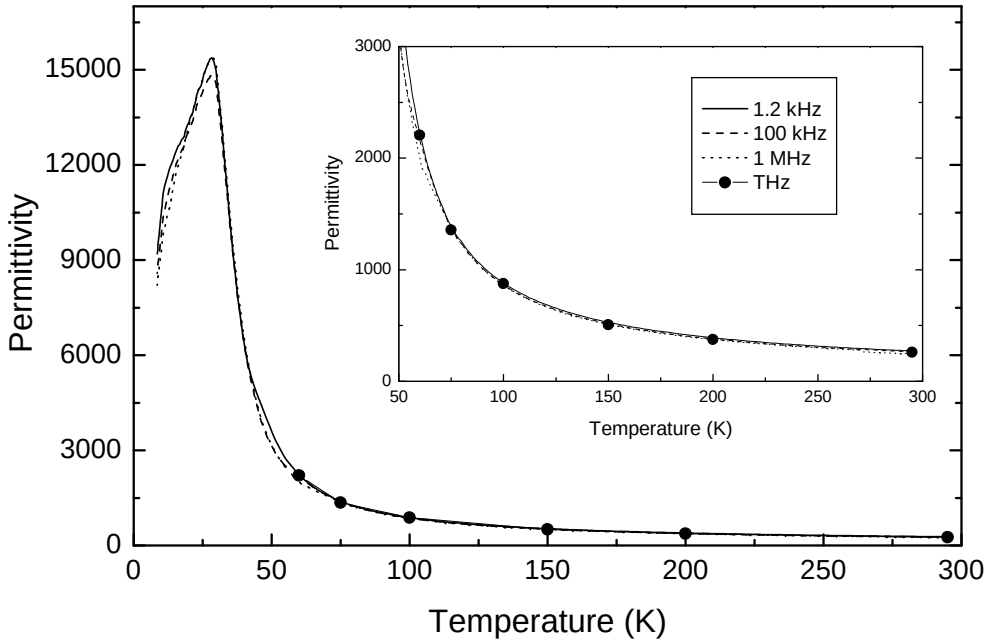

Figure 3.22: Low frequency permittivity as a function of temperature and the phonon contribution to permittivity found from the fits for $KTa_{1-x}Nb_xO_3$ with $x = 0.018$.

The soft mode frequency and damping constant as a function of temperature obtained from the fits is shown in Figure 3.23 for $KTa_{1-x}Nb_xO_3$ with $x = 0.018$ and 0.022 in comparison with the pure $KTaO_3$ and with hyper-Raman results of Kugel *et al.* [149] for $x = 0.02$. The Nb doping of $KTaO_3$ decreases the soft mode frequency and induces its critical slowing down in the vicinity of the phase transition temperature $T_c \simeq 27$ K. This behavior contrasts to that of the Li-doped samples where the soft mode stiffens upon doping and does not produce any temperature anomaly in the far IR response. Our results on the soft mode frequency are in good agreement with the hyper-Raman measurements for KTN with intermediate concentration $x = 0.02$. The damping constants extracted from the fits are higher than for pure $KTaO_3$ and are almost temperature independent but somewhat lower than those obtained from hyper-Raman measurements. The temperature dependence of the soft mode frequency for both investigated KTN crystals can be fitted by the Cochran law (see Figure 3.23). Deviations from this law are expected in the vicinity of T_c as predicted for quantum ferroelectrics (see Equation 3.13). Below the phase transition the samples remain opaque in IR. However, hyper-Raman [149], neutron and Raman scattering [150] experiments reveal the soft mode component which stiffens approximately according to the Cochran law with the proportionality constant renormalized according to thermodynamical mean-field theory [199] (see Figure 3.23). In the vicinity of T_c the soft mode behavior deviates from the Cochran law that leads to incomplete softening and the soft mode frequency is about 10 cm^{-1} at T_c as it was found in [150].

Let us discuss the reasons that make the investigated KTN samples opaque below the phase transition. It is seen in Figure 3.23 that at 10 K the soft mode frequency is of about 30 cm^{-1} as found by hyper-Raman scattering. For the underdamped soft mode TDTTS is able to detect the transmission signal even for lower soft mode frequencies. For example, in KTN with $x = 0.022$ at 50 K the found soft mode frequency and

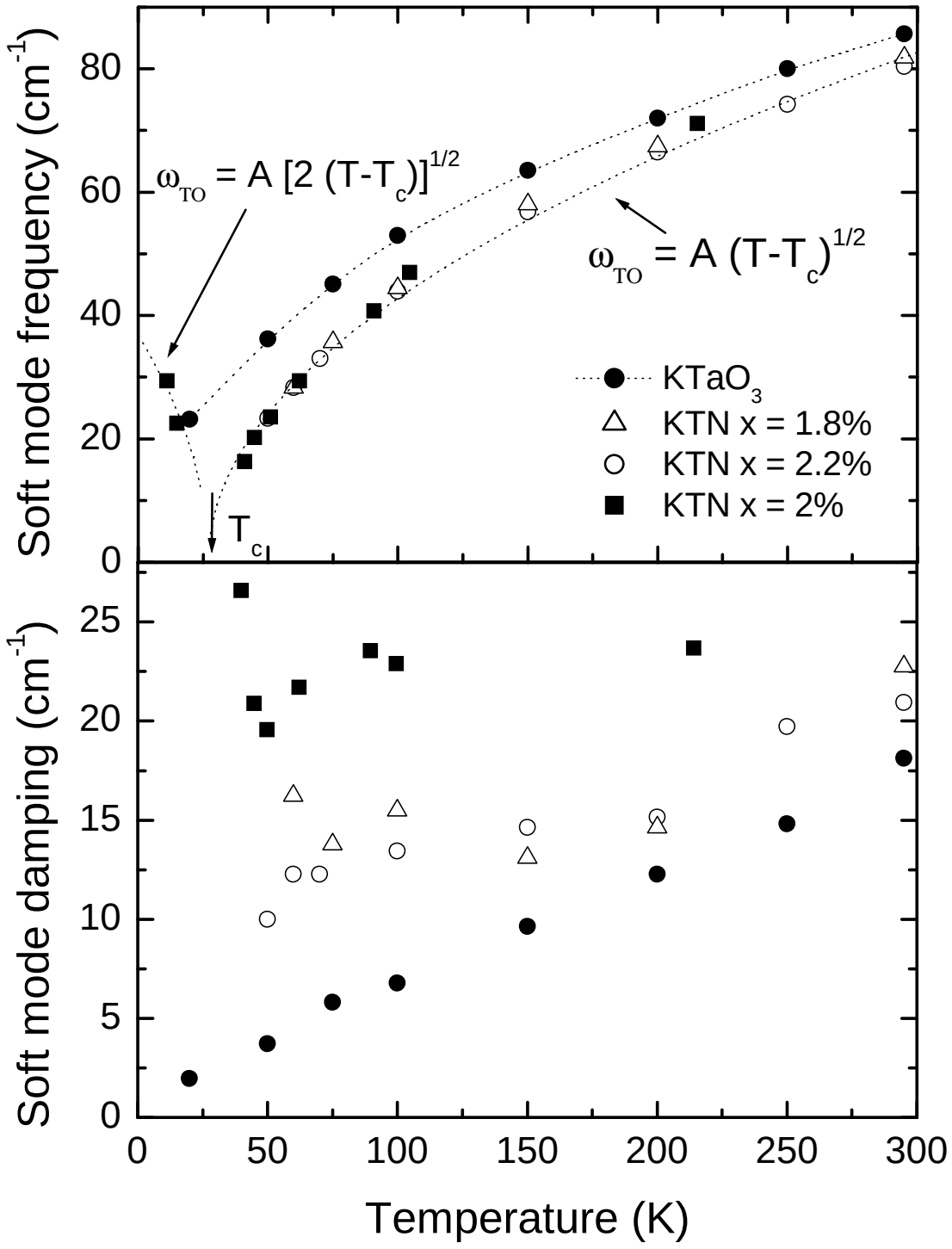

Figure 3.23: Frequency and damping constant of the soft mode in KTN and $KTaO_3$ as a function of temperature. Full squares correspond to hyper-Raman results taken from [149]. Line for KTN is approximate fit by the Cochran law ($T_c = 27$ K), line for $KTaO_3$ is guided by eye.

damping are 23.3 cm^{-1} and 10 cm^{-1}, respectively. Our estimation shows that the soft mode damping should be higher than 30 cm^{-1} at 10 K in order to make the sample less transparent than at 50 K. It seems that there is no reason for such increase of the damping constant at low temperatures (the soft mode damping below T_c is not reported in [149]). Moreover, the soft mode splitting measured by Raman spectroscopy below T_c (at 15 K) is rather small: 3 cm^{-1} for KTN with $x = 0.018$ [200] and 6.5 cm^{-1} for KTN with $x = 0.024$ [159]. Thus the effective soft mode frequency seen by IR spectroscopy would not be small enough to make KTN sample opaque for TDTTS.

Therefore we suggest that there is an additional mechanism of dielectric losses in the THz range which arises below T_c. In this respect the situation seems to be similar to the case of KLT where additional peak in losses has been found. However, we were able to observe it because the soft mode frequency in KLT samples is higher than in KTN, the measured KLT samples thus were not completely opaque at low temperatures. By analogy with KLT we suggest the same piezoelectric nature of additional losses in KTN. However, the size of polar regions in which the piezoelectric resonance takes place should be smaller than a few tens of nanometers: this is required by the values of the resonance frequency. In other words, this interpretation implies a short-range dipolar order in KTN below the phase transition. Recent dielectric and Raman study of the same KTN sample with $x = 0.018$ [200] supports this point of view. The physical picture proposed in this paper is the following. On cooling from the room temperature, the system behaves as a conventional displacive-type ferroelectric. However, the soft mode softens more in the regions enriched by Nb ions. Below T_c these regions, which have nanoscale size, acquire dipole moments. Their interaction leads to the freezing into glass-like state. This additional transition resembles the reentrant glass phase formation in $K_{1-x}Li_xTa_{1-y}Nb_yO_3$ proposed by the same group of authors [201]. Another evidence of the short-range order in KTN at liquid helium temperatures was found by Kleemann *et al.* [202] from the temperature measurements of refractive index and linear birefringence. For $KTa_{1-x}Nb_xO_3$ with $x = 0.02$ they found that about 80% of the polarization contribution to the change of refractive index is owing to the short-range polarization fluctuations and only 20% are due to the long-range order of polarization (note that the linear birefringence depends only on the long-range ordering).

In conclusion, far IR spectroscopy measurements on $KTa_{1-x}Nb_xO_3$ crystals with $x = 0.018$ and 0.022 above the phase transition temperature have demonstrated the critical softening of the soft mode following the Cochran law. The soft mode frequencies and damping constants extracted from the combined fits of FTIR reflectivity and TDTTS complex permittivity are in good agreement with previously published Raman and hyper-Raman data. The phonon contribution to the permittivity coincides with the permittivity measured in kHz frequency range indicating absence of noticeable dielectric dispersion below the IR range down to 50 K. Furthermore, no indication of the central peak related to Nb hopping among potential minima is observed in the THz spectra apart from T_c. Below 50 K, KTN samples become opaque due to high losses which persist down to liquid helium temperatures. Taking into account the fact that, at these temperatures, the soft mode hardens according to previously published experimental data [150, 149] we assume, similarly to the $K_{1-x}Li_xTaO_3$ system, an appearance of another polar excitation related to the piezoelectric resonance inside the polar nanoclusters.

3.2.3 $Sr_{1-1.5x}Bi_xTiO_3$ ceramics

Dielectric properties of $Sr_{1-1.5x}Bi_xTiO_3$ (SBiT-x) system were first investigated by Scanavi *et al.* [203]; recently this compound has attracted a lot of interest as a typical relaxor ferroelectric [135]. In contrast to $K_{1-x}Li_xTaO_3$ and $KTa_{1-x}Nb_xO_3$ systems, $Sr_{1-1.5x}Bi_xTiO_3$ is a solid solution in which the host lattice ions Sr^{2+} are substituted by aliovalent Bi^{3+} ions. According to Ref. [204], to satisfy the charge neutrality, one strontium vacancy V_{Sr} has to be created upon the substitution of tree divalent Sr^{2+} by two trivalent Bi^{3+}. Hence, the appropriate chemical formula should be written as $[Sr_{1-1.5x}(V_{Sr})_{0.5x}Bi_x]TiO_3$. Moreover, the situation in doped $SrTiO_3$ is more complicated comparing to the doped $KTaO_3$ because of the antiferrodistortive phase transition at 105 K which is accompanied by the doubling of $SrTiO_3$ unit cell [105]. Tetragonal symmetry of $SrTiO_3$ below the phase transition may lead to anisotropic character of the dipolar interaction between impurities. This was observed e.g. in $Sr_{1-x}Ca_xTiO_3$ system where the quantum ferroelectricity in the plane normal to the tetragonal axis was reported by Bednorz and Müller [145].

The origin of dielectric relaxation in $Sr_{1-1.5x}Bi_xTiO_3$ was initially attributed to the hopping of Ti^{4+} ions within the oxygen octahedra distorted by the proximity of Sr vacancies [204]. However this hypothesis is in conflict with recent dielectric measurements on $[Sr_{1-1.5x}(V_{Sr})_{0.5x}La_x]TiO_3$ ceramics [205] where the relaxation can be eliminated by a proper annealing. On the other hand, it was found that the lattice parameter of SBiT linearly increases as the content of Bi grows [206, 207]. Taking into account this fact together with the smaller ionic radius of Bi^{3+} ($r^{3+}_{Bi}/r^{2+}_{Sr} \approx 0.86$), Chen Ang *et al.* [135] suggested an off-centered position for Bi^{3+}. Thus, in analogy to $K_{1-x}Li_xTaO_3$, the off-centered Bi ions on A-site are responsible for the relaxor-type behavior of $Sr_{1-1.5x}Bi_xTiO_3$.

Only $Sr_{1-1.5x}Bi_xTiO_3$ ceramics which are not optically transparent have been studied up to now. This is probably related to difficulties of the crystal growth: SBiT is non-stoichiometric compound with a large number of vacancies. Therefore no optical measurements of refractive index, birefringence and SHG are available for SBiT. This is in contrast to KLT and KTN crystals where these methods allow the determination of the phase transition temperature with a high enough precision. The only optical experiment made on SBiT ceramics is Raman scattering [208, 209, 210]. The most prominent feature observed in these spectra is the presence of forbidden TO_2 and TO_4 modes whose intensity is progressively growing towards higher Bi-content and lower temperatures. Appearance of these polar modes proves the loss of the inversion center at least locally. A similar effect was observed in $K_{1-x}Li_xTaO_3$ [158]. It is also worth to notice that one of the R-point modes (at $\sim 140\,cm^{-1}$), which should become active below the antiferrodistortive phase transition in pure $SrTiO_3$ [155], can be observed up to the room temperature. This fact speaks for the simultaneous existence of impurity induced local antiferrodistortive and polar ordering. The splitting of the soft mode typical for KLT below the phase transition [192] was not resolved in SBiT down to 10 K [209] because of its high damping compared to the case of KLT crystals. The detailed determination of the soft mode frequency as a function of temperature is not possible by Raman spectroscopy because of the same reason. Therefore THz and FTIR spectroscopy seems to be the most simple and reliable method for investigation of phonon dynamics in SBiT ceramics.

Temperature behavior of the IR phonon modes

Six SBiT-x ceramic samples (x = 0; 0.0067; 0.0267; 0.08; 0.133; 0.167) were provided by P. Vilarinho (University of Aveiro, Portugal). The samples were prepared using conventional mixed oxide technology (initial reagents: $SrCO_3$, TiO_2 and Bi_2O_3), details of the synthesis and the microstructure characterization can be found elsewhere [207]. X-ray diffraction analysis of all studied SBiT samples has confirmed their cubic perovskite structure at room temperature. Thin plane-parallel platelets of 8 mm diameter and 75 and 130 µm thickness were used for TDTTS measurements, 2 mm or thicker plates with optically polished front side were used for BWO and FTIR reflectivity measurements. The obtained reflectivity spectra were normalized to the corresponding submillimeter reflectivity values calculated from the complex permittivity determined by TDTTS.

The normalized experimental reflectivity spectra were fitted together with the THz data by a factorized oscillator model (Equation 1.29); a classical three parameter overdamped oscillator term (Equation 1.28) has been also added in order to take into account the relaxational dispersion below the phonon frequencies. Results of the fit are shown in Figure 3.24 for SBiT-0 and SBiT-0.0267 ceramics. In the pure $SrTiO_3$ sample three transverse optic phonon modes TO_1 (soft mode), TO_2 (174 cm^{-1}) and TO_4 (545 cm^{-1}) are observed in the cubic phase above the antiferrodistortive phase transition ($T_a \simeq 130$ K was reported for ceramics [102]). Below the transition $SrTiO_3$ stabilizes in tetragonal phase (space group $I4/mcm$) and two additional modes appear in the IR spectra due to the Brillouin zone folding: an IR-active E_u mode at 435 cm^{-1} and a Raman-active E_g mode (denoted as X-mode) activated in IR due to the coupling with the soft mode which becomes possible in ceramics with frozen polarization at grain boundaries [102].

Bi-doping causes appreciable changes in far IR spectra of SBiT (see Figure 3.24b). The soft mode hardens with increasing Bi content and even for x = 0.0067 its frequency becomes higher than the X-mode frequency. Simultaneously, the X-mode frequency lowers by approximately 10 cm^{-1} comparing to the pure $SrTiO_3$ ceramic. This can be understood by the "repulsive" effect that shifts the observed frequencies of two coupled modes with respect to their bare (uncoupled) values. For the undoped ceramics, the soft mode lies below the E_g mode and the resulting X-mode frequency is shifted to higher values. In contrast, for SBiT samples the soft mode lies above the E_g mode and the X-mode frequency is expected to be lower than the bare frequency. Temperature dependencies of the X-mode and soft mode frequencies for all investigated SBiT samples are shown in Figure 3.25. One can see that for x = 0.08 the soft mode becomes almost temperature independent below the room temperature. Nevertheless its frequency hardens with the increase of bismuth content and reaches the level of 140 cm^{-1} for SBiT-0.167. The dependence of the square of the soft mode frequency on Bi-content is linear at all temperatures with a minor sublinear deviation for low (x < 0.02) concentrations of the dopant. As it was discussed above, a similar effect is observed for KLT and it is explained in terms of the frequency shift of an anharmonic oscillator biased by random electric fields produced by dipole impurities [148]. In the case of $Sr_{1-1.5x}Bi_xTiO_3$ the shift of the soft mode frequency is larger than for $K_{1-x}Li_xTaO_3$. This can be due to the additional internal fields produced by different valence of Bi^{3+} and Li^+ ions, Sr vacancies and by larger anharmonicity of $SrTiO_3$ lattice comparing to $KTaO_3$.

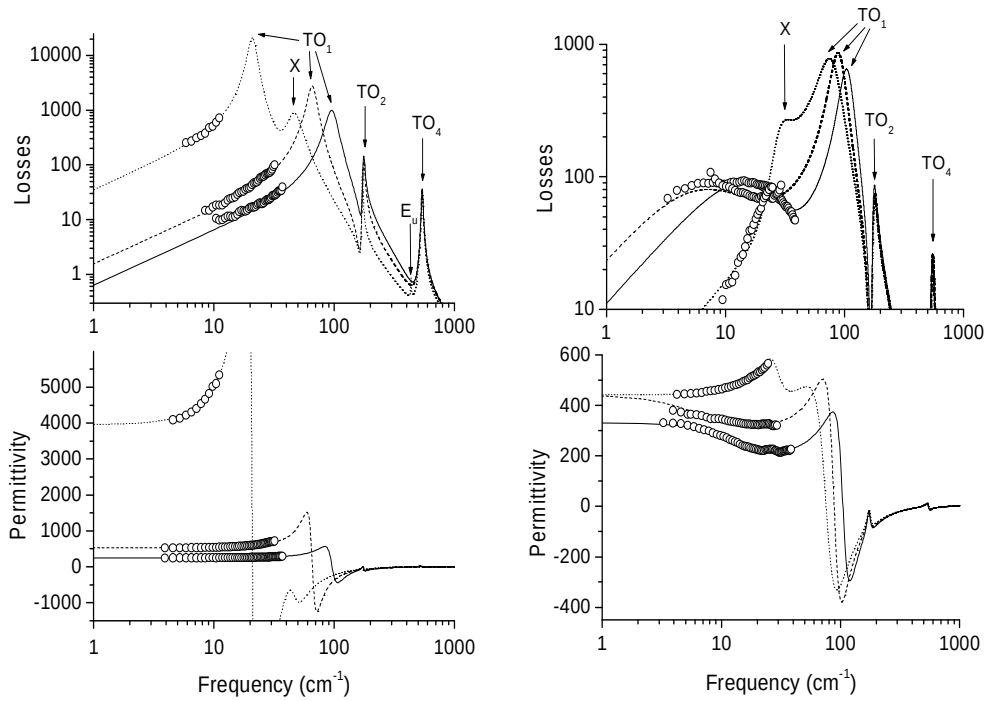

Figure 3.24: Submillimeter dielectric loss and permittivity (open circles) and IR fits at 295 K (solid line), 160 K (dashed line) and 20 K (dotted line) of pure $SrTiO_3$ (a) and SBiT-0.0267 (b).

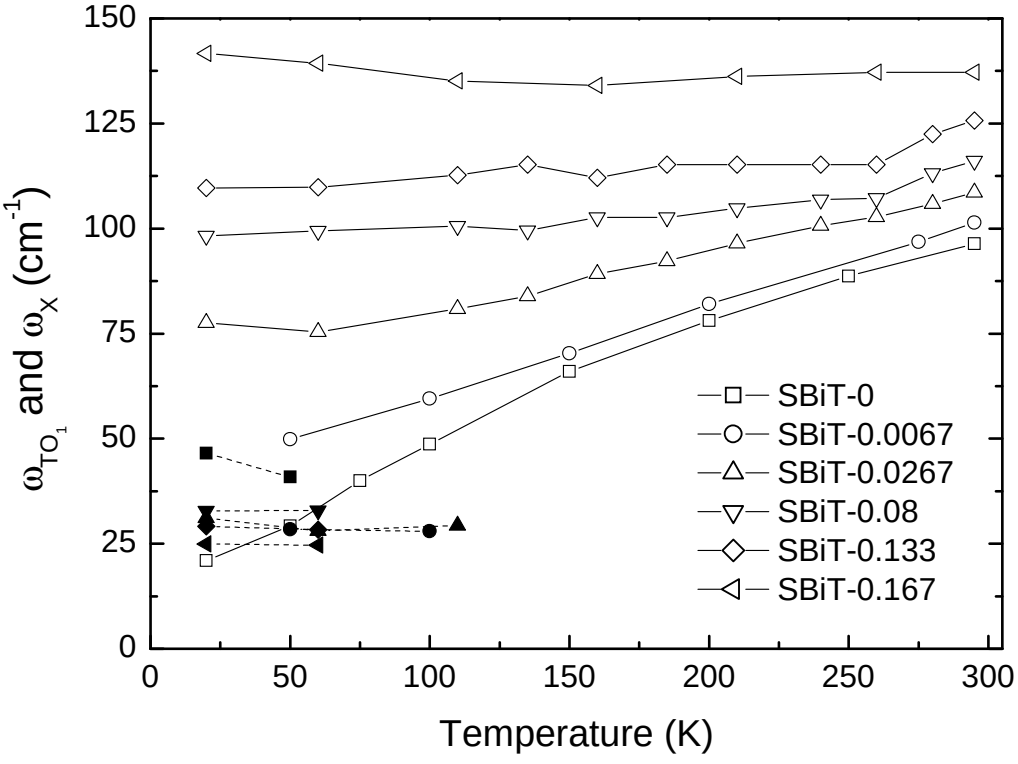

Figure 3.25: Temperature dependence of the soft mode TO1 (open symbols) and the X-mode (full symbols) frequencies in $Sr_{1-1.5x}Bi_xTiO_3$.

The X-mode frequency in SBiT does not depend on bismuth content within the experimental and fitting errors. On the other hand, the dielectric strength of X-mode distinctly decreases with the increase of bismuth content. Unfortunately, the precision of our fits was not high enough for a quantitative estimation of the coupling constant. From the qualitative point of view one can expect an increase of the coupling constant for higher doping by the off-center impurities such as bismuth that tends to distort local lattice symmetry. At the same time, the soft mode hardening induced by the doping diminishes the coupling effect and correspondingly the transfer of the effective charge from the soft TO_1 to the X-mode. The latter factor seems to be dominant in SBiT with $x > 0.0267$.

Relaxational dispersion in $Sr_{1-1.5x}Bi_xTiO_3$

Let us discuss now the relaxational dispersion in SBiT ceramics. It is well known that the dielectric relaxation in SBiT spans over a wide frequency range (especially at low temperatures) [211, 212]. However, it was not confirmed up to now whether the relaxation-like dispersion reaches millimeter and submillimeter range. Our measurements reveal this type of dispersion in all investigated SBiT samples [175].

The room temperature THz permittivity and losses of all samples are shown in Figure 3.26. In contrast to pure $SrTiO_3$, SBiT samples exhibit appreciably higher losses and a negative slope in the permittivity dispersion. The origin of this dispersion can be attributed to the relaxational hopping of individual (uncorrelated) bismuth ions between the off-center equilibrium positions as the fastest possible polarization process below the optic phonon frequencies. Dielectric losses of SBiT increase with doping for $x \leq 0.08$ and start to decrease above this level. This gives the evidence that at high concentration of Bi ($x > 0.08$) the interaction energy between Bi ions becomes higher than the energy of room temperature thermal fluctuations and most of ions are involved in slow polarization processes which do not contribute to submillimeter losses.

Quantitative analysis of these effects needs to include dielectric data in the MW frequency range. It has been performed by Porokhonskyy *et al.* [210]. In this work the complex permittivity spectra in a wide frequency range (100 Hz – 1.8 GHz) were fitted together with the THz permittivity and FTIR reflectivity data in the temperature range 100 – 300 K. Relaxational dispersion has been fitted using relaxation time distribution function (see Equation 3.7) where $g(\Omega)$ was chosen in the form of symmetrical trapezia. Moreover, the integrand in Equation 3.7 involved strongly overdamped oscillator term instead of Debye relaxation term in order to avoid drawbacks of Debye model in the high frequency limit (for details see [210]).

It was found that there are at least two processes contributing to the submillimeter losses and permittivity of SBiT. First one, denoted here as "process I", is a narrow (almost mono-Debye) relaxation located in the THz range at all studied temperatures. Second "process II" is broader and its center is located around 10 GHz. Its temperature behavior obeys the Arrhenius law which allows us to conclude that the process is thermally activated. Taking into account the fact that the dielectric strength of process II is proportional to Bi concentration in the sample, one can conclude that the process II is related to Bi ions hopping among the off-centered potential minima. Furthermore, the dielectric contribution of process II should correlate with the soft mode frequency. This behavior is expected because the effective dipole moment of

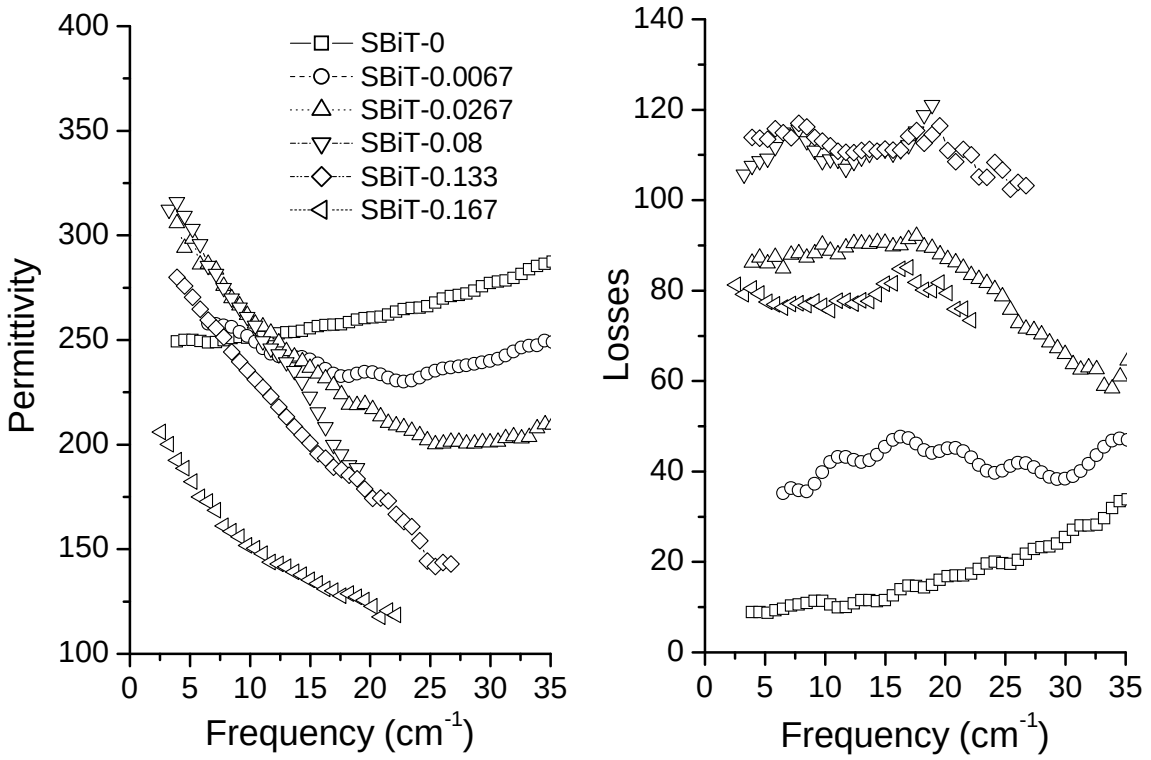

Figure 3.26: THz dielectric permittivity and losses of SBiT-x ceramics at room temperature.

impurity depends on dielectric constant of the lattice determined by the soft mode frequency.

Figure 3.27 shows the dielectric strength of process II normalized by Bi concentration as a function of the soft mode frequency. For low Bi concentrations (x = 0.67 and 2.67%) the dependence can be well fitted by a power law $\Delta\epsilon_{II}(T)/x \propto [\omega_{TO_1}(T)]^{-\gamma}$, where $\gamma = 8$. For higher dopant concentrations the soft mode depends on temperature rather weakly such that an accurate determination of γ is not possible.

Figure 3.27 gives evidence of interaction between dipolar Bi impurities and highly polarizable $SrTiO_3$ host lattice which enhances the effective dipole moment of relaxing dipoles. As it was shown, the effective dipole moment increases proportionally to permittivity of the host lattice (Equation 3.11). The dielectric contribution of electric dipoles in non-polar surrounding can be described by the Onsager model [213] which takes into account the long-range dipolar interactions. In the limit of high permittivities it writes

$$\Delta\epsilon_{II}(T) = \frac{(\epsilon_{ph}(T)+2)^2}{2}\frac{1}{3\epsilon_0}N\frac{d_0^2}{3kT}, \tag{3.26}$$

where d_0 is the internal dipole moment of impurities and N is their concentration. Taking into account LST relation (Equation 3.2) we obtain

$$\Delta\epsilon_{II}(T)/x \propto [\omega_{TO_1}(T)]^{-4}/T. \tag{3.27}$$

For the rough estimation we may consider $\epsilon_{ph}(T) \propto 1/T$ in the high temperature limit. Then the last equation gives $\Delta\epsilon_{II}(T)/x \propto [\omega_{TO_1}(T)]^{-6}$. Thus the exponent

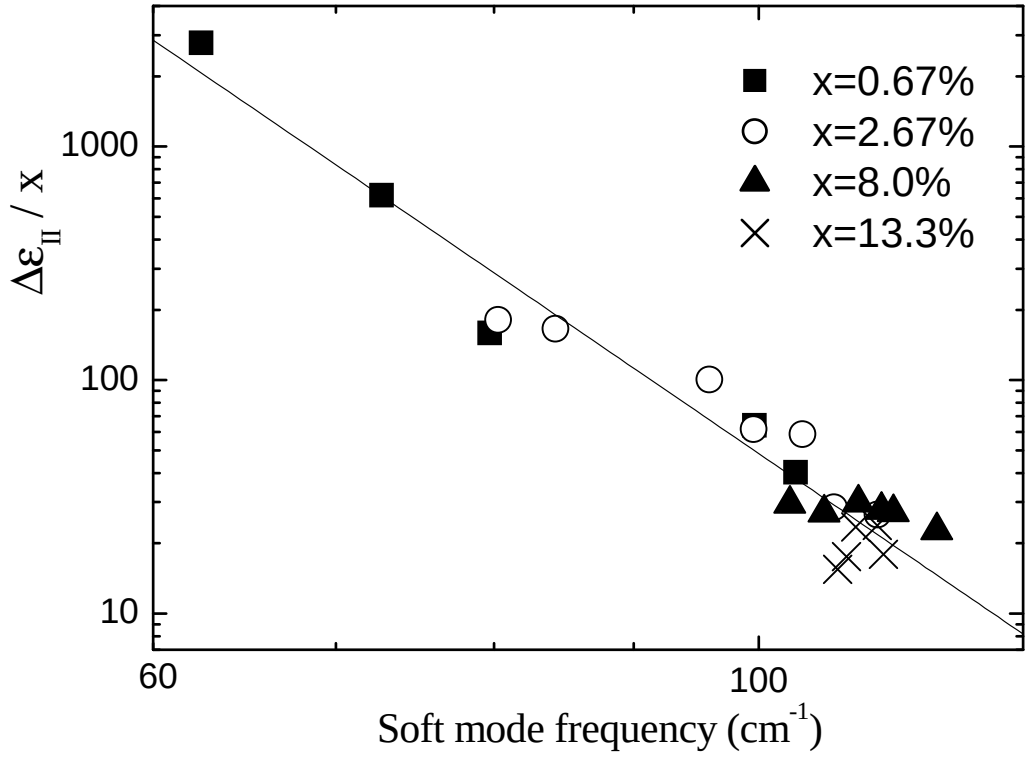

Figure 3.27: Dielectric strength of relaxation process II as a function of the soft mode frequency. Symbols are experimental data, solid line is the fit of the data by power law with exponent $\gamma = 8$.

$\gamma \simeq 6$ obtained in the framework of our simplified model is appreciably smaller than that observed in the experiment. Perhaps, a more detailed analysis which takes into account the short-range interactions between dipoles has to be performed. However, to the best of our knowledge, no theoretical model for the systems with random impurities which predicts $\gamma = 8$ has been elaborated so far.

The temperature independence of the characteristic frequency of process I indicates that the corresponding polarization mechanism is not related to a thermally activated hopping. It has been assigned to quasi-Debye losses which are activated due to the local breaking of the inversion symmetry (see Chapter 2.1). The characteristic frequency, which is not strongly temperature dependent, is then given by the mean damping of the thermally activated phonons. In agreement with the theory, the dielectric strength of process I vanishes at low temperatures.

In conclusion, the bismuth doping of $SrTiO_3$ ceramics leads to the hardening of the soft mode frequency and to the suppression of its temperature dependence. The frequencies of other IR active modes are almost independent on Bi content. The coupling of the soft mode with E_g symmetry Raman doublet in SBiT-x decreases due to the soft mode hardening for x $>$ 0.0267. An additional dielectric dispersion in the submillimeter range related to the thermally activated hopping of the off-center bismuth ions and quasi-Debye losses appears in all SBiT samples below the soft-mode frequency. $SrTiO_3$ host lattice polarized around Bi dipoles enhances the dielectric strength of thermally activated relaxation process. However the relation between the soft mode frequency and the strength of hopping process is not trivial and is described by a power law with the exponent $\gamma = 8$.

Conclusion

The main results of the present work are summarized below:

(i). A new approach to the time-domain THz reflection spectroscopy has been developed. It is able to provide in many cases an easy and accurate measurement of the phase of complex reflectance. In this way the complex THz permittivity of opaque samples and thin films can be measured. The corresponding experimental setup has been constructed and tested using different types of samples which were chosen to illustrate the potential applications of the method. The obtained results have confirmed the efficiency and reliability of the approach.

(ii). The analysis of intrinsic and extrinsic dielectric losses in several MW ceramics systems has been carried out. The conclusions for each ceramics system are the following:

(a) Far IR spectroscopic study of $Ba(Mg_{1/3}Ta_{2/3})O_3$ (BMT) ceramics has confirmed that Zr-doping during two-step mixed oxide process increases quality factor of BMT ceramics in THz range in agreement with the results of MW measurements. On the other hand, BMT ceramics prepared by alkoxide process are characterized by additional resonances in THz range due to the presence of secondary phase of unknown structure and have appreciably higher intrinsic losses than BMT ceramics prepared by mixed oxide technology.

(b) The poor quality factor of (1-x)$CaTiO_3$–x$Sr(Mg_{1/3}Nb_{2/3})O_3$ ceramics with $\tau_f \approx 0$ ($x \approx 0.8$) is mostly a consequence of extrinsic losses which may be eliminated by reducing the defect density in the ceramics. For $CaTiO_3$ ceramics moderately doped with $Sr(Mg_{1/3}Nb_{2/3})O_3$ the MW dielectric losses are rather close to the fitted intrinsic losses that indicates their high quality.

(c) The low quality factors of (1-x)$CaTiO_3$–x$Sr(Zn_{1/3}Nb_{2/3})O_3$ ceramics are mostly related to the fundamental (intrinsic) loss mechanisms. In contrast to $CaTiO_3$–$Sr(Mg_{1/3}Nb_{2/3})O_3$ ceramics there is no technological way to achieve appreciably higher quality of investigated $CaTiO_3$–$Sr(Zn_{1/3}Nb_{2/3})O_3$ ceramics.

(d) The MW losses of (1-x)$CaTiO_3$–x$LaGaO_3$ ceramics are mostly determined by intrinsic losses except pure $LaGaO_3$ and compositions with $x \leq 0.25$ where pronounced contribution of extrinsic losses is seen. Comparison of dielectric losses for ceramic and crystalline forms of $LaGaO_3$ shows that the approach for estimation of intrinsic losses by extrapolation of oscillator model down to MW range gives reasonable results.

(e) Extrapolation of the oscillator model fails in the case of (1-x)$CaTiO_3$–x$NdAlO_3$. The only conclusion we can make from comparison of submillimeter and MW losses is the absence of appreciable extrinsic losses for $0.125 \leq x \leq 0.75$. Pure $NdAlO_3$ sample and (1-x)$CaTiO_3$–x$NdAlO_3$ with x = 0.875 have extrinsic losses which are due to lower sample quality. Thus $CaTiO_3$–$NdAlO_3$ ceramics with compositions close to the point of temperature stability ($x \approx 0.44$) can be considered as promising materials for MW applications.

(f) Quality factor and dielectric constant of CeO_2 ceramics are improved by the addition of 1 mol% $CaCO_3$, but they deteriorate as the Ca^{2+} content further increases. The addition of TiO_2 essentially decreases the quality factor of CeO_2. Two sources of extrinsic losses (thermal relaxation and quasi-Debye loss) were found in pure ceria, however, the former loss mechanism (thermal relaxation of the defects) is suppressed by doping with 1 mol% of $CaCO_3$ which indicates a possibility of improvement of the CeO_2 ceramics quality factor by Ca^{2+} doping.

(iii). Far IR and THz dielectric response of three different doped incipient ferroelectric systems $K_{1-x}Li_xTaO_3$ (KLT), $KTa_{1-x}Nb_xO_3$ (KTN) and $Sr_{1-1.5x}Bi_xTiO_3$ (SBiT) have been studied. It has been found that the temperature behavior of the soft mode frequency is strongly dependent on the position of impurity ions in the host perovskite lattice. Li^+ and Bi^{3+} ions which occupy off-center position on the A-site of $KTaO_3$ and $SrTiO_3$, respectively, stiffen the soft mode frequency and do not induce any temperature anomaly in its behavior. It seems that this effect is induced by the random electric fields produced by the dipole moments of the off-centered ions.

Nb^{5+} ions which substitute Ta^{5+} on the B-site of $KTaO_3$ are involved in the soft mode vibrations and cause a decrease of its frequency compared to pure $KTaO_3$. In addition, a temperature anomaly in the soft mode behavior is observed for sufficiently large concentration of Nb ($x > x_c = 0.008$). At temperatures well above the transition temperature the softening follows the Cochran law like in typical ferroelectrics with displacive phase transition. On approaching T_c the soft mode couples to the relaxation mode of polar clusters; this leads to the rise of central peak which is mostly responsible for the permittivity near the transition point.

The relation between the dynamics of polar regions and the soft mode behavior in doped incipient ferroelectrics is different for different kinds of dopants. In KLT and SBiT local dipole moments of polar clusters stiffen the soft mode frequency at high temperatures. In this case the cooperative dynamics of the clusters leads to order-disorder type transition on cooling and the spontaneous polarization inside nanodomains induces a splitting of the soft mode. On the other hand, in KTN at high temperatures the influence of polar clusters is negligibly small and the soft mode is dominant. The polar clusters become dominant on cooling, close to T_c and below it, due to the coupling with the soft mode.

Bibliography

[1] G. Grüner, ed. *Millimeter and Submillimeter Wave Spectroscopy of Solids*. Springer-Verlag, Berlin, Heidelberg (1998).

[2] T. Kakeshita, S. Uchida, K. M. Kojima, S. Adachi, S. Tajima, B. Gorshunov, and M. Dressel. Transverse Josephson Plasma Mode in T* Cuprate Superconductors. *Phys. Rev. Lett.* **86**, 4140 (2001).

[3] P. Kužel and J. Petzelt. Time-resolved terahertz transmission spectroscopy of dielectrics. *Ferroelectrics* **239** (1–4), 949–956 (2000).

[4] M. van Exter and D. Grischkowsky. Optical and Electronic Properties of Doped Silicon from 0.1 to 2 THz. *Appl. Phys. Lett.* **56** (17), 1694–1696 (1990).

[5] M. C. Nuss, P. M. Mankiewich, M. L. O'Malley, and E. H. Westerwick. Dynamic conductivity and "coherence peak" in $YBa_2Cu_3O_7$ superconductors. *Phys. Rev. Lett.* **66** (25), 3305–3308 (1991).

[6] T.-I. Jeon, D. Grischkowsky, A. K. Mukherjee, and R. Menon. Electrical characterization of conducting polypyrrole by THz time-domain spectroscopy. *Appl. Phys. Lett.* **77** (16), 2452–2454 (2000).

[7] P. Gu, F. Chang, M. Tani, K. Sakai, and C. L. Pan. Generation of Coherent Cw-Terahertz Radiation Using Tunable-Dual Wavelength External Cavity Laser Diode. *Jpn. J. of Appl. Phys.* **38**, L1246 (1999).

[8] G. Kozlov, ed. *Submillimeter Dielectric Spectroscopy of Solids*, vol. 25 of *Proc. Inst. General Phys.* Nauka, Moscow (1990). In Russian.

[9] M. Born and E. Wolf. *Principles of Optics*. Pergamon, Oxford (1970).

[10] C. Rullière, ed. *Femtosecond Laser Pulses: Principles and Experiments*. Springer-Verlag, Berlin Heidelberg (1998).

[11] M. Pessot, P. Maine, and G. Mourou. 1000 Times Expansion/Compression of Optical Pulses for Chirped Pulse Amplification. *Opt. Commun.* **62**, 419–421 (1987).

[12] D. H. Auston, K. P. Cheung, and P. R. Smith. Picosecond photoconducting Hertzian dipoles. *Appl. Phys. Lett.* **45** (3), 284–286 (1984).

[13] F. E. Doany, D. Grischkowsky, and C.-C. Chi. Carrier Lifetime versus Ion-Implantation Dose in Silicon on Sapphire. *Appl. Phys. Lett.* **50**, 460 (1987).

[14] H. Němec, A. Pashkin, P. Kužel, M. Khazan, S. Schnüll, and I. Wilke. Carrier dynamics in low-temperature grown GaAs studied by terahertz emission spectroscopy. *J. Appl. Phys.* **90** (3), 1303–1306 (2001).

[15] C. Fattinger and D. Grischkowsky. Point source terahertz optics. *Appl. Phys. Lett.* **53** (16), 1480–1482 (1988).

[16] B. B. Hu, J. T. Darrow, X.-C. Zhang, D. H. Auston, and P. R. Smith. Optically Steerable Photoconducting Antennas. *Appl. Phys. Lett.* **56**, 886–888 (1990).

[17] D. You, R. R. Jones, P. H. Bucksbaum, and D. R. Dykaar. Generation of High-Power Sub-Single-Cycle 500-Fs Electromagnetic Pulses. *Opt. Lett.* **18**, 290 (1993).

[18] K. H. Yang, P. L. Richards, and Y. R. Shen. Generation of Far-Infrared Radiation by Picosecond Light Pulses. *Appl. Phys. Lett.* **19**, 320–323 (1971).

[19] L. Xu, X. C. Zhang, and D. H. Auston. Terahertz beam generation by femtosecond optical pulses in electrooptic materials. *Appl. Phys. Lett.* **61** (15), 1784–1786 (1992).

[20] A. Leitenstorfer, S. Hunsche, J. Shah, M. C. Nuss, and W. H. Knox. Detectors and sources for ultrabroadband electro-optic sampling: Experiment and theory. *Appl. Phys. Lett.* **74** (11), 1516–1518 (1999).

[21] A. Nahata, A. S. Weling, and T. F. Heinz. A wideband coherent terahertz spectroscopy system using optical rectification and electro-optic sampling. *Appl. Phys. Lett.* **69** (16), 2321–2323 (1996).

[22] X.-C. Zhang, Y. Jin, K. Yang, and L. J. Schowalter. Resonant nonlinear susceptibility near the GaAs band gap. *Phys. Rev. Lett.* **69** (15), 2303–2306 (1992).

[23] A. Rice, Y. Jin, X. F. Ma, , X.-C. Zhang, D. Bliss, J. Larkin, and M. Alexander. Terahertz optical rectification from $\langle 110 \rangle$ zinc-blende crystals. *Appl. Phys. Lett.* **64** (11), 1324–1326 (1994).

[24] X.-C. Zhang, X. F. Ma, Y. Jin, T.-M. Lu, E. P. Boden, P. D. Phelps, K. R. Stewart, and C. P. Yakymyshyn. Terahertz optical rectification from a nonlinear organic crystal. *Appl. Phys. Lett.* **61** (26), 3080–3082 (1992).

[25] H. Hashimoto, H. Takahashi, T. Yamada, K. Kuroyanagi, and T. Kobayashi. Characteristics of the terahertz radiation from single crystals of *N*-substituted 2-methyl-4-nitroaniline. *J. Phys.: Condens. Matter* **13** (23), 529–537 (2001).

[26] P. R. Smith, D. H. Auston, and M. C. Nuss. Subpicosecond photoconducting dipole antennas. *IEEE J. of Quantum Electron.* **24** (2), 255–260 (1988).

[27] Q. Wu and X.-C. Zhang. Free-space electro-optic sampling of terahertz beams. *Appl. Phys. Lett.* **67** (24), 3523–3525 (1995).

[28] Z. Jiang, F. G. Sun, Q. Chen, and X.-C. Zhang. Electro-optic sampling near zero optical transmission point. *Appl. Phys. Lett.* **74** (9), 1191–1193 (1999).

[29] Q. Wu, M. Litz, and X.-C. Zhang. Broadband detection capability of ZnTe electro-optic field detectors. *Appl. Phys. Lett.* **68** (21), 2924–2926 (1996).

[30] H. J. Bakker, G. C. Cho, H. Kurz, Q. Wu, and X.-C. Zhang. Distortion of terahertz pulses in electro-optic sampling. *J. Opt. Soc. Am. B* **15** (6), 1795–1801 (1998).

[31] M. Schall and P. U. Jepsen. Freeze-out of difference-phonon modes in ZnTe and its application in detection of THz pulses. *Appl. Phys. Lett.* **77** (18), 2801–2803 (2000).

[32] Q. Wu and X.-C. Zhang. 7 terahertz broadband GaP electro-optic sensor. *Appl. Phys. Lett.* **70** (14), 1784–1786 (1997).

[33] P. Y. Han, , M. Tani, F. Pan, and X.-C. Zhang. Use of the organic crystal DAST for terahertz beam applications. *Opt. Lett.* **25** (9), 675–677 (2000).

[34] M. van Exter, C. Fattinger, and D. Grischkowsky. Terahertz time-domain spectroscopy of water-vapor. *Opt. Lett.* **14** (20), 1128–1130 (1989).

[35] P. Kužel, M. A. Khazan, and J. Kroupa. Spatiotemporal transformations of ultrashort terahertz pulses. *J. Opt. Soc. Am. B* **16** (10), 1795–1800 (1999).

[36] H. Němec, F. Kadlec, and P. Kužel. Methodology of an Optical Pump-Terahertz Probe Experiment: An Analytical Frequency-Domain Approach. *J. Chem. Phys.* **117**, 8454–8466 (2002).

[37] C. F. Klingshirn. *Semiconductor Optics*. Springer-Verlag, Berlin Heidelberg (1995).

[38] F. Kadlec, J. Petzelt, V. Železný, and A. A. Volkov. Disappearance of the Infrared Soft Mode in the Weak Ferroelectric $Li_2Ge_7O_{15}$. *Solid State Commun.* **94**, 725–729 (1995).

[39] A. Pashkin, E. Buixaderas, P. Kužel, M.-H. Liang, C.-T. Hu, and I.-N. Lin. THz transmission spectroscopy applied to dielectrics and microwave ceramics. *Ferroelectrics* **254**, 113–120 (2001).

[40] J. Petzelt, P. Kužel, I. Rychetský, A. Pashkin, and T. Ostapchuk. Dielectric Response of Soft Modes in Ferroelectric Thin Films. *Ferroelectrics* **288**, 169–185 (2003).

[41] A. Pashkin, P. Kužel, J. Petzelt, B. Gorshunov, and M. Dressel. Time-Resolved and Backward-Wave Oscillator Submillimetre Spectroscopy of some Ferroelectric Ceramics and Thin Films. *Ferroelectrics* **272**, 219–224 (2002).

[42] S. C. Howells and L. A. Schlie. Transient Terahertz Reflection Spectroscopy of Undoped InSb from 0.1 to 1.1 THz. *Appl. Phys. Lett.* **69**, 550 (1996).

[43] L. Thrane, R. H. Jacobsen, P. U. Jepsen, and S. R. Keiding. THz Reflection Spectroscopy of Liquid Water. *Chem. Phys. Lett.* **240**, 330 (1995).

[44] M. Khazan, R. Meissner, and I. Wilke. Convertible Transmission-Reflection Time-Domain Terahertz Spectrometer. *Review of Scientific Instruments* **72**, 3427 (2001).

[45] T. Nagashima and M. Hangyo. Measurement of Complex Optical Constants of a Highly Doped Si Wafer Using Terahertz Ellipsometry. *Appl. Phys. Lett.* **79**, 3917 (2001).

[46] T.-I. Jeon and D. Grischkowsky. Characterization of Optically Dense, Doped Semiconductors by Reflection THz Time Domain Spectroscopy. *Appl. Phys. Lett.* **72**, 3032 (1998).

[47] S. Nashima, O. Morikawa, K. Takata, and M. Hangyo. Measurement of Optical Properties of Highly Doped Silicon by Terahertz Time Domain Reflection Spectroscopy. *Appl. Phys. Lett.* **79**, 3923 (2001).

[48] D. Hashimshony, I. Geltner, G. Cohen, Y. Avitzour, A. Zigler, and C. Smith. Characterization of the Electrical Properties and Thickness of Thin Epitaxial Semiconductor Layers by THz Reflection Spectroscopy. *J. Appl. Phys.* **90**, 5778 (2001).

[49] A. Pashkin, M. Kempa, H. Němec, F. Kadlec, and P. Kužel. Phase-Sensitive Time-Domain Terahertz Reflection Spectroscopy. *Rev. Sci. Instrum.* **74**, 4711–4717 (2003).

[50] C. A. Paz de Araujo, J. E. Cuchiaro, L. D. McMillan, M. C. Scott, and J. F. Scott. Fatigue-Free Ferroelectric Capacitors with Platinum Electrodes. *Nature* **374**, 627–629 (1995).

[51] S. Kamba, J. Pokorný, V. Porokhonskyy, J. Petzelt, M. P. Moret, A. Garg, Z. H. Barber, and R. Zallen. Ferroelastic Phase in $SrBi_2Ta_2O_9$ and Study of the Ferroelectric Phase-Transition Dynamics. *Appl. Phys. Lett.* **81**, 1056 (2002).

[52] D. W. Berreman. Infrared Absorption at Logitudinal Optic Frequency in Cubic Crystal Films. *Phys. Rev.* **130**, 2193 (1963).

[53] P. Y. Han, M. Tani, M. Usami, S. Kono, R. Kersting, and X.-C. Zhang. A Direct Comparison Between Terahertz Time-Domain Spectroscopy and Far-Infrared Fourier Transform Spectroscopy. *J. Appl. Phys.* **89**, 2357–2359 (2001).

[54] F. Gervais. *Infrared and Millimetre Waves*, vol. 8. Academic Press, New York (1983).

[55] J. Petzelt, S. Kamba, G. V. Kozlov, and A. A. Volkov. Dielectric Properties of Microwave Ceramics Investigated by Infrared and Submillimetre Spectroscopy. *Ferroelectrics* 145–165 (1996).

[56] J. Petzelt, R. Zurmühlen, A. Bell, S. Kamba, G. V. Kozlov, A. A. Volkov, and N. Setter. Dielectric Spectroscopy of some $Ba(B'_{1/2}B''_{1/2})O_3$ Complex Perovskites in the $10^{11} - 10^{14}$ Hz Range. *Ferroelectrics* **133**, 205–210 (1992).

[57] V. L. Gurevich and A. K. Tagantsev. Intrinsic Dielectric Loss in Crystals. *Adv. Phys.* **40**, 719–767 (1991).

[58] A. K. Tagantsev, J. Petzelt, and N. Setter. Relation Between Intrinsic Microwave and Submillimeter Losses and Permittivity in Dielectrics. *Solid State Commun.* **87**, 1117–1120 (1993).

[59] G. J. Coombs and R. A. Cowley. Paraelectric, Piezoelectric and Pyroelectric Crystals: I. Dielectric Properties. *J .Phys. C* **6**, 121–142 (1973).

[60] S. Kamba, J. .Petzelt, E. Buixaderas, D. Haubrich, P. Vaněk, P. Kužel, I. N. Jawahar, M. T. Sebastian, and P. Mohanan. High Frequency Dielectric Properties of $A_5B_4O_{15}$ Microwave Ceramics. *J. Appl. Phys.* **89**, 3900–3906 (2001).

[61] E. Schlömann. Dielectric Losses in Ionic Crystals with Disordered Charge Distributions. *Phys. Rev.* **135**, A413–A419 (1964).

[62] R. Zurmühlen, J. Petzelt, S. Kamba, G. Kozlov, A. Volkov, B. Gorshunov, D. Dube, A. Tagantsev, and N. Setter. Dielectric Spectroscopy of $Ba(B'_{1/2}B''_{1/2})O_3$ Complex Perovskite Ceramics: Correlations Between Ionic Parameters and Microwave Dielectric Properties. II. Studies Below the Phonon Eigenfrequencies ($10^2 - 10^{12}$ Hz). *J. Appl. Phys.* **77**, 5351–5364 (1995).

[63] W. Wersing. *High Frequency Ceramic Dielectrics and their Applications for Microwave Components: Electronic Ceramics.* Elsevier, London (1991).

[64] M.-H. Liang, C.-T. Hu, C.-G.Chiou, Y.-N. Tsai, and I.-N. Lin. Effect of $Ba_5Ta_4O_{15}$ Incorporation on Sintering Behavior and Microwave Dielectric Properties of $Ba(Mg_{1/3}Ta_{2/3})O_3$ Materials. *Jpn. J. Appl. Phys.* **38**, 5621–5624 (1999).

[65] S. Nomura, K. Toyama, and K. Kaneta. $Ba(Mg_{1/3}Ta_{2/3})O_3$ Ceramics with Temperature-Stable High Dielectric Constant and Low Microwave Loss. *Jpn. J. Appl. Phys.* **21**, 624–626 (1982).

[66] J. Petzelt and N. Setter. Far Infrared Spectroscopy and Origin of Microwave Losses in Low-Loss Ceramics. *Ferroelectrics* **150**, 89–102 (1993).

[67] T. Shimada. Dielectric Loss and Damping Constants of Lattice Vibrations in $Ba(Mg_{1/3}Ta_{2/3})O_3$ Ceramics. *J. Eur. Ceram. Soc.* **23**, 2647–2651 (2003).

[68] I.-N. Lin, M.-H. Liang, C.-T. Hu, and J. Steeds. Effect of $Ba_5Ta_4O_{15}$ on Microstructural Characteristics of $Ba(Mg_{1/3}Ta_{2/3})O_3$ Ceramics and their Microwave Dielectric Properties. *J. Eur. Ceram. Soc.* **21**, 1705–1709 (2001).

[69] M.-H. Liang, C.-T. Hu, H.-F. Cheng, I.-N. Lin, and J. Steeds. Effect of Sintering Process on Microstructural Characteristics of $Ba(Mg_{1/3}Ta_{2/3})O_3$ Ceramics and their Microwave Dielectric Properties. *J. Eur. Ceram. Soc.* **21**, 2759–2763 (2001).

[70] W.-A. Lan, M.-H. Liang, C.-T. Hu, K.-S. Liu, and I.-N. Lin. Influence of Zr-Doping on the Microstructure and Microwave Dielectric Properties of $Ba(Mg_{1/3}Ta_{2/3})O_3$ Materials. *Mater. Chem. Phys.* **79**, 266–269 (2003).

[71] C.-C. Chou, D.-S. Tsai, I.-N. Lin, and J. Steeds. Microstructural Defects in $Ba(Mg_{1/3}Ta_{2/3})O_3$ Microwave Dielectric Materials. *Mater. Chem. Phys.* **79**, 218–221 (2003).

[72] H.-J. Youn, K.-Y. Kim, and H. Kim. Microstructural Characteristics of $Ba(Mg_{1/3}Ta_{2/3})O_3$ Ceramics and its Related Microwave Dielectric Properties. *Jpn. J. Appl. Phys.* **35**, 3947–3953 (1996).

[73] T.-R. Tsai, M.-H. Liang, C.-T. Hu, C.-C. Chi, and I.-N. Lin. Terahertz Response of Bulk $Ba(Mg_{1/3}Ta_{2/3})O_3$. *Jpn. J. Appl. Phys.* **39**, 5642–5644 (2000).

[74] I.-N. Lin, C.-T. Chia, H.-L. Liu, Y.-C. Chen, H.-F. Cheng, and C.-C. Chi. High Frequency Dielectric Properties of $Ba(Mg_{1/3}Ta_{2/3})O_3$ Complex Perovskite Ceramics. *J. Eur. Ceram. Soc.* **23**, 2633–2637 (2003).

[75] T.-R. Tsai, C.-C. Chi, M.-H. Liang, C.-T. Hu, and I.-N. Lin. Dielectric Properties of (X)$Ba(Mg_{1/3}Ta_{2/3})O_3$-(1 - X)$Ba(Mg_{1/3}Nb_{2/3})O_3$ (X = 1, 0.75, 0.50, 0.25 and 0) Complex Perovskite Ceramics. *Mater. Chem. Phys.* **79**, 169–174 (2003).

[76] M.-H. Liang, S.-Y. Wu, C.-T. Hu, and I.-N. Lin. Enhancing the Sinterability of $Ba(Mg_{1/3}Ta_{2/3})O_3$ Dielectrics by Using Chemically-Derived Powders. *Mater. Chem. Phys.* **79**, 276–281 (2003).

[77] H. Tamura, D. A. Sagala, and K. Wakino. Lattice Vibrations of $Ba(Zn_{1/3}Ta_{2/3})O_3$ Crystal with Ordered Perovskite Structure. *Jpn. J. Appl. Phys.* **25**, 787–791 (1986).

[78] S. Nomura. Ceramics for Microwave Dielectric Resonator. *Ferroelectrics* **49**, 61–70 (1983).

[79] H. Zheng, G. D. C. Csete de Györgyfalva, R. Quimby, H. Bagshaw, R. Ubic, I. M. Reaney, and J. Yarwood. Raman Spectroscopy of B-site Order-Disorder in $CaTiO_3$-Based Microwave Ceramics. *J. Eur. Ceram. Soc.* **23**, 2653–2659 (2003).

[80] H. Bagshaw, D. Iddles, R. Quimby, and I. M. Reaney. Structure-Property Relations in x$CaTiO_3$-(1-x)$Sr(Mg_{1/3}Nb_{2/3})O_3$ Based Microwave Dielectrics. *J. Eur. Ceram. Soc.* **23**, 2435–2441 (2003).

[81] H. Zheng, G. D. C. Csete de Györgyfalva, R. Quimby, H. Bagshaw, R. Ubic, I. M. Reaney, and J. Yarwood. Raman Spectroscopy and Microwave Properties of $CaTiO_3$-Based Ceramics. *J. Appl. Phys.* **94**, 2948–2956 (2003).

[82] V. Železny, E. Cockayne, J. Petzelt, M. F. Limonov, D. E. Usvyat, V. V. Lemanov, and A. A. Volkov. Temperature Dependence of Infrared-Active Phonons in $CaTiO_3$: A Combined Spectroscopic and First-Principles Study. *Phys. Rev. B* **66**, 224 303 (2002).

[83] K. Fukuda, R. Kitoh, and I. Awai. Far-Infrared Reflection Spectra of Dielectric Ceramics for Microwave Applications. *J. Am. Ceram. Soc.* **77**, 149–154 (1994).

[84] S. Kamba, M. Berta, A. Pashkin, J. Petzelt, G. D. C. Csete de Györgyfalva, and I. M. Reaney. High Frequency Dielectric Properties of $CaTiO_3$-Based Microwave Ceramics To be published.

[85] J. Kobayashi, Y. Tazoh, M. Sasaura, and S. Miyazawa. Structural Analysis of Lanthanum Gallate. *J. Mater. Res.* **6**, 97–100 (1991).

[86] C. J. Howard and B. J. Kennedy. The Orthorombic and Rombohedral Phases of $LaGaO_3$ - a Neutron Powder Diffraction Study. *J. Phys.: Condens. Matter* **11**, 3229–3236 (1999).

[87] G. A. Tompsett, N. M. Sammes, and R. J. Phillips. Raman Spectroscopy of $LaGaO_3$ Phase Transition. *J. Raman Spectrosc.* **30**, 497–500 (1999).

[88] T. Inagaki, K. Miura, H. Yoshida, J. Fujita, and M. Nishimura. Raman Studies of $LaGaO_3$ and Doped $LaGaO_3$. *Solid State Ionics* **118**, 265–269 (1999).

[89] P. Calvani, M. Capizzi, F. Donato, P. Dore, S. Lupi, P. Maselli, and C. P. Varsamis. Infrared Optical Properties of Perovskite Substrates for High-T_c Superconducting Films. *Physica C* **181**, 289–295 (1991).

[90] Z. M. Zhang, B. I. Choi, M. I. Flik, and A. C. Anderson. Infrared Refrative Indices of $LaAlO_3$, $LaGaO_3$ and $NdGaO_3$. *J. Opt. Soc. Am. B* **11**, 2252–2257 (1994).

[91] D. C. Dube, H. J. Scheel, I. Reaney, M. Daglish, and N. Setter. Dielectric Properties of Lanthanum Gallate ($LaGaO_3$) Crystal. *J. Appl. Phys.* **75**, 4126–4130 (1994).

[92] S.-Y. Cho, I.-T. Kim, and K. S. Hong. Microwave Dielectric Properties and Applications of Rare-Earth Aluminates. *J. Mater. Res.* **14**, 114–119 (1999).

[93] B. Jančar, D. Suvorov, and M. Valant. Microwave Dielectric Properties of $CaTiO_3$-$NdAlO_3$ Ceramics. *J. Mater. Sci. Lett.* **20**, 71–72 (2001).

[94] B. Jančar, D. Suvorov, M. Valant, and G. Drazic. Characterization of $CaTiO_3$-$NdAlO_3$ Dielectric Ceramics. *J. Eur. Ceram. Soc.* **23**, 1391–1400 (2003).

[95] D. Suvorov, M. Valant, , B. Jančar, and D. Škapin. $CaTiO_3$-based Ceramics: Microstructural Development and Dielectric Properties. *Acta Chim. Slov.* **48**, 87–99 (2001).

[96] T. Nakazawa, T. Inoue, M. Satoh, and Y. Yamamoto. Electrical Characteristics of Metal/Cerium Dioxide/Silicon Structures. *Jpn. J. Appl. Phys.* **34**, 548–553 (1995).

[97] M. N. Rahaman and Y. C. Zhou. Effect of Solid Solution Additivies on the Sintering of Ultra-Fine CeO_2 Powders. *J. Eur. Ceram. Soc.* **15**, 939–950 (1995).

[98] D.-H. Kim, S.-K. Lim, and C. An. The Microwave Dielectric Properties of xTiO_2 (1-x)CeO_2 Ceramics. *Mater. Lett.* **52**, 240–243 (2002).

[99] F. Marabelli and P. Wachter. Covalent Insulator CeO_2: Optical Reflectivity Measurements. *Phys. Rev. B* **36**, 1238–1243 (1987).

[100] W. H. Weber, K. C. Hass, and J. R. McBride. Raman Study of CeO_2: Second-order Scattering, Lattice Dynamics, and Particle-Size Effects. *Phys. Rev. B* **48**, 178–185 (1993).

[101] N. I. Santha, M. T. Sebastian, P. Mohanan, N. Alford, K. Sarma, R. C. Pullar, S. Kamba, A. Pashkin, P. Samoukhina, and J. Petzelt. Effect of Doping on the Dielectric Properties of CeO_2 in the Microwave and Far-Infrared Frequency Range. *J. Am. Ceram. Soc.* (2003). To be published.

[102] J. Petzelt, T. Ostapchuk, I. Gregora, I. Rychetsky, S. Hoffmann-Eifert, A. V. Pronin, Y. Yuzyuk, B. P. Gorshunov, S. Kamba, V. Bovtun, J. Pokorny, M. Savinov, V. Porokhonskyy, D. Rafaja, P. Vanek, A. Almeida, M. R. Chaves, A. A. Volkov, M. Dressel, and R. Waser. Dielectric, Infrared, and Raman Response of Undoped $SrTiO_3$ Ceramics: Evidence of Polar Grain Boundaries. *Phys. Rev. B* **64**, 184 111 (2001).

[103] E. V. Bursian. *Nonlinear Crystal (Barium Titanate).* Nauka, Moscow (1974). In Russian.

[104] W. J. Merz. The Electric and Optical Behavior of $BaTiO_3$ Single-Domain Crystals. *Phys. Rev.* **76**, 1221–1225 (1949).

[105] R. Blinc and B. Zeks. *Soft Modes in Ferroelectrics and Antiferroelectrics.* North-Holland, Amsterdam (1974).

[106] R. H. Lyddane, R. G. Sachs, and E. Teller. On the Polar Vibrations of Alkali Halides. *Phys. Rev.* **59**, 673–676 (1941).

[107] W. Cochran. Crystal Stability and the Theory of Ferroelectricity. *Adv. Phys.* **9**, 387–423 (1960).

[108] K. A. Müller and H. Burkard. $SrTiO_3$: An Intrinsic Quantum Paraelectric Below 4 K. *Phys. Rev. B* **19**, 3593–3602 (1979).

[109] G. A. Samara and B. Morosin. Anharmonic Effects in $KTaO_3$: Ferroelectric Mode, Thermal Expansion, and Compressibility. *Phys. Rev. B* **8**, 1256–1264 (1973).

[110] V. V. Lemanov, A. V. Sotnikov, E. P. Smirnova, M. Weihnacht, and R. Kunze. Perovskite $CaTiO_3$ as an Incipient Ferroelectric. *Solid State Commun.* **110**, 611 (1999).

[111] J. H. Barrett. Dielectric Constant in Perovskite Type Crystals. *Phys. Rev.* **86**, 118–120 (1952).

[112] J. C. Slater. The Lorentz Correction in Barium Titanate. *Phys. Rev.* **78**, 748–761 (1950).

[113] O. E. Kvyatkovskii. Quantum Effects in Incipient and Low-Temperature Ferroelectrics (A Review). *Phys. Solid State* **43**, 1401–1419 (2001).

[114] L. E. Cross. Relaxor Ferroelectrics. *Ferroelectrics* **76**, 241–267 (1987).

[115] A. J. Bell. Calculation of Dielectric Properties from the Superparaelectric Model of Relaxors. *J. Phys.: Condens. Matter* **5**, 8773–8792 (1993).

[116] I. Rychetský, S. Kamba, V. Porokhonskyy, A. Pashkin, M. Savinov, V. Bovtun, J. Petzelt, M. Kosec, and M. Dressel. Frequency-Independent Dielectric Losses (1/F Noise) in PLZT Relaxors at Low Temperatures. *J. Phys.: Condens. Matter* **15**, 6017–6030 (2003).

[117] F. Chu, N. Setter, and A. K. Tagantsev. The Spontaneous Relaxor-Ferroelectric Transition of $Pb(Sc_{0.5}Ta_{0.5})O_3$. *J. Appl. Phys.* **74**, 5129–5134 (1993).

[118] I. M. Reaney, J. Petzelt, V. V. Voitsekhovskii, F. Chu, and N. Setter. B-Site Order and Infrared Reflectivity in $A(B'B'')O_3$ Complex Perovskite. *J. Appl. Phys.* **76**, 2086–2092 (1994).

[119] G. Burns and F. H. Dacol. Crystalline Ferroelectrics with Glassy Polarization Behavior. *Phys. Rev. B* **28**, 2527–2530 (1983).

[120] G. Burns and F. H. Dacol. Glassy Polarization Behavior in Ferroelectrics Compounds $Pb(Mg_{1/3}Nb_{2/3})O_3$ and $Pb(Zn_{1/3}Nb_{2/3})O_3$. *Solid State Commun.* **48**, 853–856 (1983).

[121] G. A. Samara. The Relaxational Properties of Compositionally Disordered ABO_3 Perovskites. *J. Phys.: Condens. Matter* **15**, R367–R411 (2003).

[122] D. Viehland, S. J. Jang, L. E. Cross, and M. Wuttig. Deviation from Curie-Weiss Behavior in Relaxor Ferroelectrics. *Phys. Rev. B* **46**, 8003–8006 (1992).

[123] P. Debye. *Polar Molecules*. Dover, New York (1929).

[124] D. Viehland, S. J. Jang, L. E. Cross, and M. Wuttig. Freezing of the Polarization Fluctuations in Lead Magnesium Niobate Relaxors. *J. Appl. Phys.* **68**, 2916–2921 (1990).

[125] A. K. Jonscher. *Universal Relaxation Law*. Chelsea Dielectrics Press, London (1996).

[126] A. K. Tagantsev. Vogel-Fulcher Relationship for the Dielectric Permittivity of Relaxor Ferroelectrics. *Phys. Rev. Lett.* **72**, 1100–1103 (1994).

[127] Z. Kutnjak, C. Filipic, A. Levstik, and R. Pirc. Glassy Dynamics of $Rb_{0.40}(ND_4)_{0.60}D_2PO_4$. *Phys. Rev. Lett.* **70**, 4015–4018 (1993).

[128] A. Levstik, Z. Kutnjak, C. Filipic, and R. Pirc. Glassy Freezing in Relaxor Ferroelectric Lead Magnesium Niobate. *Phys. Rev. B* **57**, 11 204–11 211 (1998).

[129] Z. Kutnjak, C. Filipic, R. Pirc, A. Levstik, R. Farhi, and M. E. Marssi. Slow Dynamics and Ergodicity Breaking in a Lanthanum-Modified Lead Zirconate Titanate Relaxor System. *Phys. Rev. B* **59**, 294–301 (1999).

[130] U. T. Höchli, K. Knorr, and A. Loidl. Orientational Glasses. *Adv. Phys.* **51**, 589–798 (2002).

[131] D. Viehland, M. Wutting, and L. E. Cross. The Glassy Behavior of Relaxor Ferroelectrics. *Ferroelectrics* **120**, 71–77 (1991).

[132] V. Westphal, W. Kleemann, and M. D. Glinchuk. Diffuse Phase Transition and Random-Field-Induced Domain States of the "relaxor" Ferroelectric $PbMg_{1/3}Nb_{2/3}O_3$. *Phys. Rev. Lett.* **68**, 847–850 (1992).

[133] R. Pirc and R. Blinc. Spherical Random-Bond – Random-Field Model of Relaxor Ferroelectrics. *Phys. Rev. B* **60**, 13 470–13 478 (1999).

[134] B. E. Vugmeister and M. D. Glinchuk. Dipole Glass and Ferroelectricity in Random-Site Electric Dipole Systems. *Rev. Mod. Phys.* **62**, 993–1026 (1990).

[135] C. Ang, Z. Yu, P. M. Vilarinho, and J. L. Baptista. Bi:$SrTiO_3$: A Quantum Ferroelectric and a Relaxor. *Phys. Rev. B* **57**, 7403–7406 (1998).

[136] J. J. van der Klink and S. N. Khanna. Off-Center Lithium Ions in $KTaO_3$. *Phys. Rev. B* **29**, 2415–2422 (1984).

[137] O. E. Kvyatkovskii. On the Nature of Ferroelectricity in $Sr_{1-x}A_xTiO_3$ and $KTa_{1-x}Nb_xO_3$ Solid Solutions. *Phys. Sol. State* **44**, 1135–1144 (2002).

[138] S. A. Prosandeev, E. Cockayne, and B. P. Burton. Energetics of Li Atom Displacements in $K_{1-x}Li_xTaO_3$: First-principles Calculations. *Phys. Rev. B* **68**, 014 120 (2003).

[139] J. J. van der Klink and F. Borsa. NMR Study of the Quasi-Reorientational Dynaimcs of Li Ions in $KTaO_3$:Li. *Phys. Rev. B* **30**, 52–64 (1984).

[140] A. V. Turik and A. G. Khasabov. Relaxation Kinetics in Virtual Ferroelectrics: (K,Li)TaO_3 Crystals. *J. Phys.: Condens. Matter* **13**, 1323–1327 (2001).

[141] Y. Girshberg and Y. Yacoby. Off-Centre Displacements and Ferroelectric Phase Transition in Dilute $KTa_{1-x}Nb_xO_3$. *J. Phys.: Condens. Matter* **13**, 8817–8830 (2001).

[142] O. Hanske-Petitpierre, Y. Yacoby, J. Mustre de Leon, E. A. Stern, and J. J. Rehr. Off-Center Displacement of the Nb Ions Below and Above the Ferroelectric Phase Transition of $KTa_{0.91}Nb_{0.09}O_3$. *Phys. Rev. B* **44**, 6700–6707 (1991).

[143] R. Morf, T. Schneider, and E. Stoll. Nonuniversal Critical Behavior and its Suppression by Quantum Fluctuations. *Phys. Rev. B* **16**, 462–469 (1977).

[144] U. T. Höchli, H. E. Weibel, and L. A. Boatner. Quantum Limit of Ferroelectric Phase Transitions in $KTa_{1-x}Nb_xO_3$. *Phys. Rev. Lett.* **39**, 1158–1161 (1977).

[145] J. G. Bednorz and K. A. Müller. $Sr_{1-x}Ca_xTiO_3$: An XY Quantum Ferroelectric with Transition to Randomness. *Phys. Rev. Lett.* **52**, 2289–2292 (1984).

[146] J. Toulouse, B. E. Vugmeister, and R. Pattnaik. Collective Dynamics of Off-Center Ions in $K_{1-x}Li_xTaO_3$: A Model of Relaxor Behavior. *Phys. Rev. Lett.* **73**, 3467–3470 (1994).

[147] S. A. Prosandeev and V. A. Trepakov. The Dielectric Response of Quantum Paraelectrics Containing Dipole Impurities. *JETP* **94**, 419–430 (2002).

[148] H. Vogt. Stiffening and Splitting of the Soft Mode of $KTaO_3$ Induced by Doping with Li. *Ferroelectrics* **202**, 157–165 (1997).

[149] G. Kugel, H. Vogt, W. Kress, and D. Rytz. Study of the Ferroelectric Soft Mode in Solid Solutions of $KTa_{1-x}Nb_xO_3$ by hyper-Raman Scattering. *Phys. Rev. B* **30**, 985–991 (1984).

[150] H. Chou, S. M. Shapiro, K. B. Lyons, J. Kjems, and D. Rytz. Soft-Mode Behavior and the Dipolar Glass Transition in $KTa_{1-x}Nb_xO_3$. *Phys. Rev. B* **41**, 7231–7234 (1990).

[151] Y. Yacoby and Y. Girshberg. Ferroelectricity in Doped Incipient Ferroelectrics. *AIP Conference Proceedings* **626**, 132–140 (2002).

[152] K. B. Lyons, P. A. Fleury, and D. Rytz. Cluster Dynamics in a Dipolar Glass. *Phys. Rev. Lett.* **57**, 2207–2210 (1986).

[153] M. D. Fontana, E. Bouziane, and G. E. Kugel. Order and Disorder Processes in the Raman Spectrum of $KTa_{1-x}Nb_xO_3$. *J. Phys.: Condens. Matter* **2**, 8681–8689 (1990).

[154] H. Vogt. Hyper-Raman Study of Li-induced Polarization Clusters in $K_{1-x}Li_xTaO_3$. *J. Phys.: Condens. Matter* **7**, 5913–5929 (1995).

[155] P. A. Fleury and J. M. Worlock. Electric-Field-Induced Raman Scattering in $SrTiO_3$ and $KTaO_3$. *Phys. Rev.* **174**, 613 (1968).

[156] R. L. Prater, L. L. Chase, and L. A. Boatner. Raman Scattering Studies of the Impurity-Induced Ferroelectric Phase Transition in $KTaO_3$: Nb. *Phys. Rev. B* **23**, 221–231 (1981).

[157] R. L. Prater, L. L. Chase, and L. A. Boatner. Raman Scattering Studies of the Impurity-Induced Ferroelectric Phase Transition in $KTaO_3$:Li. *Phys. Rev. B* **23**, 5904–5915 (1981).

[158] J. Toulouse, P. DiAntonio, B. E. Vugmeister, X. M. Wang, and L. A. Knauss. Precursor Effects and Ferroelectric Marcoregions in $KTa_{1-x}Nb_xO_3$ and $K_{1-x}Li_xTaO_3$. *Phys. Rev. Lett.* **68**, 232–235 (1992).

[159] P. Calvi, P. Camagni, E. Giulotto, and L. Rollandi. Raman Scattering and the Evolution of Polar Order in Li-doped and Nb-doped $KTaO_3$. *Phys. Rev. B* **53**, 5240–5246 (1996).

[160] H. Vogt. Evidence of Defect-Induced Polarization Clusters in Nominally Pure $KTaO_3$ from Low-Temperature Raman and hyper-Raman Spectra. *J. Phys.: Condens. Matter* **3**, 3697 (1991).

[161] H. Vogt. Permanent Dipole Moment and First-Order Hyperpolarizability If Li-induced Polarization Clusters in $K_{1-x}Li_xTaO_3$ Determined by hyper-Raman Spectroscopy. *Phys. Rev. B* **58**, 9916–9925 (1998).

[162] V. Bovtun, J. Petzelt, V. Porokhonskyy, S. Kamba, and Y. Yakimenko. Structure of the Dielectric Spectrum of Relaxor Ferroelectrics. *J. Eur. Ceram. Soc.* **21**, 1307–1311 (2001).

[163] H.-M. Christen, U. T. Höchli, A. Chatelain, and S. Ziolkiewicz. Random-Barrier and Hierarchical Relaxation in $K_{1-x}Li_xTaO_3$. *J. Phys.: Condens. Matter* **3**, 8387–8401 (1991).

[164] W. Kleemann, A. Albertini, M. Kuss, and R. Lindner. Optical Detection of Symmetry Breaking on a Nanoscale in $SrTiO_3$:Ca. *Ferroelectrics* **203**, 57–74 (1997).

[165] G. Yong, J. Toulouse, R. Erwin, S. M. Shapiro, and B. Hennion. Pretranslational Diffuse Neutron Scattering in the Mixed Perovskite Relaxor $K_{1-x}Li_xTaO_3$. *Phys. Rev. B* **62**, 14 736–14 743 (2000).

[166] P. M. Gehring, S.-E. Park, and G. Shirane. Soft Phonon Anomalies in the Relaxor Ferroelectric $Pb(Zn_{1/3}Nb_{2/3})_{0.92}Ti_{0.08}O_3$. *Phys. Rev. Lett.* **84**, 5216–5219 (2000).

[167] J. Hlinka, S. Kamba, J. Petzelt, J. Kulda, C. A. Randall, and S. J. Zhang. Origin of "waterfall" Effect in Phonon Dipersion of Relaxor Perovskites. *Phys. Rev. Lett.* **91**, 107 602 (2003).

[168] S. R. Andrews. X-Ray Scattering Study of the Random Electric Dipole System $KTaO_3$:Li. *J. Phys. C* **18**, 1357–1376 (1985).

[169] P. Bonneau, P. Garnier, G. Calvarin, E. Husson, J. R. Gavarri, and A. T. Hewat. X-Ray and Neutron Diffraction Studies of the Diffuse Phase Transition in $PbMg_{1/3}Nb_{2/3}O_3$ Ceramics. *J. Solid State Chem.* **91**, 350–361 (1991).

[170] J. J. van der Klink, D. Rytz, F. Borsa, and U. T. Höchli. Collective Effects in a Random-Site Electric Dipole System: $KTaO_3$:Li. *Phys. Rev. B* **27**, 89–101 (1983).

[171] M. D. Glinchuk, V. Skorokhod, I. P. Bykov, V. Dimza, and E. Cernoskova. The Study of Polycrystalline $PbMg_{1/3}Nb_{2/3}O_3$ by the Electron-Paramagnetic-Resonance of Fe^{3+} Ions. *J. Phys.: Condens. Matter* **6**, 3421–3428 (1994).

[172] J. Petzelt, S. Kamba, and I. Gregora. Infrared and Raman Spectroscopy of Ill-Ordered Crystals. *Phase Transitions* **63**, 107–145 (1997).

[173] S. Kamba, V. Bovtun, J. Petzelt, I. Rychetsky, R. Mizaras, A. Brilingas, J. Banys, J. Grigas, and M. Kosec. Dielectric Dispersion of the Relaxor PLZT Ceramics in the Frequency Range 20 Hz-100 THz. *J. Phys.: Condens. Matter* **12**, 497–519 (2000).

[174] J. Petzelt, E. Buixaderas, and A. V. Pronin. Infrared Dielectric Reponse of Ordered and Disordered Ferroelectric $Pb(Sc_{1/2}Ta_{1/2})O_3$ Ceramics. *Materials Science and Engineering B* **55**, 86–94 (1998).

[175] A. Pashkin, P. Samoukhina, T. Ostapchuk, P. Kužel, P. Vilarinho, and J. Petzelt. Submillimeter and Far Infrared Dielectric Response of Bi-doped $SrTiO_3$ Ceramics. *Ferroelectrics* **294**, 133–139 (2003).

[176] M. Savinov. *Low Frequency Dielectric Spectroscopy of Nominally Pure and Diluted* $KTaO_3$*,* $KTaO_3 : Li$*, and* $KTaO_3 : Li + Nb$. Ph.D. thesis, Czech Technical University, Prague (2001).

[177] J. J. van der Klink and D. Rytz. Growth of $K_{1-x}Li_xTaO_3$ Crystals by a Slow-Cooling Method. *J. Crystal Growth* **56**, 673–676 (1982).

[178] P. Voigt and S. Kapphan. Experimental Study of Second Harmonic Generation by Dipolar Configurations in Pure and Li-doped $KTaO_3$ and its Variation under Electric Field. *J. Phys. Chem. Solids* **55**, 853–869 (1994).

[179] Y. Fujii and T. Sakudo. Electric-Field-Induced Optical Second-Harmonic Generation in $KTaO_3$ and $SrTiO_3$. *Phys. Rev. B* **13**, 1161–1167 (1976).

[180] S. K. Kurtz and T. T. Perry. A Powder Technique for the Evaluation of Nonlinear Optical Materials. *J. Appl. Phys.* **39**, 3798–3813 (1968).

[181] W. Kleemann, S. Kütz, and D. Rytz. Cluster Glass and Domain State Properties of Lithium-Doped Potassium Tantalate. *Europhys. Lett.* **4**, 239–245 (1987).

[182] W. Kleemann, S. Kütz, and D. Rytz. Cluster Glass and Domain State Properties of $KTaO_3$:Li. *Europhys. Lett.* **4**, 239–245 (1987).

[183] K. Szot, W. Speier, M. Pawelczyk, J. Kwapuliñski, J. Hulliger, H. Hesse, U. Breuer, and W. Quadakkers. Chemical Inhomogeneity in the Near-Surface Region of $KTaO_3$ Evolving at Elevated Temperatures. *Journal of Physics: Condensed Matter* **12** (22), 4687–4697 (2000).

[184] C. H. Perry and T. F. McNelly. Ferroelectric "Soft" Mode in $KTaO_3$. *Phys. Rev.* **154**, 456–458 (1966).

[185] U. T. Höchli, H. E. Weibel, and L. A. Boatner. Extrinsic Peak in the Susceptibility of Incipient Ferroelectric $KTaO_3$:Li. *Phys. Rev. Lett.* **41**, 1410–1413 (1978).

[186] S. Jandl, M. Banville, P. Dufour, S. Coulombe, and L. A. Boatner. Infrared Study of Oxygen Vacancies in $KTaO_3$. *Phys. Rev. B* **43**, 7555–7560 (1991).

[187] F. Borsa, U. T. Höchli, J. J. van der Klink, and D. Rytz. Condensation of Random-Site Electric Dipoles: Li in $KTaO_3$. *Phys. Rev. Lett.* **45**, 1884–1887 (1980).

[188] H. Schremmer, W. Kleemann, and D. Rytz. Field-Induced Sharp Ferroelectric Phase Transition in $K_{0.937}Li_{0.063}TaO_3$. *Phys. Rev. Lett.* **62**, 1896–1899 (1989).

[189] G. A. Azzini, G. P. Banfi, E. Guilotto, and U. T. Höchli. Second-Harmonic Generation and Origin of Polar Configuration in $KTaO_3$:Li. *Phys. Rev. B* **43**, 7473–7480 (1991).

[190] G. P. Banfi, P. Calvi, and E. Giulotto. Spontaneous and Field-Assisted Transition in $K_{0.984}Li_{0.016}TaO_3$: The Polar Pattern by Birefringence and Second-Harmonic Generation. *Phys. Rev. B* **51**, 6231–6236 (1995).

[191] R. S. Klein, G. E. Kugel, and B. Hennion. Inelastic Neutron Scattering Measurements on the Transverse Acoustic and Lowest Optic Modes in $KTaO_3$ Doped with Lithium. *J. Phys.: Condens. Matter* **8**, 1109–1121 (1996).

[192] H. Vogt. Soft-Mode Splitting in the Low-Temperature Phase of $K_{1-x}Li_xTaO_3$: A Comparative Raman and hyper-Raman Study. *J. Phys.: Condens. Matter* **13**, 4313–4322 (2001).

[193] O. Hudak, I. Rychetský, and J. Petzelt. Dielectric Response of Microcomposite Ferroelectrics. *Ferroelectrics* **208**, 429–447 (1998).

[194] C. J. F. Böttcher. *Theory of Electric Polarization*. Elsevier, second edn. (1973).

[195] I. Levin, J. Y. Chan, J. E. Maslar, T. A. Vanderah, and S. M. Bell. Phase Transitions and Microwave Dielectric Properties in the Perovskite-Like $Ca(Al_{0.5}Nb_{0.5})O_3 - CaTiO_3$ System. *J. Appl. Phys.* **90**, 904–914 (2001).

[196] R. D. Shannon. Dielectric Polarizabilities of Ions in Oxides and Fluorides. *J. Appl. Phys.* **73**, 348–366 (1993).

[197] G. L. Carr, S. Perkowitz, and D. B. Tanner. *Infrared and Millimeter Waves*. Academic Press (1985).

[198] U. T. Höchli, H. E. Weibel, and W. Rehwald. Elastic and Dielectric Dispersion in the Dipole Glass $K_{1-x}Li_xTaO_3$. *Journal of Physics C: Solid State Physics* **15** (30), 6129–6140 (1982).

[199] B. A. Strukov and A. P. Levanyuk. *Ferroelectric Phenomena in Crystals. Physical Foundations*. Springer Verlag (1998).

[200] V. A. Trepakov, S. A. Prosandeev, M. E. Savinov, P. Galinetto, G. Samoggia, S. E. Kapphan, L. Jastrabik, and L. A. Boatner. Long-Range Displacive to Short-Range Order-Disorder Crossover in Weakly Concentrated $KTa_yNb_{1-y}O_3$. *Jpn. J. Appl. Phys.* **41**, 7176–7178 (2002).

[201] V. A. Trepakov, M. E. Savinov, E. Giulotto, P. Galinetto, P. Camagni, G. Samoggia, L. A. Boatner, and S. E. Kapphan. Dipole Ordering Effects and Reentrant Dipolar Glass State in $KTaO_3$:Li,Nb. *Phys. Rev. B* **63**, 172 203 (2001).

[202] W. Kleemann, F. J. Schäfer, and D. Rytz. Diffuse Ferroelectric Transition and Long-Range Order of Dilute $KTa_{1-x}Nb_xO_3$. *Phys. Rev. Lett.* **54**, 2038–2041 (1985).

[203] G. I. Skanavi and E. N. Matveeva. New Dielectrics with High Permittivity and Low Conductivity Possessing Nonferroelectric Properties. *Sov. Phys. JETP* **3**, 905 (1957).

[204] G. I. Skanavi, Y. M. Ksendzov, V. A. Trigubenko, and V. V. Prokhvatilov. Relaxation Polarization and Losses in Nonferroelectric Dielectrics Possessing Very High Dielectric Constants. *Sov. Phys. JETP* **6**, 250 (1958).

[205] Zhi Yu, Chen Ang, and L. E. Cross. Oxygen-Vacancy-Related Dielectric Anomalies in La:$SrTiO_3$. *Appl. Phys. Lett.* **74**, 3044–3046 (1999).

[206] K. V. Kiselova and S. V. Bogdanov. Structure Investigation of Solid Solutions $SrTiO_3 - Bi_2O_3 \cdot 3TiO_2$. *Sov. Solid State Phys.* **5**, 2294 (1964).

[207] Z. Yu. *Dielectric Polarisation and Relaxation Behavior in Bi and La Doped* $SrTiO_3$ *Ceramics*. Ph.D. thesis, University of Aveiro, Portugal (1997).

[208] C. Ang, Z. Yu, and Z. Jing. Impurity-Induced Ferroelectric Relaxor Behavior in Quantum Paraelectric $SrTiO_3$ and Ferroelectric $BaTiO_3$. *Phys. Rev. B* **61**, 957–961 (2000).

[209] A. Almeida, P. Teles, M. R. Chaves, P. M. Vilarinho, and J. L. Baptista. Raman Spectroscopy and Pyroelectric Studies of $SrTiO_3$ Ceramics Doped with Different Concentrations of Bismuth. *Ferroelectrics* **294**, 49–59 (2003).

[210] V. Porokhonskyy, A. Pashkin, V. Bovtun, J. Petzelt, M. Savinov, P. Samoukhina, T. Ostapchuk, J. Pokorný, M. Avdeev, A. Kholkin, and P. Vilarinho. Broad-Band Dielectric Spectroscopy of $SrTiO_3$:Bi Ceramics Accepted to Phys. Rev. B.

[211] C. Ang, Z. Yu, P. Lunkenheimer, J. Hemberger, and A. Loidl. Dielectric Relaxation Modes in Bismuth-Doped $SrTiO_3$: The Relaxor Behavior. *Phys. Rev. B* **59**, 6670–6673 (1999).

[212] V. Bovtun, V. Porokhonskyy, M. Savinov, T. Ostapchuk, P. Samoukhina, J. Petzelt, P. Vilarinho, and J. Baptista. Wide-Frequency Range Dielectric Relaxations in $Sr_{1-1.5x}Bi_xTiO_3$ Ceramics. *Ferroelectrics* **272**, 357–362 (2002).

[213] L. Onsager. Electric Moments of Molecules in Liquids. *J. Am. Chem. Soc.* **58**, 1486–1493 (1936).